Design and optimization of inductive power transfer systems by metamodeling techniques

Yao Pei

THÈSE DE DOCTORAT

NNT : 2022UPAST145

université PARIS-SACLAY

Design and optimization of inductive power transfer systems by metamodeling techniques

Conception et optimisation de systèmes de transfert de puissance inductifs par des techniques de métamodélisation

Thèse de doctorat de l'université Paris-Saclay

École doctorale n° 575: Electrical, Optical, Bio: Physics And Engineering (EOBE)
Spécialité de doctorat : Génie électrique
Graduate School : Sciences de l'ingénierie et des systèmes. Référent : Faculté des sciences d'Orsay

Thèse préparée au **Laboratoire de Génie Electrique et Electronique de Paris (Université Paris-Saclay, CentraleSupélec, CNRS),** sous la direction de **Lionel PICHON**, Directeur de Recherche, le co-encadrement de **Mohamed BENSETTI**, Professeur, et le co-encadrement de **Yann LE BIHAN**, Professeur

Thèse soutenue à Paris-Saclay, le 7 Décembre 2022, par

Yao PEI

Composition du Jury

Membres du jury avec voix délibérative

Sami HLIOUI Professeur à CY Cergy Paris Université, SATIE	Président du jury
Francesca MARADEI Professeur à la Sapienza University of Rome	Rapporteure & Examinatrice
Christophe GUIFFAUT Chargé de recherche au CNRS - HDR, XLIM	Rapporteur & Examinateur
Didier TRICHET Professeur à l'Université de Nantes, IREENA	Examinateur
Cyril DAHON Maître de Conférences à Sorbonne Université, GeePs	Examinateur

université PARIS-SACLAY
DOCTORAL SCHOOL
Electrical, Optical, Bio: Physics and Engineering (EOBE)

Titre: Conception et optimisation de systèmes de transfert de puissance inductifs par des techniques de métamodélisation

Mots clés : Transfert de puissance inductif; dévellopement en chaos polynomial; analyse de sensibilité; optimisation

Résumé: L'objectif de cette thèse est de proposer une méthode de métamodélisation afin d'évaluer l'efficacité d'un système de transfert de puissance inductif résonant (TPIR) et de gérer les contraintes de compatibilité électromagnétique (CEM) dans les véhicules électiques (VE). La méthode inclut simultanément différents aspects du problème électromagnétique: la forme des bobines, les caractéristiques géométriques du système (ferrites, châssis du véhicule, plaques de blindage), le désalignement entre l'émetteur et le récepteur. Cette méthodologie repose sur la combinaison de la méthode des éléments finis (MEF) avec des techniques de métamodélisation.

Tout d'abord, l'efficacité de transmission maximale et la densité de flux magnétique de fruite ont été analysées pour quatre formes de coupleurs (circulaire, carré, bipolaire (BP) et double-D (DD)). Nous avons modélisé ces structures de coupleurs par des calculs MEF COMSOL 3D puis vérifié par des mesures expérimentales sur des prototypes à l'échelle 1:10 développés au laboratoire GeePs. Il apparaît que le rapport entre la longueur du fil conducteur et l'inductance mutuelle influence directement l'efficacité maximale de la transmission quand l'émetteur et le récepteur sont identiques. Concernant l'efficacité de transmission maximale, les coupleurs circulaires peuvent fournir les valeurs maximales parmi ces coupleurs, mais les coupleurs carrés ont une plus grande tolérance au désalignement entre bobines que les autres; en revanche, les coupleurs carrés ont plus de fuites de champ magnétique. Cependant, les coupleurs carrés sont choisis car ils sont plus faciles à fabriquer et conviennent mieux au TPIR dynamique.

Deuxièmement, afin de prendre en compte les sources d'incertitude (le désalignement, ou la rotation du récepteur), différents métamodèles (régression par machine à vecteur de support (SVR), algorithme de programmation génétique multigénique (MGPA), dévellopement en chaos polynomial (PCE)) ont été comparés dans le cas d'un coupleur carré à échelle réduite. En raison du compromis entre le temps de calcul et la précision, la technique PCE a été retenu. Selon l'analyse de sensibilité établie à partir des coefficients des métamodèles, le désalignement le long de la longueur de la bobine s'est avèré le facteur le plus influent pour les coupleurs DD/BP, alors que les désalignements le long de la longueur et de la largeur de la bobine ont le même effet sur les coupleurs circulaires et carrés, en raison des symétries.

Ensuite, une optimisation multi-objectifs combinée avec un métamodèle PCE a été proposée pour un système TPIR sans blindage (développé au laboratoire GeePs et à l'institut Vedecom) et un autre système avec blindage (développé au laboratoire GeePs). Le but était de déterminer les dimensions du système, afin d'une part d'améliorer l'efficacité de la transmission et d'autre part de réduire le poids/le coût du système en prenant en compte les recommandations de l'ICNIRP. Par rapport à une approche traditionnelle d'optimisation, cette méthode peut économiser plusieurs fois le temps de calcul (y compris le temps d'apprentissage) et les ressources de calcul. Deux algorithmes d'optimisation: Non-dominated Sorting Genetic Algorithm II (NSGA-II) et Multiobjective Particle Swarm Algorithm (MOPSO) sont comparés. Il en ressort qu'un métamodèle PCE avec MOPSO s'avère une approche performante pour effectuer l'optimisation lorsqu'on considère un système impliquant un grand nombre de variables de conception sous contraintes. Par ailleurs, une optimisation topologique permet d'affiner le placement de la ferrite dans la zone obtenue afin de réduire le volume de ferrite sans trop affecter l'inductance mutuelle.

université PARIS-SACLAY

DOCTORAL SCHOOL
Electrical, Optical, Bio: Physics and Engineering (EOBE)

Title: Design and optimization of inductive power transfer systems by metamodeling techniques

Keywords: Inductive power transfer; Polynomial chaos expansion; Sensitivity analysis; Optimization

Abstract: The aim of this thesis is to propose a metamodeling method in order to assess the efficiency of the resonant inductive power transfer system and to manage electromagnetic compatibility (EMC) constraints in the electric vehicles (EVs). The method simultaneously includes various aspects of the electromagnetic problem: the shape of the coils, geometrical characteristics of the system (ferrites, chassis of vehicle, shielding plates), and possible misalignment between transmitter and receiver while charging. This methodology relies on the combination of the finite element method (FEM) with metamodeling techniques.

First, the maximum transmission efficiency and magnetic flux density leakage are analyzed for four shapes of couplers (circular, square, bipolar (BP), and double-D (DD)). They are compared using COMSOL 3D FEM simulations and the experiments on 1:10 scale prototypes developed in the GeePs laboratory. It was shown that the ratio between the wire length and the mutual inductance mainly influences the maximum transmission efficiency when the transmitter and the receiver are identical. The analysis was performed on the electrical circuit in the series-series compensation topology. Regarding the maximum transmission efficiency in RIPT systems, the circular coupler can provide the maximum values among different shapes of coils, but the square coupler has a higher tolerance to misalignment than others; meanwhile, the square coupler also has a higher magnetic flux density leakage. However, the square coupler is chosen instead of the circular one as it is easier to manufacture and is more suitable in the dynamic RIPT.

Secondly, to take into account the sources of uncertainty (the misalignment or the rotation of the receiver), various metamodels (support vector machine regression (SVR), multigene genetic programming algorithm (MGPA), sparse polynomial chaos expansions (sparse PCE)) were built and compared for analyzing the mutual inductance on the small scale square coupler. Due to the tradeoff between the computational time and the accuracy of the metamodel, the sparse PCE metamodel was chosen. According to the sensitivity analysis established on the coefficients of PCE metamodels, the misalignment along the length of the coil appeared to be the most influential factor in the mutual inductance for DD/BP couplers, whereas the misalignment along the length/width of the coil had the same effect as the circular and the square couplers, due to their symmetries.

Then, a method was proposed to perform a multiobjective optimization with the sparse PCE metamodeling technique to the RIPT system without shielding (developed by GeePs laboratory and Vedecom institute) and the one with shielding (developed by GeePs laboratory). The aim was to find the best dimensions of the system for improving the transmission efficiency and decreasing the volume of the system/ the cost of the system under the ICNIRP guidelines. Compared to 3D FEM computations with multiobjective optimization methods, this method may save several times the computational time (including the time to calculate the training samples) and computational resources. Two optimization algorithms: Non-dominated Sorting Genetic Algorithm II (NSGA-II) et Multiobjective Particle Swarm Algorithm (MOPSO) were compared, and it comes out that associating PCE metamodel with MOPSO uses a shorter computational time, and it can find a larger set of feasible solutions than the PCE metamodel with NSGA-II. Furthermore, topology optimization with the solid isotropic material with penalization (SIMP) method is used to find a ferrite distribution that maximizes the mutual inductance while constraining the volume of ferrite.

Acknowledgement

Upon the completion of my Ph.D. thesis, I am really thankful to those who have offered me invaluable help during the three-year study and life.

First of all, special acknowledgement is given to my respectable supervisors, Prof. Lionel PICHON, Prof. Mohamed BENSETTI and Prof. Yann LE BIHAN, for their patient instructions and insightful suggestions on my thesis.

Secondly, particular thanks go to the members of my jury, Prof. Christophe GUIFFAUT, Prof. Francesca MARADEI, Prof. Sami HLIOUI, Prof. Didier TRICHET, M. Cyril DAHON for my Ph.D. defense and their constructive comments on my work. I appreciated our fruitful discussion very much.

Besides, I should express my sincere gratitude to my colleagues in GeePs and the friends around, especially prof. Demba DIALLO, Dr. Haiteng SUN, Dr. Baojie LI, M. Qihao GUO, Mme. Jie SUN, Mme. Chuanyong SHAO, Dr. Sleimane NASSER EL DINE, Dr. Guili ZHAO, Mme. Mengyu GAO. This journey was interesting because you helped me and shared my worries, frustrations, and happiness with me.

Last but not least, I would like to extend my deep gratefulness to my family, especially my parents and my little brother. Their encouragement and support have made my accomplishments possible.

CONTENTS

List of Figures

List of Tables

INTRODUCTION

The use of a resonant inductive power transfer (RIPT) system seems an effective technology for the growth of electric vehicles (EVs). Moreover, its application for the charge during the motion of the vehicle (dynamic RIPT) is promising to overcome the barriers represented by the heavy onboard battery storage and the long recharging time. RIPT is essentially based on the resonance of two magnetically coupled inductors (constituting the coupler): the transmitter, placed on the ground, and the receiver, placed under the vehicle floor. The operating frequency typically ranges from 20 kHz to 100 kHz. The coupling between the two inductors takes place through an air gap, usually about 10~25 cm.

Although RIPT systems are now widely studied, there are still several challenges in designing the coil system. Up to now, there is no comprehensive methodology allowing a fast, reliable, and efficient design and optimization of a coil system for RIPT systems. Adequate methodologies have to take into account the environment of the system, including the impact of the car chassis and the presence of the human body since it is needed to evaluate the level of exposure in order to be compliant with international standards. Recently, 3D finite element methods (FEMs) have been studied and applied to solve the electromagnetic problem involving the RIPT system. Such a computational approach gives reliable results about the electrical parameters (mutual inductance, transmission efficiency) and the magnetic parameters (magnetic flux density leakage) around the system, but it may lead to heavy computations that have to be repeated for each new configuration that is highly dependent on various parameters: the size of coils, geometrical characteristics of the system (e.g., ferrite plates, shielding plates), possible misalignment between transmitter and receiver while charging.

So, the goal of the thesis is to propose a fast and efficient modeling methodology in order to assess the efficiency of RIPT systems and manage EMC constraints in EVs. The introduction of metamodeling techniques allows to manage the variability of design variables describing the electromagnetic problem and to quantitatively determine the contribution of each design variable to the observed output. Next, it combines multiobjective optimization algorithms to find the best dimensions of a practical RIPT system. This proposed methodology can get faster conclusions at a low cost compared to 3D FEM with multiobjective optimization algorithms. Then, some tips for the placements of ferrite are deduced in the studied area by topology optimization with solid isotropic material with penalization (SIMP) method.

The structure of the thesis is as follows:

Chapter 1 describes the state of art and introduces the general idea of a wireless power transfer (WPT) system, and discusses the application of the WPT system in modern society. The current method in the main share of the WPT market for charging EVs is based on the principle of the RIPT system. The operation modes, main standards, magnetic couplers, and compensation topologies for the RIPT systems are briefly concluded. Next, the existing optimization methods for analyzing the performances of RIPT systems are also presented and compared, which leads to heavy computations that have to be repeated for each new configuration which can be costly when using numerical modeling (such as FEM). Then, the metamodeling techniques have been

developed to characterize the system in the previous literature, but they have not been combined with the optimization method for accelerating the design process. So, the objective and aim of the thesis are presented in this chapter.

Chapter 2 is dedicated to studying the maximum transmission efficiency and magnetic flux density leakage for four shapes of couplers (circular, square, bipolar (BP), and double-D (DD)) in COMSOL 3D FEM simulations and experiments. How the ratio between the wire length and the mutual inductance between the transmitter and the receiver influences the maximum transmission efficiency η_{max} is analyzed when the transmitter and the receiver are identical. This relationship is deduced from the electrical circuit in the series-series compensation topology. In fact, a realization of real-scale coils used in EVs is costly, especially considering the price of the materials used (wire and ferrite). To save the construction cost, the studied coils are not built with a real size but miniaturized on a scale of 1:10. Then, in case of small-scale magnetic couplers, a comparison between COMSOL 3D results and experimental ones, including the electrical parameters (mutual inductance,η_{max}) and the magnetic flux density distribution around the system. Moreover, the quantitative relationship between the real scale and small scale of the square couplers is also presented.

Chapter 3 compares different metamodeling techniques: the support vector machine regression (SVR), multigene genetic programming algorithm (MGPA), and sparse polynomial chaos expansions (PCE) for analyzing the mutual inductance of small-scale square couplers, taking into account the sources of uncertainty. The sparse PCE metamodeling technique is selected due to its higher accuracy and its character in doing the sensitivity analysis. Next, how the sources of uncertainty influence the mutual inductances and the maximum transmission efficiency of small-scale couplers (circular, square, DD, and BP) are discussed by sparse PCE metamodels.

Chapter 4 focuses on the methodology to optimize the RIPT system. First, multiobjective optimization methods (Non-dominated Sorting Genetic Algorithm II (NSGA-II) and Multiobjective Particle Swarm (MOPSO) algorithm) with the sparse PCE metamodeling technique is applied to find the best dimensions of a practical RIPT system under perfect alignment conditions. This method takes into account the transmission efficiency and the volume (ferrite)/ the cost (ferrite + aluminum plates) of the system. Then, topology optimization (TO) on the SIMP method is performed to appropriately find a ferrite distribution that maximizes the mutual inductance while constraining the volume of the ferrite.

CHAPTER 1 STATE OF ART

1.1 Introduction

Today, around 800 million vehicles with internal combustion engines (ICEs) are in use worldwide [1]. These vehicles are a major source of greenhouse gases, especially CO_2. Thus, an effective way of dealing with the global warming problem is to replace ICE-powered vehicles with all electric vehicles (EVs) [1-3]. The use of electric cars also improves the quality of air around major cities. To replace ICEs, many vehicle companies are developing "plug-in" EVs, which use lithium-ion (or polymer) batteries that can be recharged at home or at charging stations [2-3].

However, the promotion and adoption of plug-in EVs raise many questions. First, the cost of lithium batteries is high. Second, the batteries are heavy. Third, the charging time for the battery is so long that it requires an expensive infrastructure for charging stations [2-4]. Finally, the material to build lithium-ion batteries is limited on earth. Earth has only about ten million tons of lithium that can be mined economically, which is enough for about 800 million cars, almost the same as the number of cars in use today [3]. Battery replacement for EVs can drastically reduce the time to charge the battery but costs a lot due to a backup battery and battery replacement facilities [2-3].

So, due to these problems, wireless power transfer (WPT) has been introduced as an alternative technology. This technology has the capability to replace the plug-in interface with transmitters and receivers, allowing power flow in a contactless manner. Moreover, its application for the charge during the motion of the vehicle (dynamic WPT) is promising to overcome the barriers represented by the heavy onboard battery storage and the long recharging time [3-5].

In this chapter, we will present a state of the art concerning wireless charging for EVs and briefly describe and position the aim of the thesis work.

1.2 General introduction of WPT systems for EVs

1.2.1 Historical development of WPT systems

Wireless charging technology has been under development for the past few decades.

In 1826, André-Marie Ampère discovered a connection between current and magnets [6-7]. After five years, Michael Faraday described the law of induction: the electromotive force drives a current in a conductor loop when subjected to a time-varying magnetic flux [6-7]. The lack of a coherent theory attributed these phenomena that transmit electrical energy without wires vaguely to electromagnetic induction, but a concise explanation of these would come from the 1860s. In 1864, James Clerk Maxwell established a theory of Maxwell's equations that unified electricity and magnetism to electromagnetism [7-8]. Around 1884, John Henry Poynting defined the Poynting vector and gave Poynting's theorem, which describes the flow of power across an area within electromagnetic radiation and allows for a correct analysis of wireless power transfer systems [7-

9]. This was followed by Heinrich Rudolf Hertz, who demonstrated high-frequency power transfer using a spark gap and parabolic reflectors at both the transmitting and receiving ends of the system in 1888 [7, 9]. Then, Nikola Tesla carried out the wireless power transfer experiment that transmitted power with microwaves between two objects 48 km apart in 1897. However, due to a lack of funding, he did not further the experiments at his Wardenclyffe Laboratory [6-7, 10]. Figure 1.1 presents Tesla's experiment on WPT.

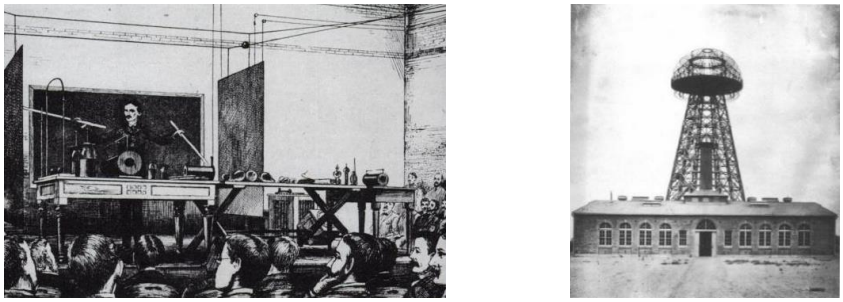

(a) Tesla demonstrating wireless transmission (b) Tesla's Wardenclyffe power station

Figure 1.1 Tesla's experiment on WPT [6-7, 10]

According to W.C. Brown et al., WPT's further development started during the period of World War II. At that time, the ability was acquired to generate substantial amounts of power at microwave frequencies where the energy could be focused into a narrow beam with the aid of parabolic reflectors [11]. So, until 1964, the first microwave wireless charging system was put into practical use by W. C. Brown, realizing the energy replenishment for a helicopter [6-7, 11]. On the basis of prior knowledge, researchers achieved further success in WPT system designs. In 1976, Dynamic Wireless Charging (DWC) was first introduced, and Lawrence Berkley National Laboratory (LBNL) evaluated its system feasibility [6-7, 12]. Later in 1993, the University of Auckland (UOA) developed a patent on non-contact power distribution [12-13]. Then, General Motors (GM) produced Magne Charge (an inductive charging system) used on EV1, which was the first modern EV made in 1996 [14], as shown in Figure 1.2. In 2007, Marin Soljačić from the Massachusetts Institute of Technology (MIT) proposed a mid-range WPT technology using magnetic resonance, which acted as a leading role in academia [15]. In 2009, Korean Advanced Research Institute (KAIST) developed the first-generation prototype of the On-Line Electric Vehicle (OLEV) project [16-17]. However, the EV market has seen great growth mainly in recent years due to the policy guidance, technology levels, and standards in force [5, 12].

Figure 1.2 GM EV1 inductively charging at a now-obsolete Magne Charge station [14]

In 2013, Elix Wireless used permanent magnet coupling power transfer (PMPT) technology as its 10-kW wireless charging solution [17-18]. In 2014, Vahle, in alliance with Hella, made foreign-object-detection free through low-field primary coils, which facilitated uninterruptible charging [19]. In 2015, the practicality of a novel WPT technology from Qualcomm Halo cooperated with UOA, was demonstrated on the BMW i8 safety car, reaching a power level of 7.2 kW [20]. Its Double D (DD) coils have also been integrated and tested on those safety cars, including Renault Fluence, Honda Accord, etc. [5, 12]. In 2016, Bombardier manufactured a high-power WPT system called PRIMOVE with a power capacity of up to 400 kW [12, 21]. Later, WPT technology designed for EVs was first commercialized by Tesla and Evantra. In 2017, Nissan announced cooperation with WiTricity and planned to equip fast wireless charging on the next generation of LEAF (Leading Environmentally-friendly Affordable Family car) in Figure 1.3 [22]. In 2022, Momentum Dynamics announced a dual-power breakthrough in automatic inductive charging (AIC) with enormous implications for the EV industry: a wireless system that provides the ability to charge light-duty EVs at both high (50-75kW) and low (7-22kW) power (presented in Figure 1.4) [23].

Figure 1.3 WiTricity WPT system with Nissan [22]

Figure 1.4 Momentum Dynamics WPT system [23]

Figure 1.5 shows the events in the development of WPT until now.

Ampere 1826 Discovery of the connection between current and magnets	Faraday 1831 Description of his law of induction	Maxwell 1864 Establishment of a theory of electromagnetism	Poynting 1884 Definition of Poynting's theorem	Hertz 1888 Discovery of electromagnetic waves	Tesla 1897 Transmission of microwave signals over 48 km
KAIST 2009 KAISR OLEV project	MIT 2007 Lighting up the bulbs over 2m using magnetic resonance	GM 1996 Magne Charge inductive charging on EV1	UOA 1993 Patent on non-contact power distribution	LBNL 1976 Introduction of the dynamic WPT	W. C. Brown 1964 First microwave power transmission system
Elix 2013 Applying PMPT technology to EVs	Vahle 2014 Foreign-object-detection free	Qualcomm 2015 Practicality of a novel WPT technology	Bombardier 2016 Manufacture of the PRIMOVE up to 400kW	Nissan 2017 Declaration of the cooperation with Witricity	Momentum 2022 Dual-Power Breakthrough in AIC

Figure 1.5 Events in the history and development of WPT [3-7]

1.2.2 WPT technologies for EVs

The available methods for WPT depend upon technology and transmission frequency, which can be categorized in Figure 1.6. Near-field type can be broadly divided into two categories:

capacitive coupling and inductive coupling. This type is adopted for applications where the distance between the transmitter and receiver is a few millimeters or centimeters. For example, Electric toothbrushes, charging portable devices, and Radio Frequency Identification (RFID) [3-7] are commercial technologies that are based on near-field WPT [12]. Far-field type is used to transmit power within distances up to several kilometers. It can be classified as microwave and radiofrequency, and optical power transfer techniques. Solar power satellites, powering drone aircraft, and charging wireless devices are established on far-field type WPT [3-12].

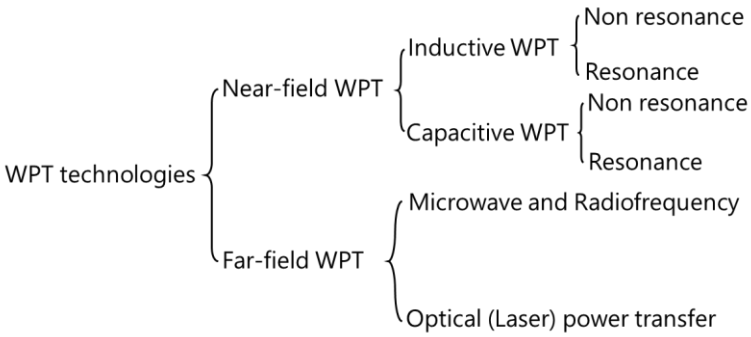

Figure 1.6 Classification of WPT technologies [3-5, 24]

The different WPT technologies are described below.

- Inductive WPT

  It (also called inductive power transfer (IPT)) is realized with the magnetic field of the electromagnetic wave. It can be divided into non-resonant IPT and resonant IPT (RIPT). According to Ampère's Law, a time-varying current in the transmitter generates a corresponding time-varying magnetic field around it. This time-varying magnetic field traverses the area of the receiver and induces an electric voltage E by Faraday's Law [4-5, 24], presented as a diagram in Figure 1.7:

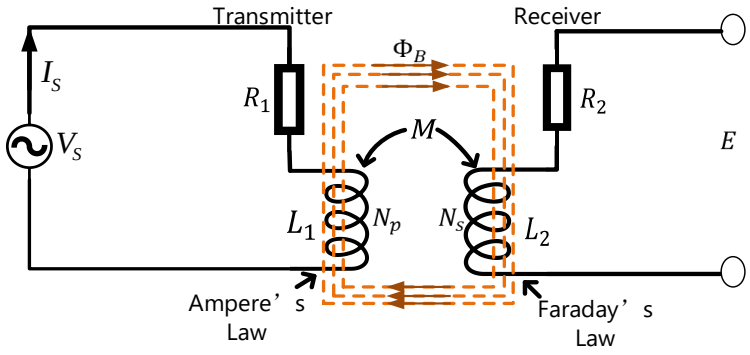

Figure 1.7 Equivalent circuit of an IPT [4-5, 24]

The electric voltage E can be expressed as below [4-5]:

$$E = -N_s \frac{d\Phi_B}{dt} \tag{1-1}$$

where E represents the induced voltage, Φ_B is the flux of the magnetic field passing in the area limited by the receiver, and N_s indicates the number of turns in the receiver. However, in this case, the air gap between the transmitter and the receiver may result in a very poor magnetic conductive environment.

The RIPT can be considered an improvement on IPT in which the electrical system is forced to work under resonant conditions [5, 12, 24]. The transmitter and the receiver are connected to structures composed of reactive elements such as capacitors or additional coils. These structures are referred to as compensation topologies. Figure 1.8 shows the generic diagram of a RIPT system. It transfers higher power than the IPT system, but it is extremely sensitive to the metallic obstacles that exist between the transmitter and the receiver [3-5, 28].

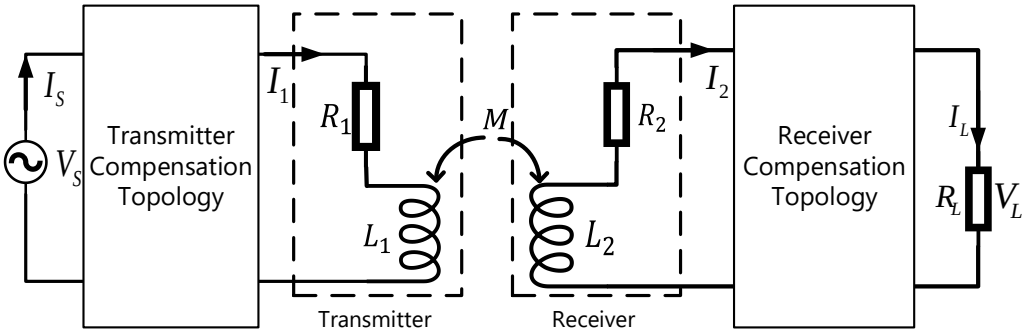

Figure 1.8 Generic diagram for a RIPT system [3-5, 24, 28]

- Capacitive WPT

It is achieved by means of the electrical fields between plates to transfer energy. A general circuit of the capacitive WPT system is shown in Figure 1.9, where two pairs of parallel metallic plates facing each other, acting as a transmitter and receiver, are connected in series and form a capacitive coupler [3, 24-25]. When an alternating voltage excitation is applied at the transmitter side, the electric flux density D between the metallic plates changes to form a displacement current I and achieve a wireless power transfer by Maxwell's full current theorem [24-25]. However, the capacitance C is small with air alone, so a common capacitor holds a dielectric between the plates to increase C [25]. The change in electric flux density $\frac{dD}{dt}$, that is, the change in the electric field $\frac{dE}{dt}$ (time derivative of the electric field) is important, as well as the change in the magnetic field at the time of electromagnetic induction [25-27].

$$\frac{dD}{dt} = \varepsilon \frac{dE}{dt} = \varepsilon_0 \varepsilon_r \frac{dE}{dt} \tag{1-2}$$

$$i = \frac{dD}{dt} S = \varepsilon_0 \varepsilon_r \frac{dE}{dt} S \tag{1-3}$$

where ε is the dielectric constant, ε_0 is the permittivity in a vacuum, ε_r is the relative permittivity, and S is the area where displacement current flows.

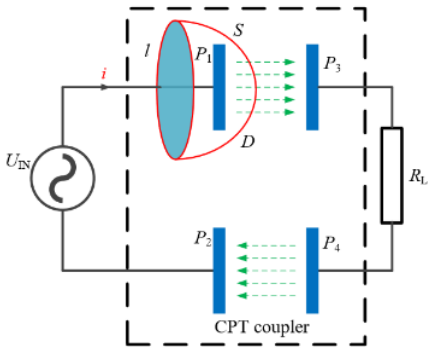

Figure 1.9 General Capacitive WPT circuit with a simplified coupling coupler [25-27]

Figure 1.10 shows a typical structure of a resonant capacitive WPT system, which is composed of an AC power supply, transmitter compensation topology, capacitive coupler, receiver compensation topology, and load. The compensation topologies are used to reduce impedance and increase power transfer efficiency [25-27]. The cost of capacitive WPT is cheaper than IPT and RIPT systems, but the transmission efficiency of resonant capacitive WPT is lower than RIPT systems [3-5, 28].

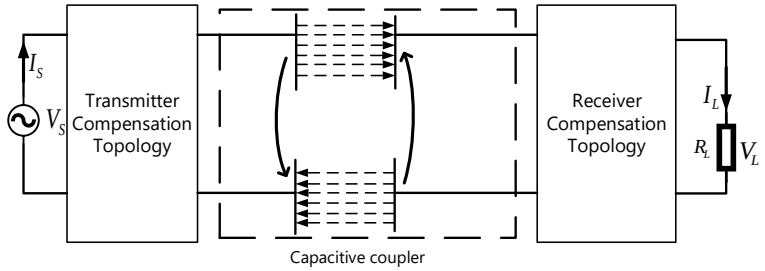

Figure 1.10 Generic diagram for resonant capacitive WPT [3-5, 24-28]

- Microwave and Radiofrequency WPT

It refers to WPT based on the microwave to transfer energy in a far-field context, which can also be extended to Radiofrequency (RF) signals with minor modifications. The generic structure of a microwave WPT is depicted in Figure 1.11. From a voltage source, a magnetron creates a microwave signal, and then it is sent through a transmitting antenna. The receiver processes the signal by means of a rectenna (antenna + rectifier) to convert the microwave signal to a DC signal. Finally, the DC signal is received by the power converter and is transferred to the load [5, 12, 24].

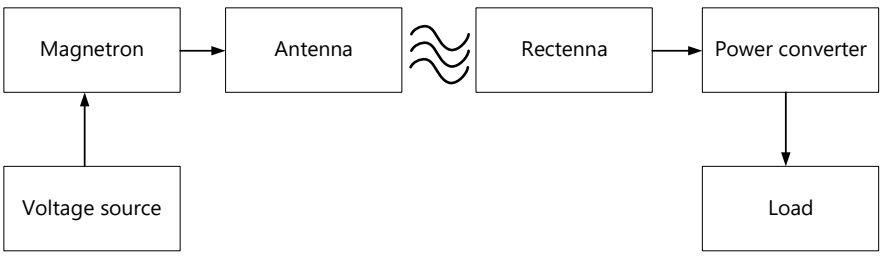

Figure 1.11 Generic structure of a microwave WPT [4-5, 24]

- Optical WPT

  Power is radiated in the form of electromagnetic waves; however, it is in the THz range and thus, exists as light [5]. This type of wave requires the power transmitter and the receiver to be in the line of sight; that is, without any intermediate obstacles, as the wave cannot traverse them [4-5, 12, 24]. A generic diagram of an optical WPT is shown in Figure 1.12. The transmitter consists of a laser diode which generates a light beam with particular power and wavelength. A beam director serves to adjust the direction of the power transfer. In the receiver, a photovoltaic (PV) panel converts the received light into power with the corresponding power converter. The DC power is then used to charge a load. It has the ability to transfer power to any point, but the temperature and materials of the PV cells will limit the performance of the system [4, 24].

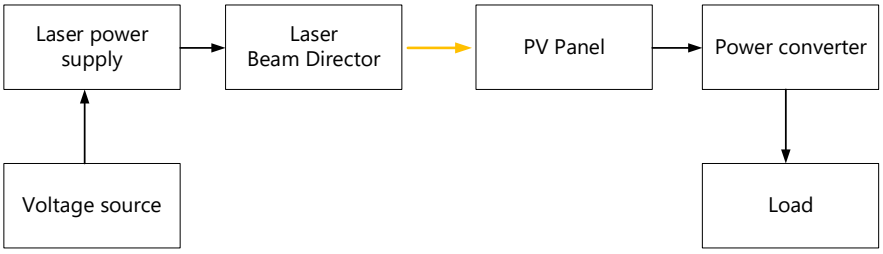

Figure 1.12 Generic structure of an optical WPT [4-5, 24]

Table 1.1 reveals some characteristics of the WPT technologies applied to EVs, such as the power level, airgap range, frequency, and so on [24-25, 28]. The power level and the efficiencies for inductive and capacitive WPT are higher than the ones obtained by the microwave and radiofrequency WPT and optical WPT, but the airgap range and frequency for inductive and capacitive WPT are lower than the ones obtained by the microwave and radiofrequency WPT and optical WPT.

Table 1.1 Comparative study of the WPT technologies applied to EVs [28]

WPT technology	Power level	Airgap Range	Frequency	Efficiency	Cost
Inductive WPT	High (Up to 100 kW)	< 30 cm	kHz to MHz	90-95%	Medium
Capacitive WPT	Medium (Up to 7 kW)	< 30 cm	kHz to MHz	80-90%	Low
Microwave and Radiofrequency WPT	Low (<250 W)	Up to several km	MHz to GHz	40-50%	High
Optical WPT	Low (<500 W)	Up to several km	>THz	1-15%	High

So far, WPT based on resonant transmission has reached a commercial status for EVs [4, 24, 28]. Considering different vehicles and power transfer techniques, the power levels and transmission efficiency of the RIPT system are higher in comparison with other resonant WPT technologies. Therefore, the main share of the WPT market for charging EVs is based on the principle of the RIPT system [4-5, 12, 24, 28].

1.2.3 RIPT operation modes

The flexibility offered by RIPT systems increases the situations in which EVs can be charged, not only when parked but also when temporarily stopped or even in motion. So, wireless charging operation modes can be done in three forms [4-5, 12, 24, 28]:

- Static RIPT

  It occurs when the charger takes place in a specific position, and the vehicle is expected to be turned off while a full charge is performed. This is the case with home chargers or those installed in car parks [4-5, 24, 28], as presented in Figure 1.13. Bombardier developed a RIPT charger for buses in Braunschweig, providing 200 kW in a static operation mode [4, 29], shown in Figure 1.14.

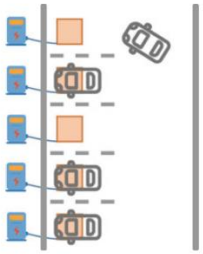

Figure 1.13 Static operation mode [4-5]

Figure 1.14 Bombardier RIPT charger for buses [29]

- Dynamic RIPT

  It refers to the charge that the transmitter positioned on the road and the receiver placed on the EV chassis to charge EVs in a motion (presented in Figure 1.15) [4-5, 30]. While implementing this mode, there are two kinds of transmitters: one is a large transmitter [30-33], and the other is multiple small transmitters [30, 34]. This type of charging promotes the Roadway Powered Electric Vehicle [35]. Dynamic charging has already been tested in some cities in South Korea (promoted by the OLEV project) [33], in Malaga (Spain) in the Victoria project [36], or in the city of Douai in France with the FastinCharge project [37]. They are illustrated in Figures 1.16-1.18.

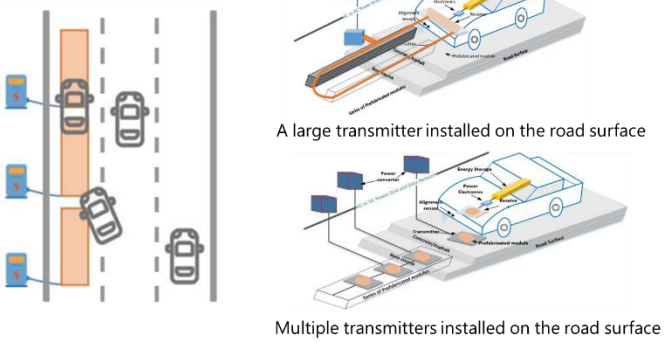

Figure 1.15 Dynamic operation mode [4-5, 30]

Figure 1.16 KAIST OLEV: dynamic wireless charging EVs with a large transmitter [33]

Figure 1.17 Dynamic charging EV system with multiple small transmitters [34]

Figure 1.18 Victoria project [36]

- Stationary (Quasi-Dynamic) RIPT

  This type of charge occurs with the following two particularities (shown in Figure 1.19). Firstly, the vehicle is stationary, but the engine is still running. Secondly, this situation holds over a short period of time that is not sufficient to reach a full charge. This type of charge is useful for public transport vehicles to receive energy when stopping at bus/tram stops or taxi ranks [4-5, 28, 35]. This was the case with the route-63 bus trialed in Mannheim (Germany) in 2013 [38]. The bus was able to charge its battery while picking up passengers without interrupting its service to recharge the battery. In Torino (Italy), Conductix-Wampfler has implemented a prototype to charge a bus when stopping and at the end of the bus route with RIPT technology (presented in Figure 1.20) [39]. Private vehicles could also be recharged during stops caused by traffic lights or conventional traffic patterns [35].

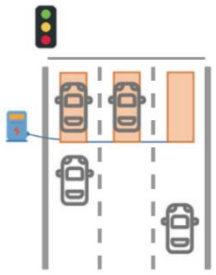

Figure 1.19 Stationary (Quasi-Dynamic) operation mode [4-5]

Figure 1.20 Conductix-Wampfler project [39]

1.2.4 Major standards

The promotion of EV wireless chargers requires their manufacturers to guarantee their interoperability in order to ensure that any vehicle can be charged at any charging site safely and efficiently [5, 12, 24]. To that end, they must comply with the requirements established by international institutions.

In the United States, the Society of Automotive Engineers (SAE) published the fourth version of SAE J2954 in 2020 [40]. The features of SAE J2954 are summarized in Table 1.2. In Europe, the IEC is the institution responsible for establishing standards through the IEC 61980 [41]. It focuses on the general requirements, communication, and magnetic field requirements, respectively, but shares mostly common information with SAE J2954. International Organization for Standardization (ISO) has defined the standards under ISO-19363 in close synchronization with SAE J2954 and IEC 61980 [42]. These organizations sets operating frequency as 85 kHz and 81.38 to 90 kHz as a band range, later extended to 79-90 kHz for light-duty vehicles.

Table 1.2 Features of SAE J2954 [40]

(a) WPT power classifications for light-duty vehicles

WPT power class	**WPT 1** **3.7 kVA**	**WPT 2** **7.7 kVA**	**WPT 3** **11.1 kVA**	**WPT 4** **22 kVA**
Minimum target efficiency at the aligned position	$> 85\%$	$> 85\%$	$> 85\%$	To be determined
Minimum target efficiency at the offset position	$> 80\%$	$> 80\%$	$> 80\%$	To be determined

(b) Z-class (Gap between the transmitter and the receiver)

Z-class	**Value [mm]**
Z1	100-150
Z2	140-210
Z3	170-250

(c) Positioning tolerance requirements for test stand

Offset direction	**Value [mm]**
ΔX	± 75
ΔY	± 100
ΔZ	Specified by manufacturer
Roll, Rotation, Yaw	$\pm 2, \pm 2, \text{and } \pm 6$ Degrees Respectively

The different power levels and air gaps create two serious issues. The first is that long-term exposures to time-varying electromagnetic fields (EMFs) can harm the human body. The second is a wide range of harmonics generated by inverters, which in turn create electromagnetic interference (EMI) issues on the other electronic devices' operations [43-44].

To prevent these adverse consequences, several organizations have documented and issued some guidelines to regulate the usage of the WPT systems. The International Commission on Non-ionizing Radiation Protection (ICNIRP) declares the recommendations for restricting field radiation and the limits to human body exposure. The ICNIRP 2010 recommended standards focus on frequencies ranging between 1 Hz-100 kHz, which covers almost wireless EV charging applications [45]. The new version of ICNIRP 2020 guidelines covers a frequency range between 100 kHz to 300 GHz [46]. However, the IEEE C95.1-2005 [47] and IEEE C95.1-2345-2014 [48] also offer safety levels with respect to human exposure to electric, magnetic, and electromagnetic fields from 0 Hz to 300 GHz.

The following table summarizes the whole standards mentioned above to be followed for EV WPT chargers.

Table 1.3 Standards for EV WPT chargers

Standard	Title/ Description
SAE J2954	Wireless Power Transfer for Light-Duty Plug-In/Electric Vehicles and Alignment Methodology
IEC 61980	Electric vehicle wireless power transfer (WPT) systems
ISO 19363	Electrically propelled road vehicles—Magnetic field wireless power transfer—safety and interoperability requirements
ICNIRP 2010	ICNIRP Guidelines for limiting exposure to time-varying electric and magnetic fields (1 Hz – 100 kHz)
ICNIRP 2020	ICNIRP Guidelines for limiting exposure to time-varying electric and magnetic fields (100 kHz – 300 GHz)
IEEE C95.1-2005	IEEE Standard for Safety Levels with Respect to Human Exposure to Electric, Magnetic, and Electromagnetic Fields, 0 Hz to 300 GHz
IEEE C95.1-2345-2014	IEEE Standard for Military Workplaces–Force Health Protection Regarding Personnel Exposure to Electric, Magnetic, and Electromagnetic Fields, 0 Hz to 300 GHz

1.3 Design of RIPT system

Figure 1.21 shows the block diagram of a RIPT system for EVs. The electrical network provides a DC-link voltage for the system through the AC/DC converter with power factor correction. The system consists of a transmitter, a receiver, converters, and resonant compensation networks for the transmitter and the receiver. The magnetic field produced by the transmitter induces an alternating field in the receiver. The AC power is then rectified in order to charge the battery. Compensation topologies are added to the transmitter and the receiver to create the resonant case and reduce additional losses [5, 12, 24, 30].

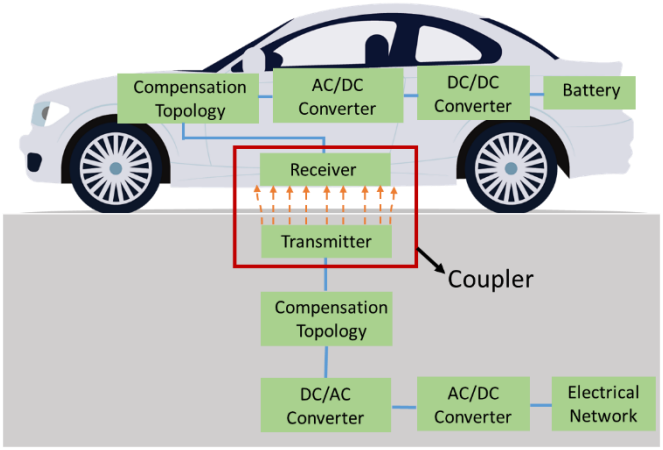

Figure 1.21 Block diagram of a RIPT system

As shown in Figure 1.21, the magnetic coupler (transmitter and receiver indicated in the red framework), the transmission distance (air gap), the compensation topologies, and the misalignment between the transmitter and the receiver directly influence the performance of the system. The performance includes transmission efficiency, magnetic flux density leakage, and the cost of the system.

1.3.1 Magnetic coupler design

The magnetic coupler is the most part of the RIPT system, which normally includes a pair of coils, the magnetic cores, and the shielding. Air-core coupler has a serious drawback in that its electrical parameters are very sensitive, especially when there are ferromagnetic objects in proximity [5, 12, 49-50]. To address this problem, the magnetic cores work as a magnetic flux guide, and they are made of ferrite [49-50]. The shielding is used to prevent magnetic flux density leakage. An example of the circular coupler from the literature is presented in Figure 1.22.

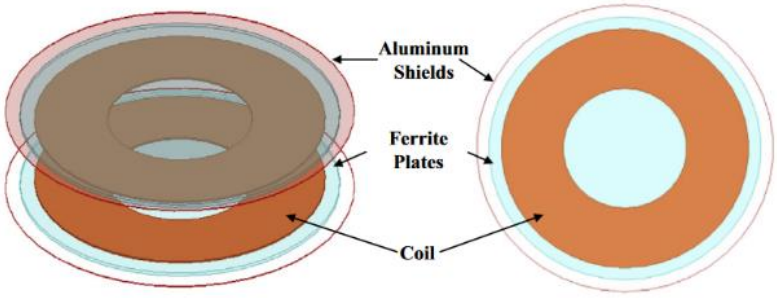

Figure 1.22 An example of the circular coupler [51]

Several coil shapes of the magnetic coupler have been proposed and evaluated in the literature so far because the geometry and configuration of the coils are crucial for determining the transmission efficiency of the RIPT system and its magnetic flux density leakage. In Figure 1.23, (a), (b) and (c) are used today due to their simplicity [4-5, 49-50]. However, other complex geometries (d), (e), (f) have been proposed with the goal of offering a lower sensitivity to coil misalignment [49-50]. Double-D (DD) coils are composed of two equal D-shaped (rectangular)

sub-coils with a shared side [55]. Based on the DD coils, the DD quadrature (DDQ) is implemented. It has two independent windings: one is a DD pair of coils, and another is the quadrature or quad (Q) coil. The Q-coil is placed over half of the area of each D coil [55]. Bipolar coils are similar to DD coils, but one of the coils overlaps half of the area of the D-shape coil [56]. In order to further improve misalignment tolerance and transmission efficiency, many researchers also designed other multiple coils, such as tri-polar coils [57-58], multi-transmitters-one receiver [59], dual transmitters-dual receivers [60], and so on. References [4-5, 28, 49-50, 61] compared most of the structures of coils on several factors (including coil shape, misalignment, system complexity, interoperability, and flux leakage).

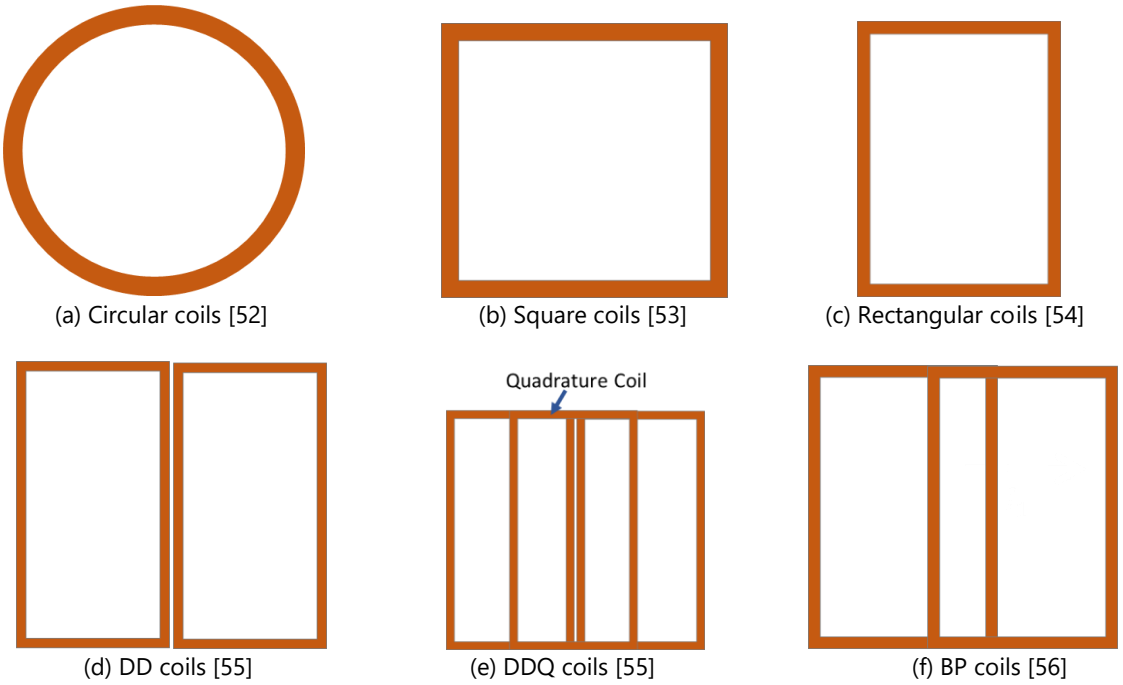

(a) Circular coils [52] (b) Square coils [53] (c) Rectangular coils [54]

(d) DD coils [55] (e) DDQ coils [55] (f) BP coils [56]

Figure 1.23 Coil geometries

After, ferrites are added to the coils, which aims for proper flux guidance to increase the mutual inductance, minimizes leakage inductance, and also work as the magnetic shielding to decrease the magnetic flux density leakage [49-50]. According to [5, 12, 49-50, 61], there are several basic shapes of ferrite, shown in Figure 1.24 (orange presents the input current, the black presents the output current). However, because of the high cost, fragile, heavyweight, and sensitivity to misalignment, many researchers proposed plate-shaped structures, which are lighter and easier to manufacture.

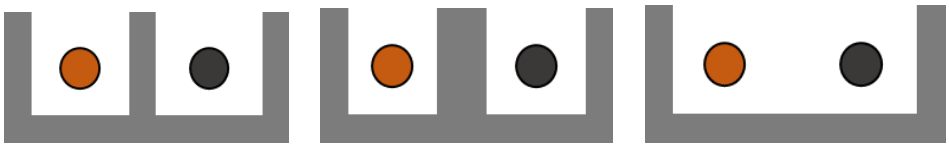

(a) E-type (b) W-type (c) U-type

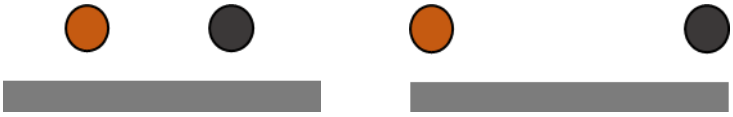

(d) Plate-type

Figure 1.24 Ferrite basic shapes [5, 49-50, 61]

Furthermore, the design of a RIPT system must be compliant with international standards to reduce the EMF leakage to allowable levels as defined in [40]. Shielding is usually placed above the receiver to minimize the leakage flux around the system, thus improving the coupling performance and leading to better efficiency and quality factor [61-63]. Different types of shieldings have been reported in the literature: passive (magnetic, conductive, or both) [64-70], active [71-73], and reactive resonant [74-76].

- passive shielding

  It is effective with magnetic materials [66-68] or conductive materials [63], or combining them together [69-70]. Some of the IPT systems take the vehicle chassis as conductive material for shielding [78]. This method improves the system efficiency and significantly reduces EMF level to some extent, but it alters the receiver inductance and the mutual inductance. It also causes a heat problem on the metallic sheet due to the eddy-current losses [61, 65]. Some examples of passive shielding are shown in Figure 1.25 (a), (b), (c) [77].

- active shielding

  It involves extra coil turns (shielding turns) wounded in the reverse direction to create a magnetic field in a reverse direction to the original magnetic field created by the coupler to minimize the EMF leakage [64, 71]. An example of active shielding is indicated in Figure 1.25 (d) [77]. The main challenges in this method are positioning and sizing of shielding coils, the control system needed for the controlling current flowing through the shielding coils, and the increasing cost and weight of the system [71-73].

- reactive resonant shielding

  It can be considered as a particular feature of the active shield to avoid the extra source for inducing field in the shielding turns. It incorporates additional reactive components (e.g., capacitor), and the coil turns close to the transmitter coils, but their current excitation comes from the magnetic field naturally generated by the transmitter coil [74-76]. Current flowing in shielding coil turns opposite magnetic field to oppose leakage flux. The magnetic field depends on the resonant capacitor and the number of turns added. The opposite field can't be controlled as an active shielding method and needs more current in the shielding coil turns [79]. The fifth generation of the OLEV project has developed three different implementations of reactive resonant shielding [76], as seen in Figure 1.25 (e).

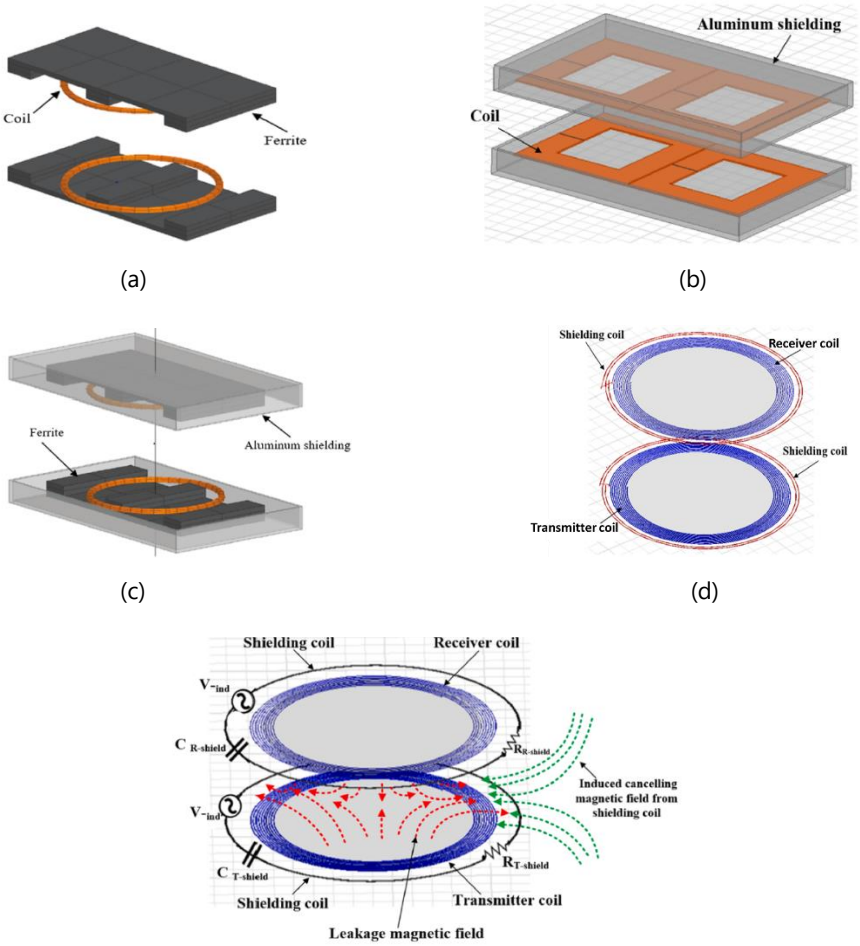

Figure 1.25 Types of shielding in the RIPT system, (a) passive magnetic, (b) passive conductive, (c) passive conductive and magnetic, (d) active, and (e) reactive resonant

Then, four shapes of coils (circular, square, DD, and BP) that incorporate the ferrite plates and the passive conductive and magnetic shielding for the RIPT system are applied in this thesis. Because these coil shapes are the basis of other complex coil geometries, and they have been proposed by a previous PhD thesis [80] and developed in the GeePs laboratory.

1.3.2 Compensation topologies

Except for the design of the magnetic coupler, the compensation topology plays a major role in the RIPT system. Due to the dimensions of the coils, the parasitic capacitance is not sufficient to ensure resonance in the operational frequency range [3-5, 24, 30]. Consequently, additional reactive structures, known as the compensation topologies, are incorporated into the transmitter and the receiver coils to adjust the operating frequency [4-5, 24, 49-50, 61]. So this minimizes the reactive power supply and improves both the transmission efficiency and the power transfer capability.

According to [3-5, 12, 50, 61, 81], there are four basic compensation topologies, which can be achieved by adding one capacitor in series/parallel to the transmitter and the receiver coils. Resonant capacitors C_1 and C_2 are connected to the transmitter or the receiver (L_1, L_2 represents the self-inductance of the transmitter and the receiver coils; R_1, R_2 represents the resistance of the transmitter and the receiver coils; M is the mutual inductance between the transmitter and the receiver), either in parallel or in series. So, it exists four principle topologies of the resonant circuit in the RIPT system: series-series (SS), series-parallel (SP), parallel-series (PS), and parallel-parallel (PP), shown in Figure 1.26. Their features are summarized in Table 1.4.

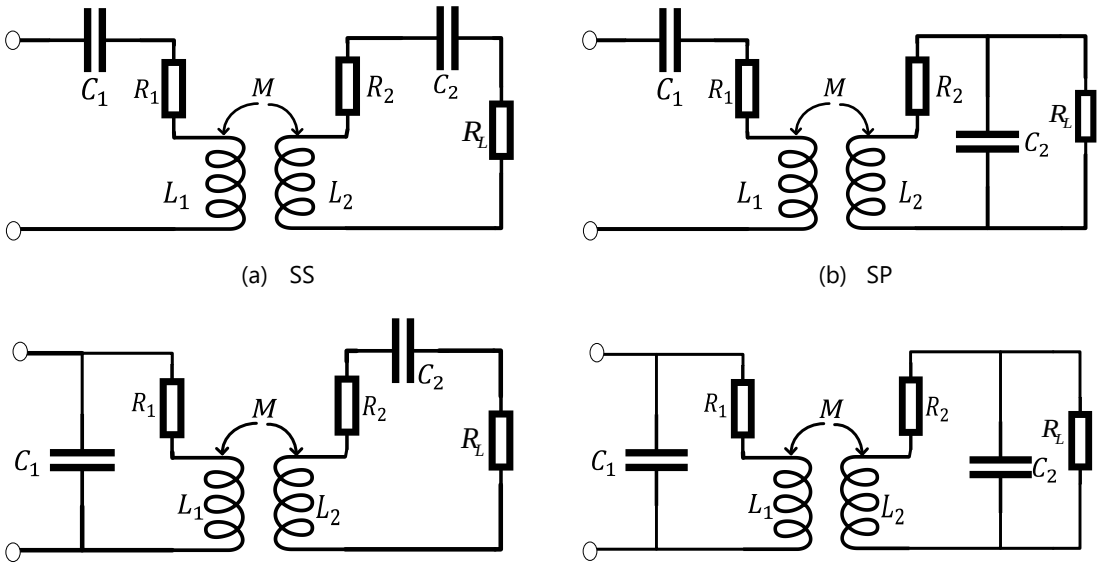

(a) SS (b) SP

(c) PS (d) PP

Figure 1.26 Basic compensation topologies [3-5, 50, 61, 81-82]

Table 1.4 Features of basic compensation topologies [5, 12, 50, 61, 81-82]

Basic compensation topology	**Resonant capacitor C_1, C_2 (w_0 is the resonant angular frequency)**	**Features**
SS	$C_1 = \frac{1}{w_0^2 L_1}$, $C_2 = \frac{1}{w_0^2 L_2}$	Capacitance values are independent of the coupling coefficient and the load; Slightly sensitive to the misalignment;
SP	$C_1 = \frac{L_2}{w_0(L_1 L_2 - M^2)}$, $C_2 = \frac{1}{w_0^2 L_2}$	The transmitter capacitance value is dependent on the coupling coefficient; Moderately sensitive to misalignment;
PS	$C_1 = \frac{L_1 + w_0^2 R_L}{w_0^2(w_0^2 M^4 + L_1^2 + w_0^2 L_1 R_L)}$, $C_2 = \frac{1}{w_0^2 L_2}$	The transmitter capacitance value is dependent on the coupling coefficient and the load; Highly sensitive to misalignment;
PP	$C_1 = \frac{L_2^3(L_1 L_2 - M^2)}{(L_1 L_2 - M^2)^2 w_0^2 L_2^2 + M^4 R_L^2}$, $C_2 = \frac{1}{w_0^2 L_2}$	The transmitter capacitance value is dependent on the coupling coefficient and the load; Highly sensitive to misalignment;

But, some factors (like misalignment, frequency deviation, etc.) make RIPT systems never function under ideal conditions. Using multiple elements in a series-parallel combination makes an effective compensation method to overcome the challenges of the basic compensation topologies mentioned above. The multi resonant compensations like LCC-LCC, LCL-LCL, etc., over their full range of loading and coupling, offer high efficiency [83-86]. However, additional elements may cause additional losses compared to mono resonant compensation, particularly for high power applications [87-88].

However, the SS topology is often implemented in the RIPT system. The advantage is that resonant capacitors don't depend on load variation and coupling coefficient, and it makes them less sensitive to the misalignment between the transmitter and the receiver compared to the other topologies [3-5, 87]. This condition is very useful in the static or dynamic RIPT system.

1.3.3 Optimization of RIPT systems

When the magnetic coupler design and compensation topology are selected, how to optimize the design for IPT systems is under current research. There are three engineering design methodologies to select the optimal design for the system:

- Parameter optimization: It allows for doing a parametric sweep on geometry dimensions or material properties, such as the ferrite length and width, coil wire position, number of coil turns, a separation between turns, size and position of ferrites, etc. [51, 55, 88-106].

- Shape optimization: It allows to deform the boundaries of the geometry, such as the coil shape, the ferrite shape, or the shielding shape;

- Topology optimization (TO): It allows to determine whether a certain point of the geometry is void or solid, for example, how to arrange the ferrite structure under the transmitter or above the receiver [107-110]. The main methods used are the solid isotropic material with penalization (SIMP) method [111], the on-off method [112], and so on.

To compare the performances of different possible designs, many researchers have considered the uncompensated power rating P_{su}, the coupling coefficient k [90-92, 95, 99-100], the kQ factor (Q is the coil's quality factor) [91], power density α [89, 97, 105], gravimetric power density γ [97], transmission efficiency η [89, 97, 101, 105-106], mutual inductance M [103], cost [92, 105-106], core losses [94, 101, 103], magnetic field leakage $B_{leakage}$ [91, 95-96], output power P_{out} [106], weight [100-101] and so on as objective functions for optimization. Most of them uses parametric sweep [51, 55, 89, 93-94, 97, 99-101, 104-105], while some literatures considered optimization algorithms such as Genetic Algorithm (GA) [90, 95-96, 98, 103], Particle Swarm Optimization (PSO) [91, 106], Tabu Search [92] and so on [102].

Table 1.5 summarizes the work on the optimization of RIPT systems, and they are compared on the objective functions, the number of design variables, coil shape, optimization method, misalignment analysis, and Pareto fronts.

Table 1.5 Optimization of RIPT systems

Article	Year	WPT type	Objective functions	Design variables	Coil shape	Optimization Method	Misalignment Analysis	Pareto fronts
[51]	2011	Static RIPT	P_{su}	3	Circular	Sweep	✓	×
[55]	2013	Static RIPT	P_{su}	5	Circular, DD, DDQ	Sweep	✓	×
[89]	2015	Static RIPT	η, α	3	Circular	Sweep	×	✓
[90]	2017	Static RIPT	k, Q, P_{out}	3	Circular	GA	×	✓
[91]	2017	Static RIPT	k, kQ, B_{max}	11	Circular	PSO	×	✓
[92]	2018	Static RIPT	$Cost + k_{avg}$	3	DD	Tabu Search	✓	×
[93]	2018	Static RIPT	Q	4	Circular	Sweep	×	×
[94]	2019	Static RIPT	Core losses	10	DD	Sweep	×	×
[95]	2019	Static RIPT	$k, B_{leakage}$	1	Circular	GA	×	×
[96]	2019	Static RIPT	$B_{leakage}$	11	Circular	GA	×	×
[97]	2019	Static RIPT	η, α, γ	9	Circular, Rectangular, DDQ	Sweep	✓	✓
[98]	2020	Static RIPT	Wire length	4	Circular	GA	×	✓
[99]	2020	Static RIPT	k	3	Solenoid	Sweep	✓	×
[100]	2021	Static RIPT	$V_{ferrite}, k$	3	Circular	Sweep	✓	✓
[101]	2021	Static RIPT	$\eta, Core\ loss, Weight_{system}$	2	Circular, square, DD	Sweep	×	×
[102]	2022	Static RIPT	$\eta_{aligned}$, $\eta_{misaligned}$	11	Rectangular	MOO	✓	✓
[103]	2022	Static RIPT	$\eta, Core\ loss,$	5	Square	GA	×	×
[104]	2019	Dynamic RIPT	M	2	DDQ	Sweep	×	×
[105]	2021	Dynamic RIPT	$\eta, \alpha, Cost$	4	Rectangular	Sweep	×	✓
[106]	2021	Dynamic RIPT	$Cost_{norm}, \eta, P_{out}$	6	Rectangular	PSO	✓	✓

Up to now, the methods to express objective functions in optimization algorithms are:

1) To deduce the mathematical expressions describing the relationships between the design variables and the objectives (such as self-inductances, mutual inductances, magnetic flux density leakage, and so on);

2) To simulate every design configuration based on 3D numerical methods, e.g., the Finite Element Method (FEM).

But when a complex coupler configuration with a large number of variables is involved in the design process, the first method will become very difficult to deduce the analytical expressions, and the second method will take a really long time to simulate all possible design configurations

by 3D FEM. How to speed up the optimization process with a large number of variables in an efficient method is worth studying.

1.4 Metamodeling analysis of RIPT systems

During the development of the RIPT system, accurate 3D models are needed, able to correctly describe the geometry, the materials (e.g., coils, ferrites, and vehicle chassis), and the phenomena involved (e.g., the effect of transient electromagnetic phenomena) with the operating frequency between 10 and 100 kHz. However, the computational cost of 3D models based on volumetric meshes (FEM, finite difference method, etc.) is rather high.

Several metamodeling techniques have been developed to describe the relationship between the input variables and the observed output, such as Support Vector Regression (SVR) [113], Multigene Genetic Programming Algorithm (MGPA) [114], Polynomial Chaos Expansions (PCE) [115], and so on. They have been applied to generate several metamodels that are trained with a limited set of samples. But, how to choose training samples effectively and define internal parameters for the metamodeling techniques depends on the studied system and the range of variability of the input variables.

Reference [116] applies the SVR, the least-squares support vector machine (LS-SVM) regressions with polynomial and Gaussian radial base function (RBF) kernels, and the PCE method to predict the impact of 30 uncertain parameters on the maximum efficiency of a WPT application in the bandwidth 500 MHz to 1.5 GHz. In [117], it derives low-complexity behavioral analytical models of the mutual inductance between the couplers of WPT systems as functions of their reciprocal position by means of the MGPA method. In [118], a MGPA metamodel is investigated to express the self-inductance and the mutual inductance versus geometrical parameters of the ferrite and coils for the WPT system. Reference [119] uses an analytical, behavioral model that relates mutual inductance between the coil pair to their relative positions along the actual vehicle trajectory for a dynamic WPT system. In [120], it adopts the parametric model order reduction technique with the Monte Carlo (MC) approach to quantify how and how much the uncertainties on the components and material parameters of a WPT system for the static charge of EVs affect the overall efficiency and functionality of the final produced device. It is based on a standard system among the ones provided by the current SAE J2954 recommended practice.

Although these articles have verified the feasibility of the metamodeling techniques in WPT systems, there is no research to compare which metamodeling technique is the most suitable for the RIPT system among SVR, MGPA, and PCE methods. Moreover, the post-process of the PCE approach-sensitivity analysis [121] is not taken into account to analyze how the input variables impact the system performances. Besides, metamodeling techniques allow to compare at low cost the performance of different shaped couplers for the RIPT system.

1.5 Objective and goal of the thesis

Although RIPT systems are now widely studied, there are still several challenges in designing the magnetic coupler. The existing methods for design optimization consist to simulate every possible design configuration based on 3D FEM or deduce the analytical expressions for solving the electromagnetic problem involving the RIPT system and the nearby environment. They can give reliable results, but when given a large number of design variables, the complex design configurations based on 3D FEM will take a lot of computational time, and the analytical expressions are really difficult to deduce. Until now, there is no comprehensive methodology allowing a fast, reliable, and efficient design and optimization for it. Meanwhile, adequate methodologies have to take into account the environment of the system, including the impact of the car chassis, bitumen around the primary coil, and presence of the human body since it is needed to evaluate the level of electromagnetic exposure in order to be compliant with the international standards. In this situation, the introduction of metamodeling techniques allows for dealing with the variability of all the parameters describing the electromagnetic problem.

The operating parameters of the RIPT system studied in this thesis work are listed in Table 1.6 [80].

Table 1.6 RIPT operating parameters

Parameter	**Value [Unit]**
Operating frequency f_0	85 [kHz]
Transmitting power	2.5 [kW]
Transmitting coil current (RMS value)	42 [A]
Air gap	150 [mm]

Our contribution will focus on the following parts to study this RIPT system:

- Analyzing the maximum transmission efficiency η_{max} of the RIPT system with the SS compensation topology, and deducing that the η_{max} is only connected to the ratio between the wire length of the transmitter coil and the mutual inductance between the transmitter and the receiver when the transmitter and the receiver are identical;
- Verifying the agreement for different small-scaled magnetic couplers (Circular, square, DD, and BP) between COMSOL 3D FEM simulations and the experiments, including the electrical parameters (mutual inductance, η_{max}) and the magnetic flux density distribution around the system;
- Comparing SVR, MGPA, and PCE metamodeling techniques for analyzing the mutual inductance of square couplers, taking into account the sources of uncertainty;
- Selecting the PCE metamodeling technique due to its accuracy and character to do the sensitivity analysis and discussing how the sources of uncertainty influence the mutual inductances and the maximum transmission efficiency of small-scale couplers (circular, square, DD, and BP) based on PCE metamodels;

- Comparing multiobjective optimization methods (Non-dominated Sorting Genetic Algorithm II (NSGA-II) [122] and Multiobjective Particle Swarm Optimization (MOPSO) algorithm [123]) with the PCE metamodeling technique to find the best dimensions of a practical RIPT system under perfect alignment conditions, taking into account both the transmission efficiency and the volume (ferrite)/ the cost (ferrite + aluminum plates) of the system;
- Performing TO based with SIMP method to appropriately place the ferrite in the previously optimized dimension considering the volume constraint.

1.6 Conclusion

This chapter presents some pieces of literature concerning wireless charging for EVs.

Firstly, the development of WPT technology has been introduced in the past few decades until now. Then, the WPT technologies, operation modes, and main standards for EVs are briefly concluded. With regard to EVs, RIPT technology is widely used. At the same time, SAE J2954 and ICNIRP 2010 are always taken into account when designing the system.

Secondly, the RIPT system used in EVs is generally described. During the design process, the magnetic coupler and compensation topologies have an effect on the performance of the system, including the efficiency and the EMF leakage. To better design the system, several optimization methods with different objective functions are also summarized. But when a complex coupler configuration with a large number of variables is involved in the optimization process, the analytical expressions that describe the relationships between the design variables and the objectives will be very difficult to deduce. On the other hand, simulating all possible design configurations by the 3D FEM method will take a really long time. How to speed up the optimization process with a large number of variables in an efficient method is worth studying.

Thirdly, some metamodeling techniques are verified to be feasible in RIPT systems, such as SVR, MGPA, PCE, and so on. But there is no research to compare which metamodeling technique is the most suitable for the RIPT system among SVR, MGPA, and PCE methods. Moreover, the post-process of some metmodeling approaches-sensitivity analysis is not taken into account to analyze how the input variables impact the system performances dring the optimization process. Besides, metamodeling techniques allow to compare at low cost the performance of different shaped couplers for the RIPT system.

Finally, according to the existing problems from the literature, the objective and aim of the thesis are described. In addition, the contributions of the thesis work are also presented.

CHAPTER 2 COUPLER ANALYSIS AND RESULTS

2.1 Introduction

A RIPT system consists of a pair of coils that are magnetically coupled through an airgap, which the transmitter is installed on the road surface, and the receiver is placed on the vehicle. The geometry of the coils is crucial for determining the magnetic field of the RIPT system and its transmission efficiency. Additionally, the electrical parameters of the coils will determine the configuration of the compensation networks. For these reasons, coil design is one of the most important steps in the complete definition of an EV RIPT charger [3-5, 24, 35].

Until now, some reviews have summarized and discussed different structures and shapes of the coils [4-5, 49-50, 61]. Reference [51, 80, 97, 124-130] explored the variation of the coupling coefficient for different shapes of couplers under different air gaps and coil misalignments. Reference [131] presented the coupling coefficient and the magnetic flux leakage on a circular coupler. However, they did not compare the coils for the transmission efficiency and magnetic flux density leakage around the RIPT systems at the same time.

In this chapter, four different shapes of couplers are presented and studied, which are well-known and widely used in RIPT systems [3-5, 24, 49-50, 61]:

- Circular coupler;
- Square coupler;
- Bipolar (BP) coupler;
- Double-D (DD) coupler.

The main aim of this chapter is to study the maximum transmission efficiency and magnetic flux density leakage for these shapes of couplers. These different coupler configurations are analyzed with the effect of the misalignment between the transmitter and the receiver.

For the simulation, the COMSOL Multiphysics® software is used [132]. It is a powerful and flexible simulation tool for investigating electromagnetic fields and electromagnetic interference /electromagnetic compatibility by solving Maxwell's equations. The simulations presented in this thesis are supported by COMSOL V5.6 on an Intel Xeon W-2125 processor.

The experimental validation is carried out on 1:10 scale prototypes developed in the GeePs laboratory. These prototypes are made on the basis of homotheticity with respect to the real-scale coupler to save manufacturing costs. The mutual inductance and magnetic flux density leakage are carefully studied and compared in the following sections.

2.2 RIPT system analysis

Generally, due to the large air gap of the IPT system, the magnetic coupling of IPT coils is low when compared with a traditional transformer [3-5, 24, 49-50]. In order to achieve a high transmission efficiency despite the high leakage inductance, a resonant compensation to the transmitter and the receiver is needed. According to [3-5, 24, 49-50, 61, 133-134], the SS compensation is suitable for EV both static and dynamic IPT systems, and the condition of resonance in the SS compensation remains constant, independently of the variations of the mutual inductance and the load. So, Figure 2.1 shows the electrical circuit in the SS compensation topology for the RIPT system. L_1, L_2 represent the self-inductances of the transmitter and the receiver; C_1 and C_2 are the resonant capacitances connected to the transmitter and the receiver coils in series respectively; R_1, R_2 represent the resistances of the transmitter and the receiver; I_1, I_2 represents the current of the transmitter and the receiver, R_{L} is the load of the system.

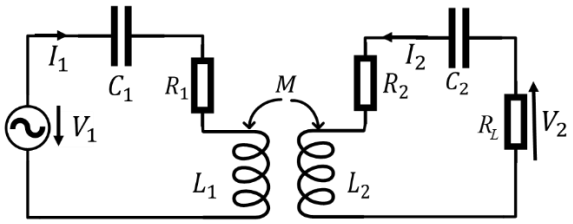

Figure 2.1 Electrical circuit in the SS compensation topology [24, 49-50, 61, 133-134]

Using the definition given in [89, 135], the coupling coefficient k is defined by the ratio of the mutual inductance M (between the transmitter and the receiver) and the geometric mean of the two self-inductances $L_1$and L_2:

$$k = \frac{M}{\sqrt{L_1 L_2}} \tag{2-1}$$

The transmitter and the receiver coil quality factors are defined as [135]:

$$Q_i = \frac{wL_i}{R_i} \tag{2-2}$$

where $i = 1,2$ stands for the transmitter and the receiver respectively, and w represents the angular frequency.

Moreover, the system quality factor Q is defined as the geometric mean of the two coil quality factors $Q_1 and\ Q_2$ [89, 131, 135].

$$Q = \sqrt{Q_1 Q_2} = w\sqrt{\frac{L_1 L_2}{R_1 R_2}} \tag{2-3}$$

So, the equation to calculate the maximum transmission efficiency η_{max} of the RIPT system in Figure 2.1 can be achieved as below [131, 135] ($R_L = \sqrt{R_2^2 + \frac{R_2 (w_0 M)^2}{R_1}}$, more details are in Appendix A):

$$\eta_{max} = \frac{R_L I_2^2}{R_1 I_1^2 + R_2 I_2^2 + R_L I_2^2} = \frac{(w_0 M)^2}{(\sqrt{R_1 R_2} + \sqrt{R_1 R_2 + (w_0 M)^2})^2} = \frac{(kQ)^2}{(1+\sqrt{1+(kQ)^2})^2} \approx 1 - \frac{2}{kQ} \quad (2\text{-}4)$$

where $w_0 = w = \frac{1}{\sqrt{L_1 C_1}} = \frac{1}{\sqrt{L_2 C_2}}$, $kQ \gg 2$.

Furthermore, the equation of the maximum transmission efficiency η_{max} can be simplified as below when the transmitter and the receiver are identical (same resistance):

$$\eta_{max} \approx 1 - \frac{2}{kQ} = 1 - \frac{2\sqrt{R_1 R_2}}{w_0 M} = 1 - \frac{R_1}{\pi f_0 M} = 1 - \frac{\rho}{\pi f_0 S} \frac{l}{M} \quad (2\text{-}5)$$

where $w_0 = 2\pi f_0$, l is the coil conducting wire length, S is the cross-sectional area of the conducting wires of the coil, ρ is the electrical resistivity of these wires.

Equation (2-5) highlights the impact of the ratio between the wire length l and the mutual inductance M on the RIPT maximum transmission efficiency η_{max}. By further inference, the maximum transmission efficiency η_{max} is only affected by the mutual inductance M for a given wire length and the resonant frequency.

According to the operating parameters of the RIPT system considered in the thesis, the external dimensions of the transmitter coil and the receiver coil are fixed as $468\ \text{mm} \times 468\ \text{mm}$, which are proposed to be mounted on the EV. The air gap between the transmitter and the receiver is chosen as 150 mm, and the resonant frequency f_0 is defined as 85 kHz. These parameters are defined by a previous PhD thesis [80]. In fact, a realization of a real-scale coupler used in EVs is costly, especially considering the price of the materials used (wire and ferrite). So, to save construction time and cost, the studied coils are not built with a real size but miniaturized on a scale of 1:10 in the following section.

2.3 Small-scale coupler analysis

The circular coupler, square coupler, DD coupler, and BP coupler in small-scale shapes are shown in Figure 2.2. The current I_1 in the transmitter generates the magnetic flux through the receiver. The coils of the coupler are made of Litz wires with six turns distributed in two layers. The Litz wires are conductive wires suitable for transporting high-frequency current, reducing the skin effect, and reducing the proximity effect [136-139]. Here, the chosen Litz wires are made up of 105 strands electrically insulated from each other and braided together to form the final wires [80, 137]. The diameter of the strand is chosen to be 0.04 mm so that it is smaller than the skin depth at the operating frequency. Then, the parameters of the small-scale couplers are shown in Table 2.1.

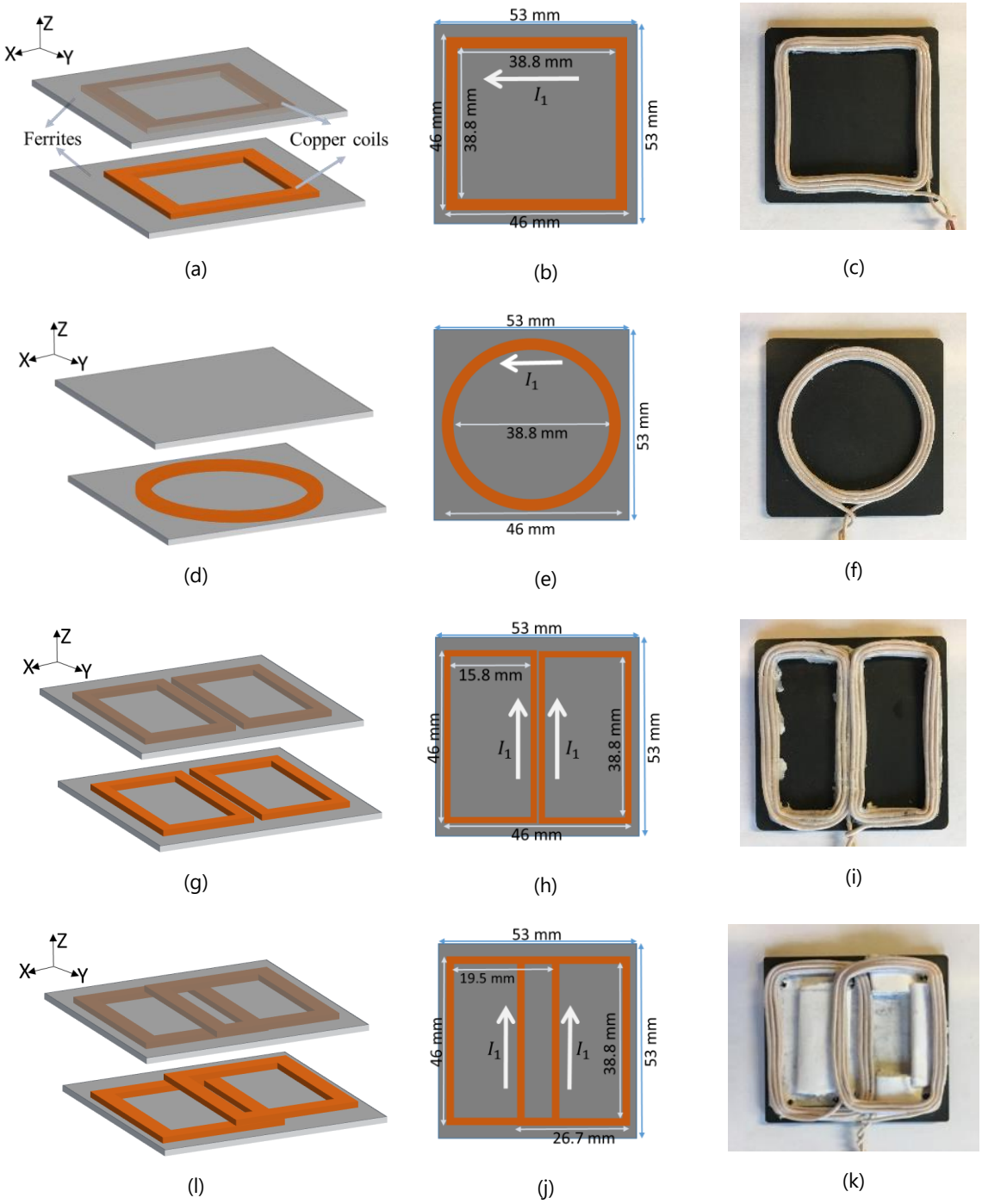

Figure 2.2 Different shaped couplers (a), (d), (g), (l): Description of the coupler; (b), (e), (h), (j): Dimensions of the different couplers: square, circle, DD and BP; (c), (f), (i), (k): Prototypes made in the laboratory (square, circle, DD and BP).

In order to observe how the coupler shapes influence the performances of the RIPT system, the mutual inductance, and the magnetic flux density leakage are studied and compared below in the simulations and the experiments.

Table 2.1 Parameters of the small-scale coupler coils

Parameter	Value [Unit]
Width of the coils	3.6 [mm]
Coil thickness	2.4 [mm]
Ferrite thickness	2 [mm]
Relative permeability of ferrite	2500
Cross-sectional area of the wires S	0.95 $[mm^2]$
Resistivity of the wires ρ	1.7×10^{-8} $[\Omega \cdot m]$
Wire length of Square coils l_{square}	93.1 [cm]
Wire length of Circular coils l_{circle}	73.1 [cm]
Wire length of DD coils l_{DD}	131.0 [cm]
Wire length of BP coils l_{BP}	139.9 [cm]
Air gap between the transmitter and the receiver	15 [mm]

2.3.1 Maximum transmission efficiency evaluation

We will focus on the evaluation of the maximum transmission efficiency on these four couplers. A comparison in terms of efficiency will be presented in the simulations and the experiments. Moreover, the influence of the misalignment on efficiency will also be taken into account.

2.3.1.1 Modeling and experiments for the mutual inductance

Before doing the experiments for the mutual inductance, it is necessary to know the value of the mutual inductance in the simulation for further comparison. In the COMSOL simulation, the coils are modeled as homogenized multi-turn numeric coils, where the current flows only in the direction of the wires and is negligible in other directions. This method is used to model a bundle of tiny wires tightly wound together but separated by an electrical insulator (Litz wires).

Then, the method to measure the electrical parameters of the coupler is based on the four-terminal-pair cabling technique through using E4990A impedance analyzer [140], as shown in Figure 2.3. It is an electronic equipment dedicated to measuring complex electrical impedance as a function of test frequency. The way to measure the mutual inductance based on this experiment is presented in Appendix B.

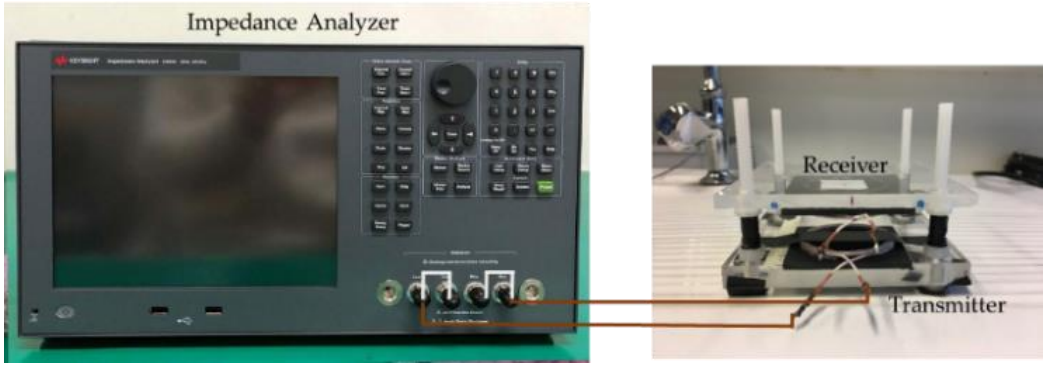

(a) Measurement of the self-inductance of the transmitter

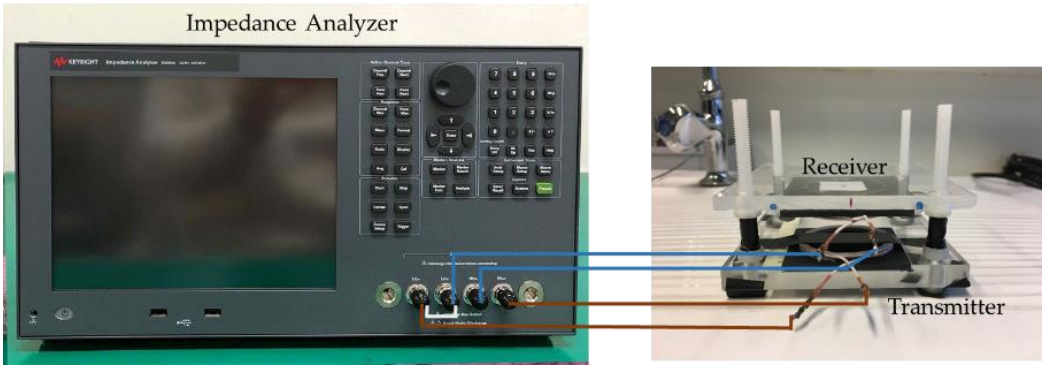

(b) Measurement of the mutual inductance between the transmitter and the receiver

Figure 2.3 Experiment to measure the electrical parameters of the coupler

2.3.1.2 Maximum transmission efficiency

In order to evaluate the agreement between the simulation and the measurement, Figure 2.4 shows the comparison of the mutual inductance M related to these two aspects with the normalized misalignment conditions. Due to their symmetry properties, the circular and square couplers have the same performance along the X and Y axis, so only one direction of the results is displayed.

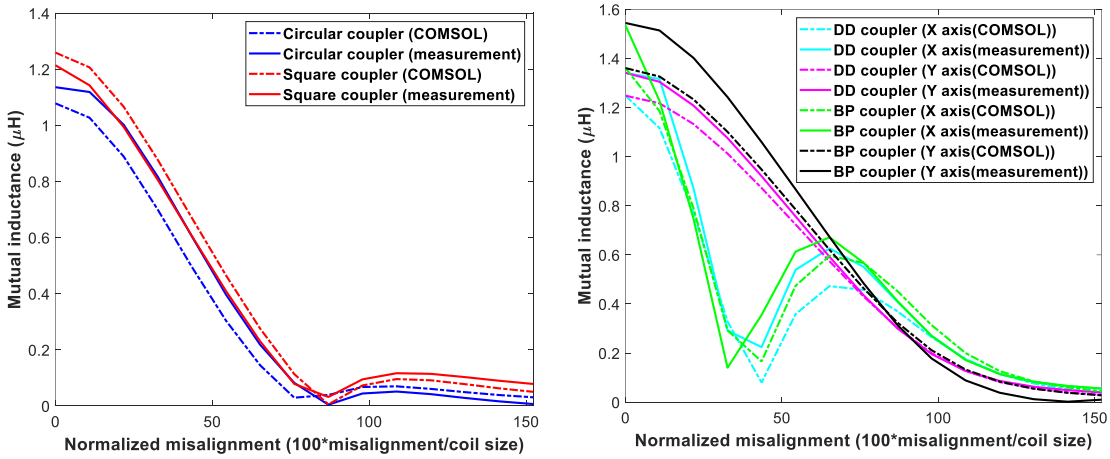

Figure 2.4 Mutual inductance M versus the misalignment

From Figure 2.4, there are some discrepancies between the simulation results and the measurement values for different couplers. A small part of these deviations is justified by measurement errors. However, the majority of the deviations are due to the fact that the coils of the coupler are made by hand, and it is hard to have the perfect shape as in the simulation. It can also be observed that the DD/BP couplers can provide more mutual inductance than circular/square couplers.

However, according to Equation (2-5), the maximum transmission efficiency η_{max} is not only connected to the mutual inductance between the transmitter and the receiver, but also connected to the conducting wire length. The conducting wire length is determined by the geometry size of

the coil and the number of turns in the coil. So, the relationship between the maximum transmission efficiency η_{max} and the normalized misalignment along the X/Y axis on the receiver (defined in Figure 2.2) can be calculated from experimental values of mutual inductances. Figure 2.5 shows the dependence of the maximum transmission efficiency η_{max} with the normalized misalignment along the X/Y axis. In order to better observe this figure, the part in the purple line framework is enlarged and shown in Fig 2.5 (b). The circular coupler has the maximum value of the maximum transmission efficiency compared to other couplers due to the smallest ratio between the conducting wire length and the mutual inductance. So it is preferred in a case where there is no misalignment between the transmitter and the receiver. On the other hand, with the misalignment increasing, the square coupler has a better tolerance than other couplers, especially DD/ BP couplers have a worse tolerance on the X axis (as defined in Figure 2.2).

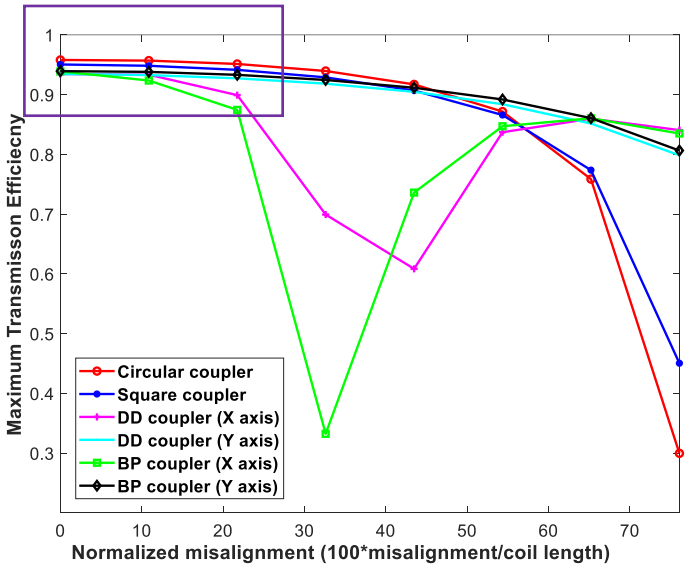

(a) Maximum transmission efficiency η_{max} versus the normalized misalignment

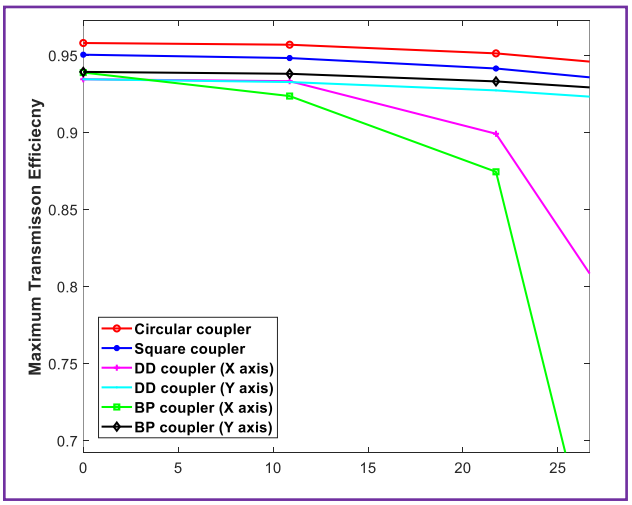

(b) Enlarged part from the purple line framework

Figure 2.5 Maximum transmission efficiency η_{max} versus the normalized misalignment

2.3.2 Magnetic flux density leakage evaluation

In addition to the transmission efficiency issues in the RIPT systems, the challenges in terms of electromagnetic radiation need to be addressed with particular consideration in order to control the risks related to electromagnetic compatibility (EMC) and human exposure [45]. Here, we will focus on the evaluation of the magnetic flux density leakage emitted by the couplers. A comparison of the four couplers in terms of magnetic radiation will be presented.

2.3.2.1 Near field test bench

The measurement of the magnetic flux density in the near field is carried out using the test bench in the GeePs laboratory. As shown in Figure 2.6, it includes:

- a 4-axis robot (3 translation axes and 1 rotational axis) allowing the magnetic probe to move above the measurement plane;
- a circular magnetic probe that performs field measurements using Faraday's law;
- a low-noise amplifier connected to the output of the probe to improve the sensitivity;
- a spectrum analyzer for displaying the power measured by the probe;
- a computer, connected to the spectrum analyzer, to collect the data from the spectrum analyzer, to control the robot and to create field cartography based on the position and energy.

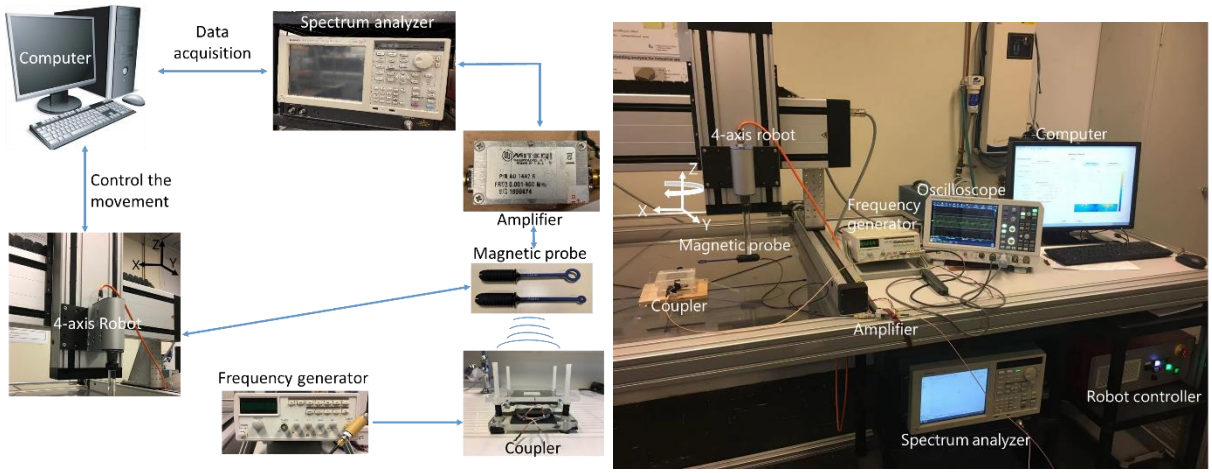

Figure 2.6 Near field test bench

The generator is used to supply the transmitter coil with a sinusoidal voltage at the defined frequency. The robot controls the position of the magnetic probe. The use of the probe is dedicated to capturing three components of the magnetic field (x, y, z) separately. A magnetic probe consists of a loop that generates a voltage, according to Faraday's law, once it intercepts a variable magnetic field. Figure 2.7 below shows the PBS H3/H2 magnetic probe from AARONIA [141]. PBS H3 with a diameter of 25 mm and PBS H2 with a diameter of 12 mm are used in the measurements of the magnetic field radiated by inductive power transfer systems. The magnetic field emitted by a coil and picked up by the probe generates a voltage that is amplified by a MITEQ AU-1442 type amplifier [142]. Its gain is 35 dB in the range from 1 kHz to 40 GHz for improving the quality of the measurements. The amplified signal is transmitted to the Tektronix

RSA5106A spectrum analyzer [143]. The latter is equipped with a General Purpose Interface Bus (GPIB) interface for communication with the computer, allowing the measured data to be processed.

Figure 2.7 Magnetic probe PBS H3/H2

The sensitivity of the magnetic probe is given in terms of a performance factor (PF) which is the ratio between the voltage V_m measured by the spectrum analyzer and the magnetic field H caught by the magnetic probe, as shown in Figure 2.8.

Figure 2.8 Measurement chain for the performance factor

The PF for magnetic field probes is given by Equation (2-6) [144]:

$$\mathrm{PF} = \frac{V_m}{H} \tag{2-6}$$

This value is independent of the radiating structure and the position of the probe above the radiation source, but depends on the characteristics of the probe, the amplifier which is connected between the probe and the spectrum analyzer, and the frequency. The detailed method of determining the PF is presented in Appendix C. When the frequency is 85 kHz, the performance factors for PBS H3 and PBS H2 are shown in Table 2.2:

Table 2.2 Performance factors for PBS H3 and PBS H2

	PBS H3	**PBS H2**
Performance factor ($dB_{mV/(A/m)}$)	-24	-40

2.3.2.2 Magnetic flux density leakage around the coupler

The SAE J2954 standard [40] defines three physical regions to facilitate EMF safety management of the RIPT system (Figure 2.9). Region 1 is the entire area underneath the vehicle, including and surrounding the wireless power assemblies, which shall not extend beyond lower body structure edges. Region 2 is the region outside the periphery of the vehicle. The boundary between Regions 1 and 2 extends downward from the lower periphery of the vehicle body sides. When the vehicle is not covering the transmitter, Region 2 includes the entire area over and

around the transmitter. Region 3 is the vehicle interior. It is obvious that Region 2 and 3 must adhere to the EMF safety management principles.

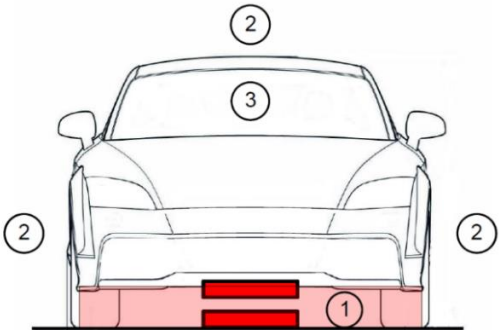

Figure 2.9 SAE J2954 EMF regions in an EV with the RIPT system [40]

So, considering the restrictions on field exposure, it is necessary to estimate the magnetic flux density leakage: above the coupler and at the side of the coupler.

2.3.2.2.1 Magnetic flux density leakage above the receiver

The measurement leads to a map of the magnetic flux density leakage over the receiver. This mapping is done on a measurement plane at a defined height: 32 mm above the receiver in Figure 2.10. This definition of the measurement plane is used for these four shapes of coupler (defined in Figure 2.3).

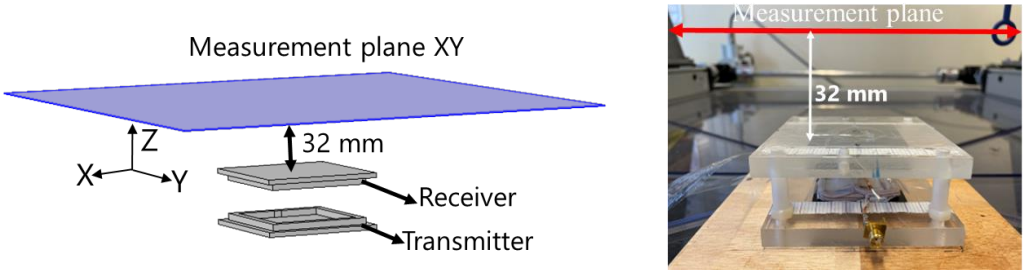

Figure 2.10 Measurement plane XY of the magnetic flux density leakage above the receiver

Table 2.3 illustrates the measurement conditions for the measurement plane in Figure 2.10.

Table 2.3 Measurement conditions for the magnetic field distribution

Parameter	Value [unit]
Measurement step along the X axis	10 [mm]
Measurement step along the Y axis	10 [mm]
Measured plane	400mm×400mm
Height from the receiver with the ferrite plate	32 mm
Number of the measurement points	1681 (41×41)
Measurement frequency	85 kHz
Peak current fed by the generator	210 [mA]

The amplitude of the current provided by the generator, which is measured by a current probe, is used as the excitation value of the transmitter coil in 3D simulations performed with COMSOL. A comparison of the magnetic flux density distribution obtained by the measurement and simulation is carried out under the same conditions (geometry, measurement plane, excitation current, etc.) in the form of three components ($|B_x|, |B_y|, |B_z|$) and norm B_{norm}.

Table 2.4 shows the amplitude distributions of the three magnetic flux density component B_x, B_y, B_z (the orientation of the X, Y, and Z axis is given in Figure 2.6) and the norm B_{norm} on the small-scale square coupler.

Table 2.4 Distribution of the magnetic flux density in the simulation and measurement

$\|B_x\|$	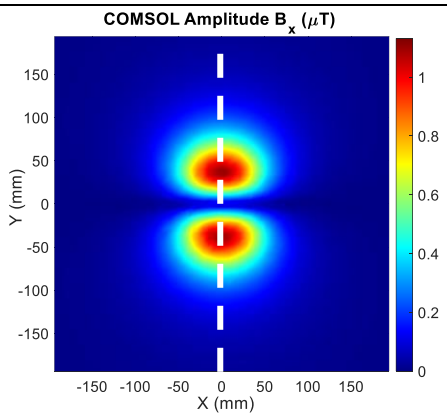	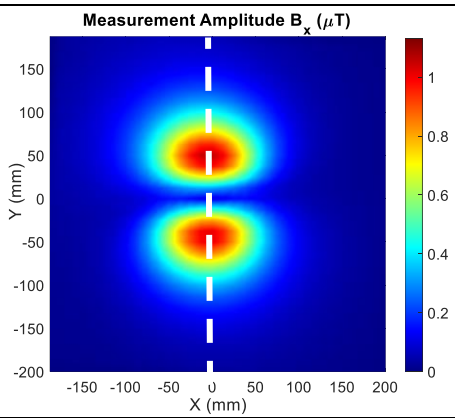
$\|B_y\|$	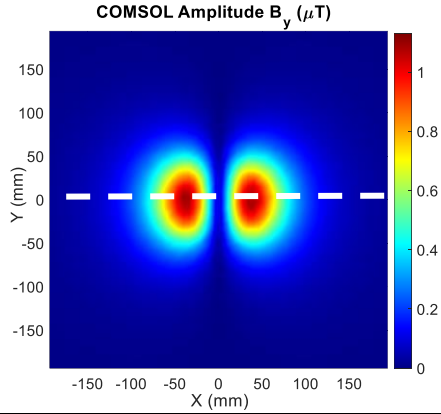	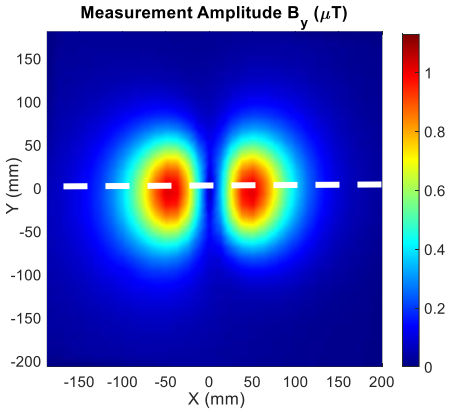
$\|B_z\|$	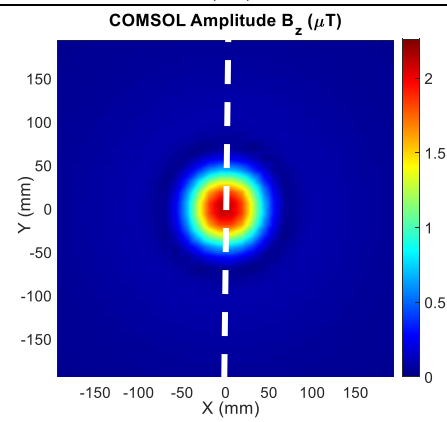	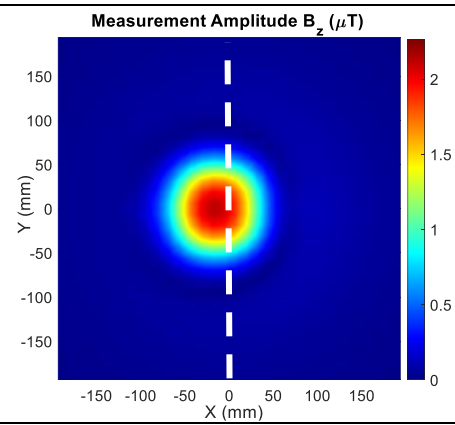

$\|B_{norm}\|$	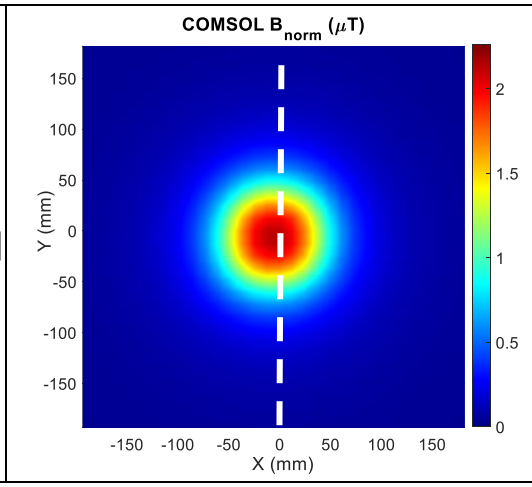	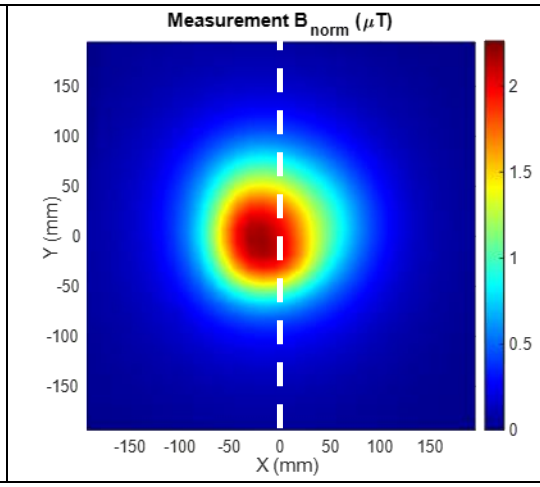

It can be seen that there is a good agreement in the magnetic flux density distribution between the measurement results and the simulations. To better compare the values of the flux density for each component, Figure 2.11 represents a comparison of the magnetic flux density amplitudes (measurements and simulations) on the lines indicated in white dotted in Table 2.4.

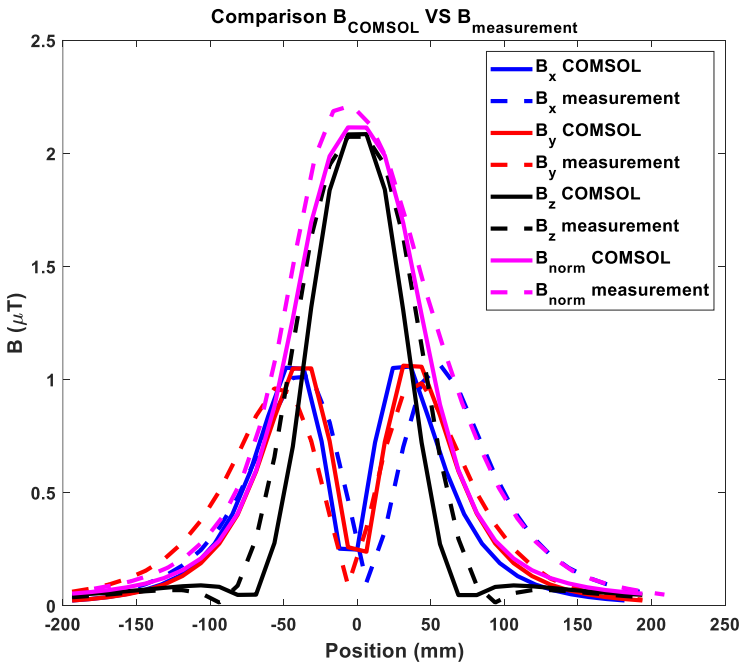

Figure 2.11 Comparison of amplitudes of the magnetic flux density obtained by simulation and by measurement

Looking at Figure 2.11 for the magnetic flux density, there is a difference in some zones. This situation may be due to the differences between the real measurement conditions and those of the simulation (height of the measurement plane, variation of the emitted current supplied by the generator, the angle between the probe and the component, etc.), in addition to the fact that the coils used in the experiment were made by hand, and were not in the same shape as in the simulation. However, this step validates the results from the simulation and the measurement.

Then, the steps above are repeated on the circular, DD, and BP couplers. In order to better compare the magnetic flux density leakage from these different shapes of couplers, only the amplitudes and the distributions of the normal magnetic flux density are summarized in Table 2.5.

To quantify these results between the simulations and the measurements, the FSV (Feature Selective Validation) tool is used [144-146]. This tool was designed as a technique to quantitatively compare a set of data. The application of the FSV tool for data validation is a key element of the current IEEE standard being developed to describe the quality of the results of an electromagnetic simulation. FSV tool is based on two analyses: the first one analyses the Amplitude Difference Measure (ADM), while the other one analyses the Feature Difference Measure (FDM). The range of values for ADM and FDM is divided into six categories (Excellent (Ex), Very good (VG), Good (G), Fair (F), Poor (P), Very poor (VP)) [145].

The results of these FSV comparisons for different couplers are also included in Table 2.5.

Table 2.5 Distribution of the magnetic flux density in the simulation and measurement for different shapes of couplers

Square coupler: Magnetic flux density B_{norm} above the receiver 32 mm	
Simulation result	Measurement result
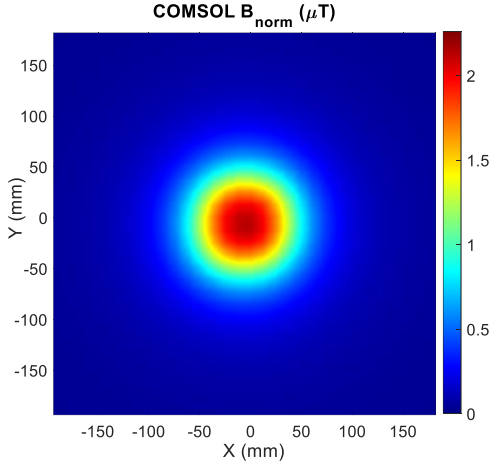	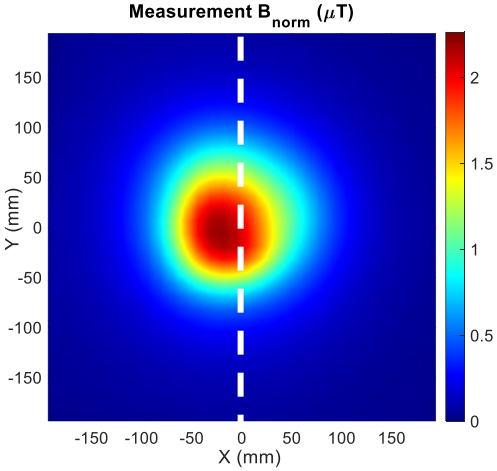
Square coupler: FSV anaysis results	
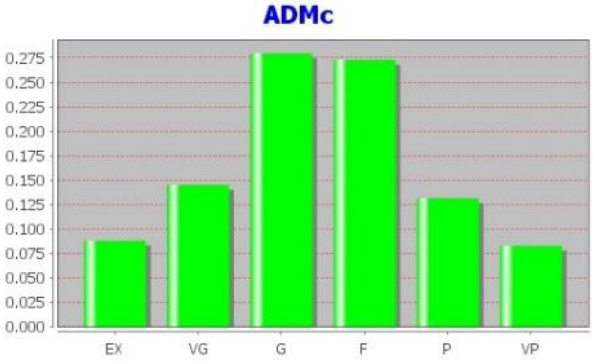	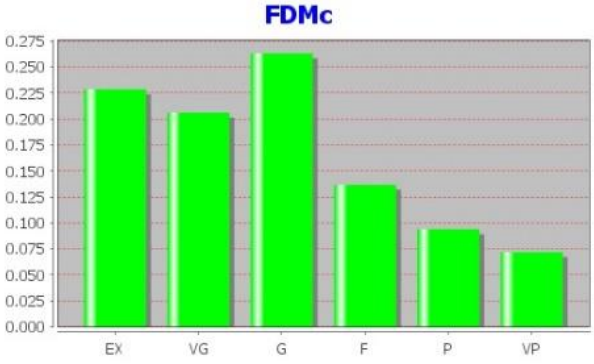

(a)

Circular coupler: Magnetic flux density B_{norm} above the receiver 32 mm	
Simulation result	Measurement result
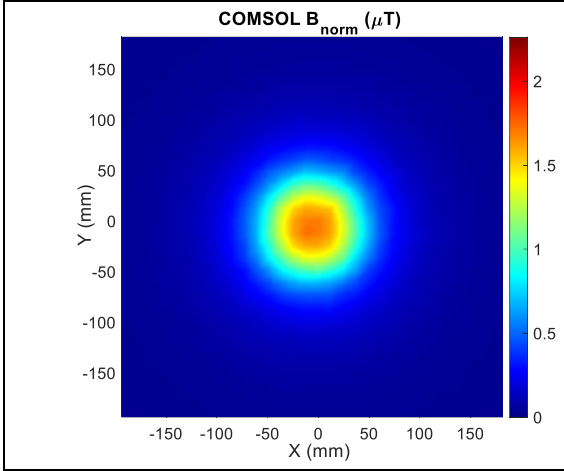	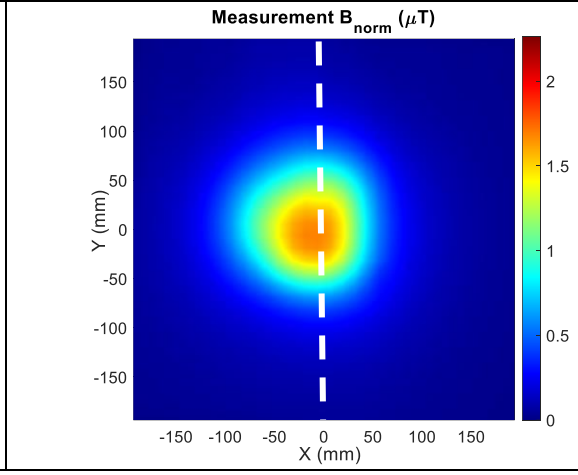
Circular coupler: FSV analysis results	
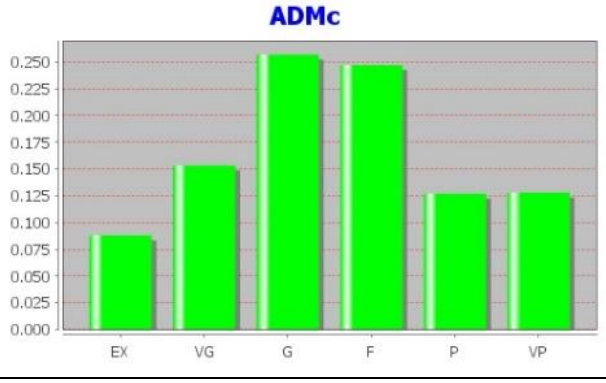	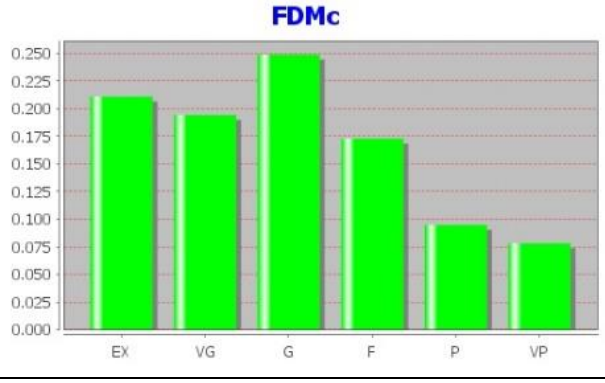

(b)

DD coupler: Magnetic flux density B_{norm} above the receiver 32 mm	
Simulation result	Measurement result
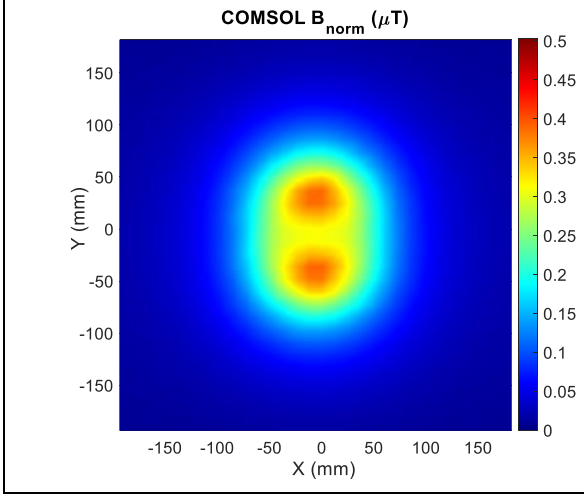	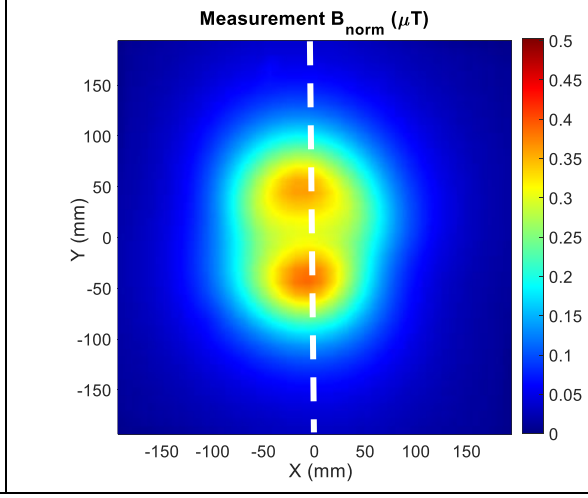

DD coupler: FSV anaysis results

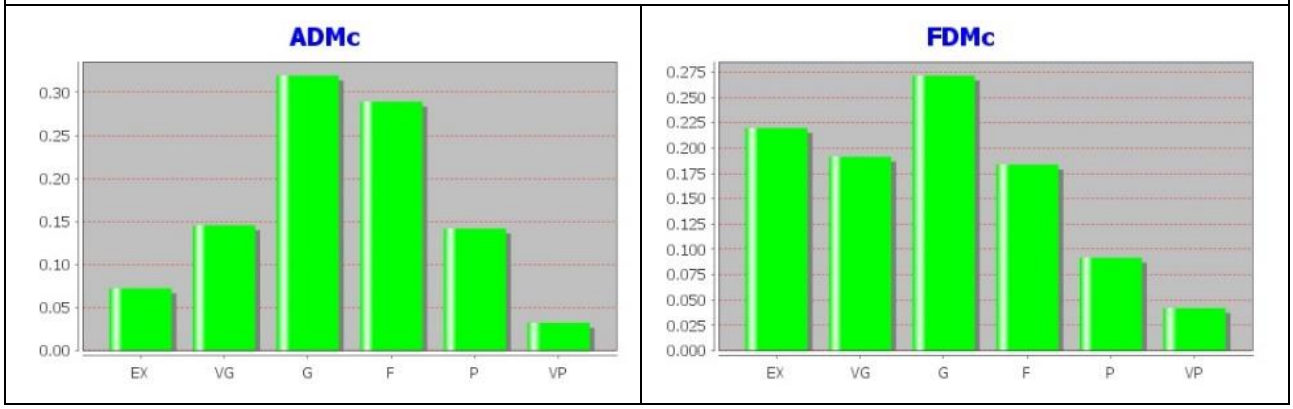

(c)

BP coupler: Magnetic flux density B_{norm} above the receiver 32 mm

Simulation result | Measurement result

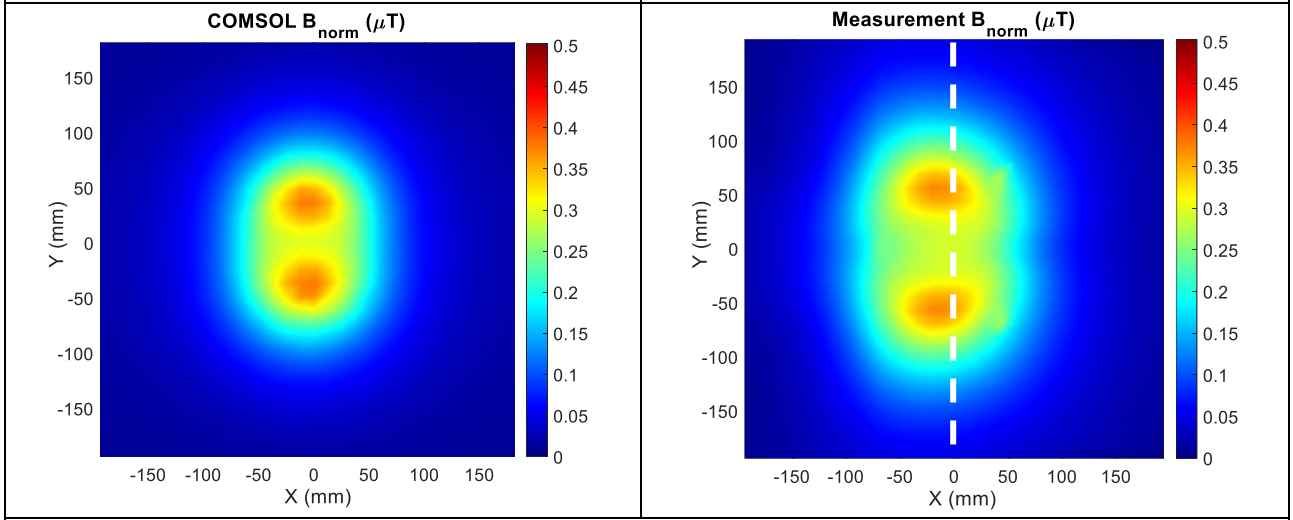

BP coupler: FSV anaysis results

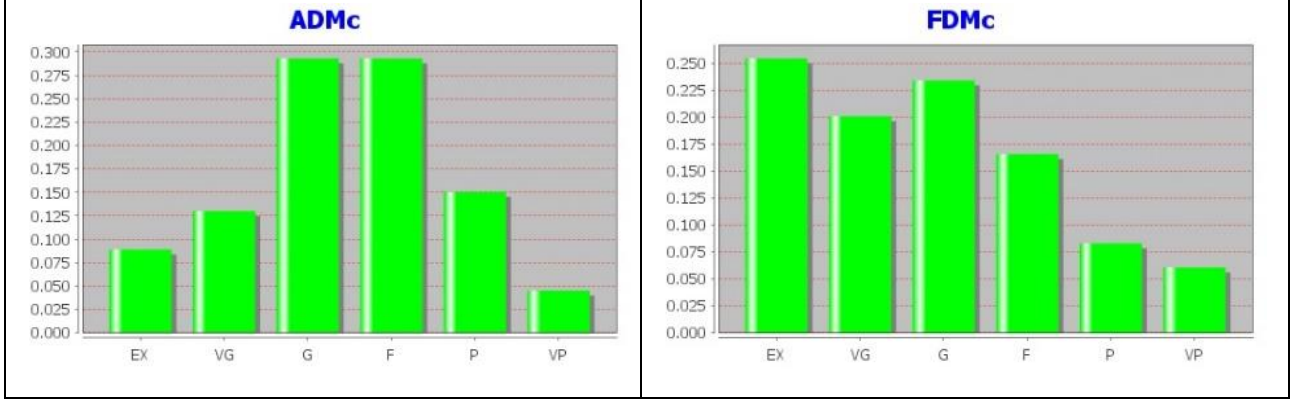

(d)

These results are mostly in the range of excellent to fair, showing a good agreement between the measurements and the simulations.

To better compare magnetic flux density leakage above different couplers, Figure 2.12 represents the measured B_{norm} on the lines indicated in white dotted in Table 2.5. It can be seen that the square coupler has the maximum magnetic leakage compared to other couplers. Moreover, DD/BP couplers have the same magnetic leakage above the receiver.

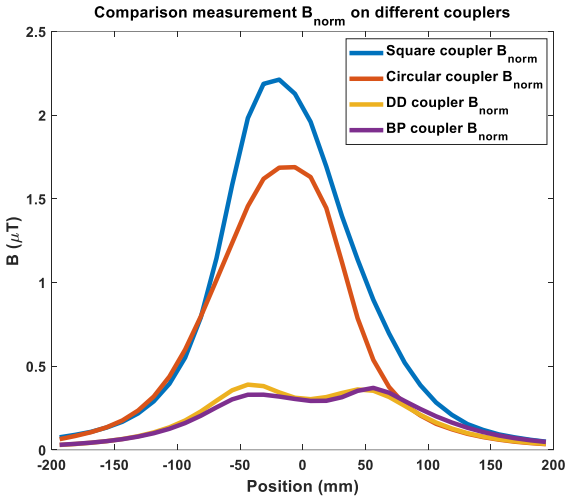

Figure 2.12 Comparison of amplitudes of the magnetic flux density B_{norm} obtained by measurement

2.3.2.2.2 Magnetic flux density leakage at the side of the coupler

When observing the magnetic flux density leakage at the side of the coupler, it is meaningful to study which side should be chosen. For square and circular couplers, they have the same performance on these four sides due to their structure. But for DD/BP coupler, the side parallel to the y axis (shown in Figure 2.2) is chosen to study due to its more magnetic flux density leakage.

In Figure 2.13, the measurement plane of the magnetic field distribution is at 70 mm far from the center of the coupler. The measurement conditions for the measurement plane are the same as shown in Table 2.3.

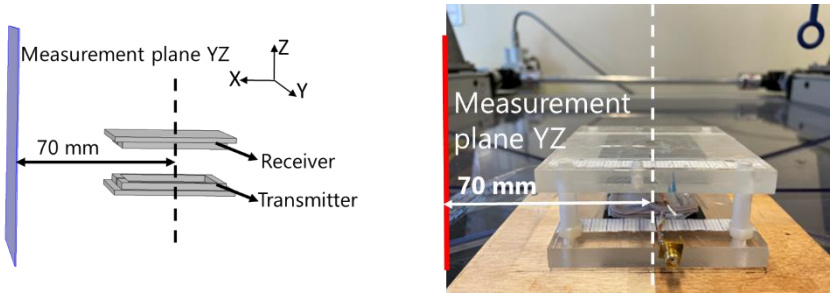

Figure 2.13 Measurement plane YZ of the magnetic flux density leakage at the side of the coupler

Table 2.6 summarizes the norm of magnetic flux density $\vec{B}$ (B_{norm}) on the plane as defined in Figure 2.13 for the four shapes of couplers. The results of FSV comparisons for different couplers are also included in Table 2.6. They are mostly in the range of excellent to fair, showing a good agreement between the measurements and the simulations for the magnetic flux density distribution at the side of the coupler.

Table 2.6 Distribution of the magnetic flux density in the simulation and measurement for different shapes of couplers

<table>
<tr><td colspan="2">Square coupler: Magnetic flux density B_{norm} 70 mm far from the center of the coupler</td></tr>
<tr><td>Simulation result</td><td>Measurement result</td></tr>
<tr><td> 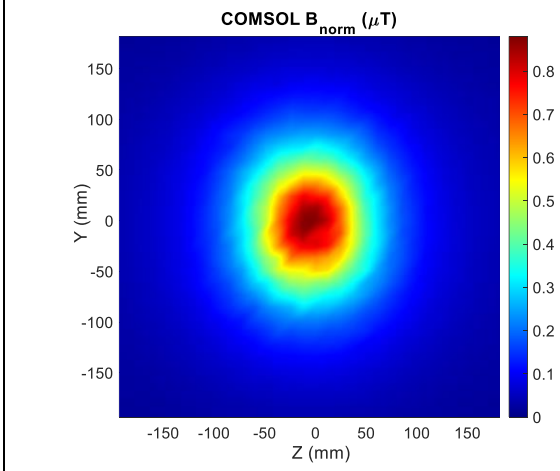
</td><td> 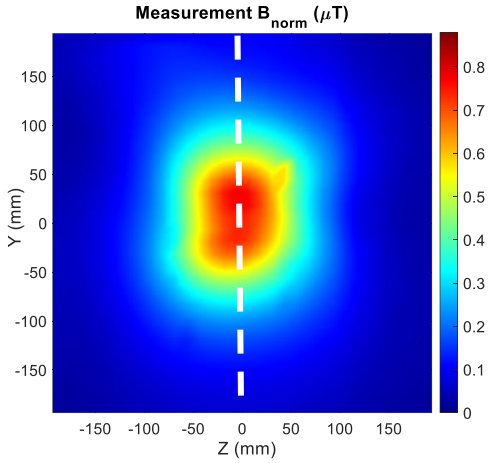
</td></tr>
<tr><td colspan="2">Square coupler: FSV anaysis results</td></tr>
<tr><td> 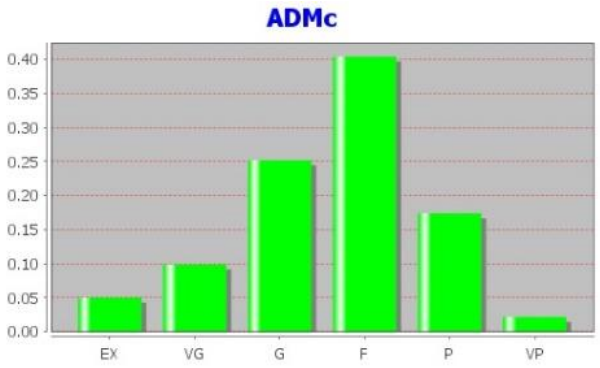
</td><td> 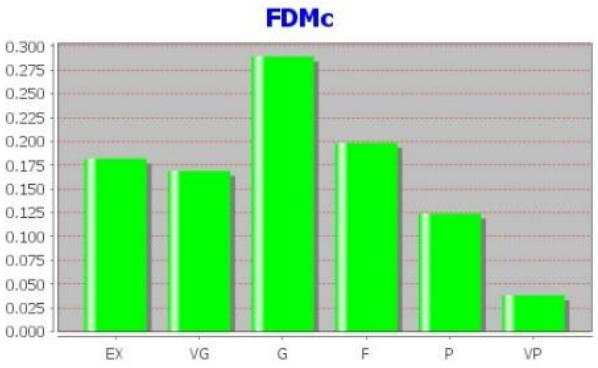
</td></tr>
</table>

(a)

Circular coupler: Magnetic flux density B_{norm} 70 mm far from the center of the coupler	
Simulation result	Measurement result
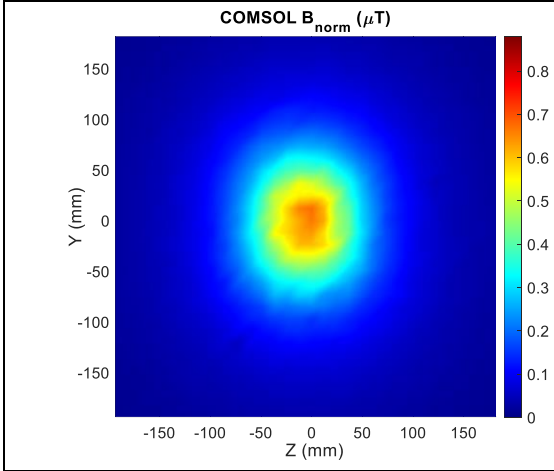	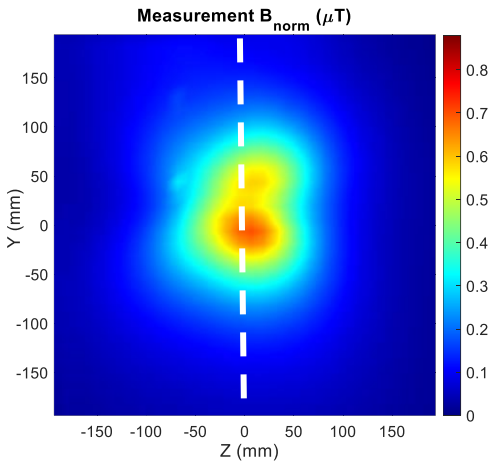
Circular coupler: FSV anaysis results	
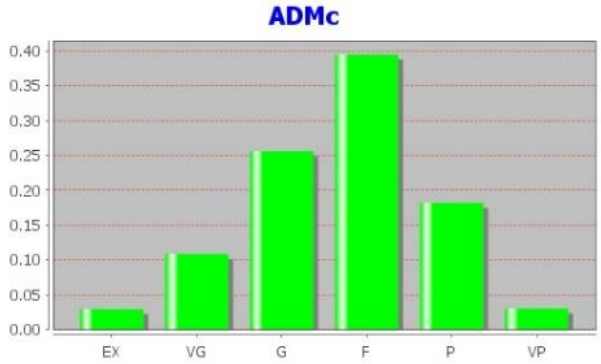	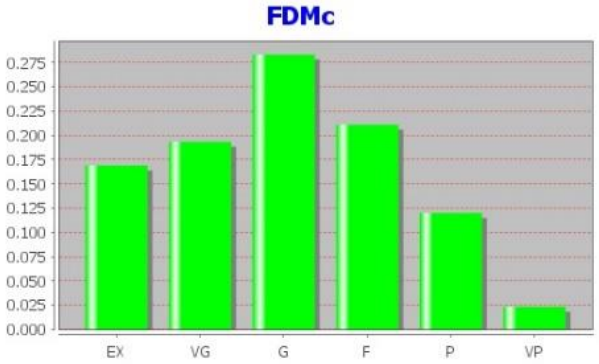

(b)

DD coupler: Magnetic flux density B_{norm} 70 mm far from the center of the coupler	
Simulation result	Measurement result
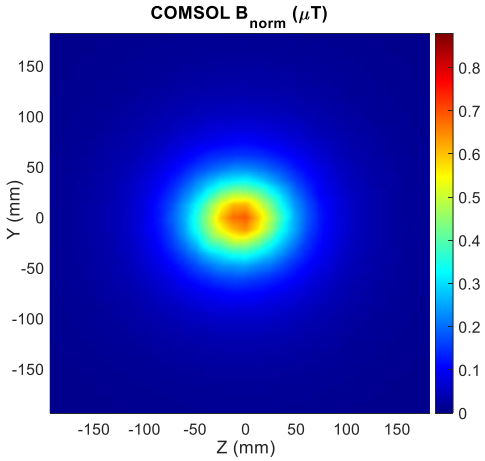	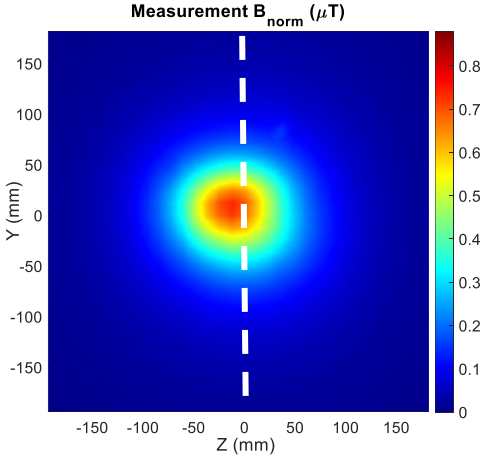

DD coupler: FSV anaysis results

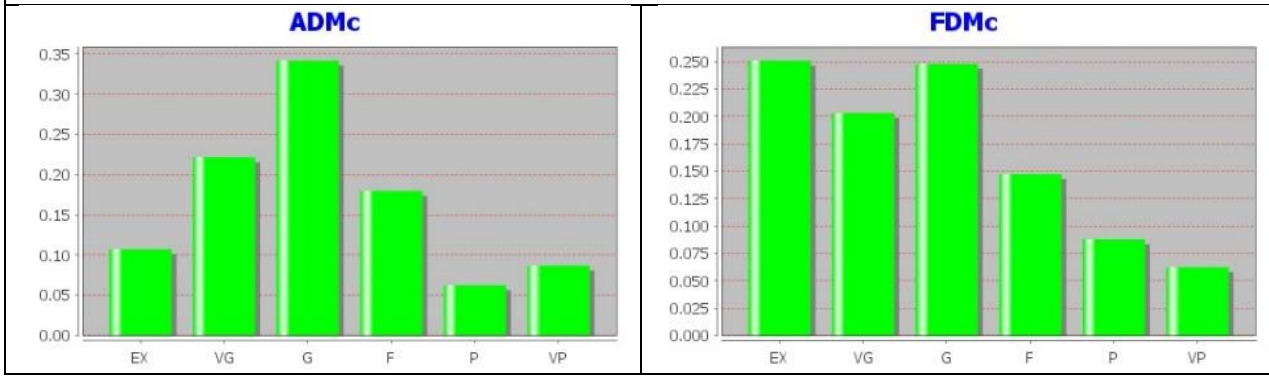

(c)

BP coupler: Magnetic flux density B_{norm} 70 mm far from the centre of the coupler

Simulation result	Measurement result

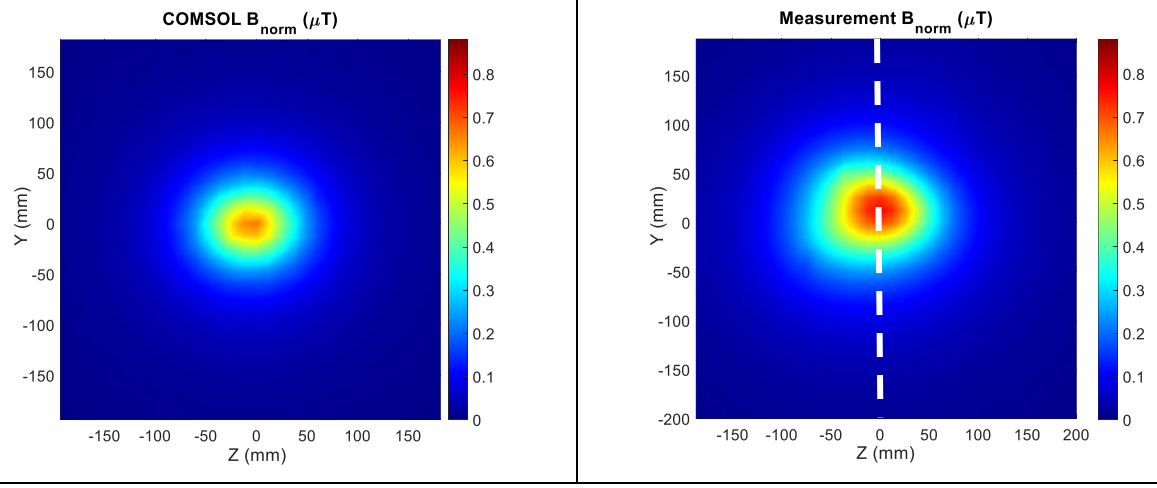

BP coupler: FSV analysis results

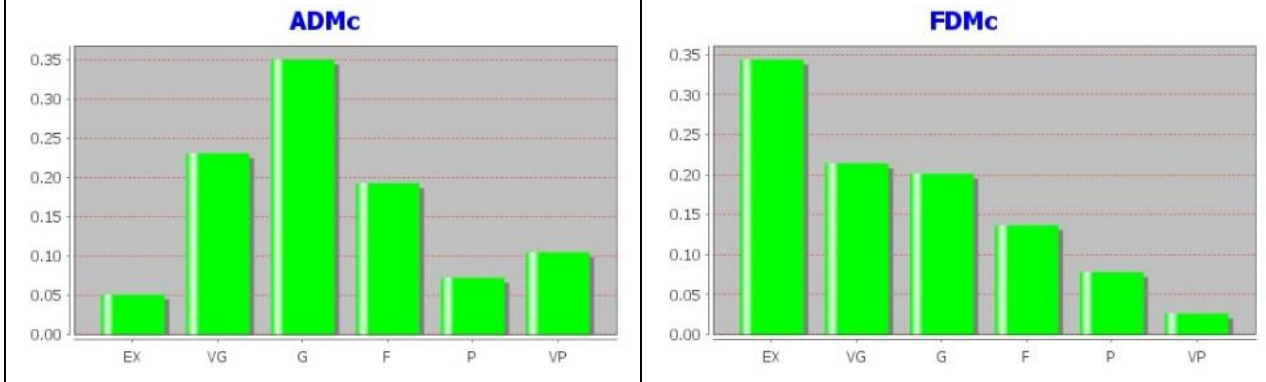

(d)

To better compare the magnetic flux density leakage at the side of these different shapes of couplers, Figure 2.14 represents the measured B_{norm} on the lines indicated in white dotted along Y axis in Table 2.6. All of the couplers lead to nearly the same amplitude of magnetic flux density at the side.

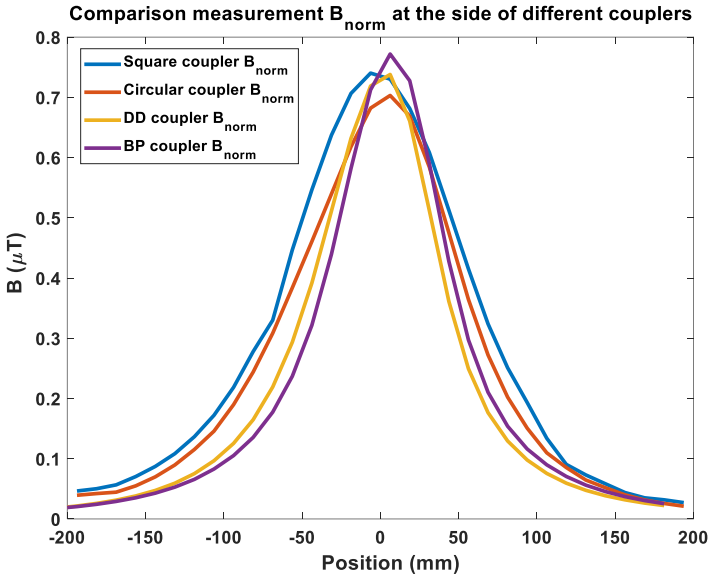

Figure 2.14 Comparison of amplitudes for the magnetic flux density B_m obtained by measurement

2.3.3 Discussion

Four shapes of small-scale couplers (circular, square, DD, and BP) are verified and compared on these two aspects: maximum transmission efficiency and magnetic flux density leakage between the simulation and the experiment. The circular shape can be preferred and used in a case where the relative positioning of the transmitter and receiver is ideal (in the aligned position). On the other hand, the square shape is well suited to dynamic charging systems for its tolerance to the misalignment between the transmitter and the receiver, but this shape provides a higher amplitude of magnetic flux density above the receiver.

2.4 Real-scale square coupler analysis

According to the analysis of the couplers above, the square is chosen as the coil shape due to its better tolerance to the misalignment between the transmitter and the receiver. So, a real-scale square coupler is studied between the simulation and the experiment. The real-scale square coupler is shown in Figure 2.15, and the parameters are summarized in Table 2.7. Here, the square coupler has six turns arranged in two layers. These turns are made with Litz wires composed of 1250 strands, and the diameter of the strand is chosen to be 0.1 mm so that it is smaller than the skin depth at the operating frequency [80, 147].

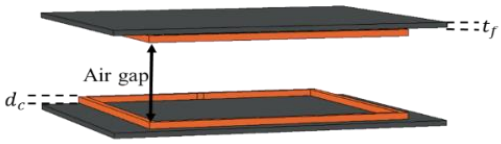

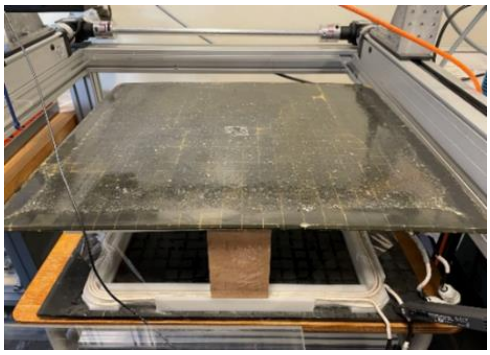

(a) Real-scale square coupler

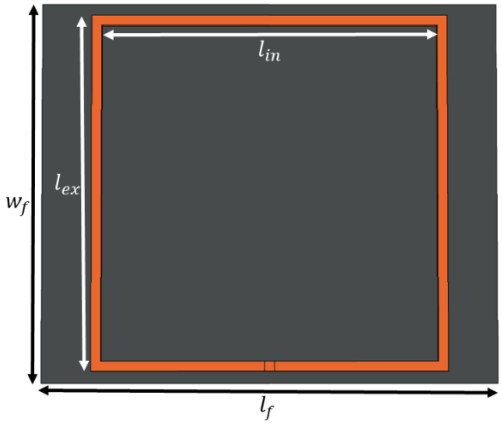

(b) Size of the real-scale square coupler

Figure 2.15 Real-scale square coupler

Table 2.7 Parameters of the real-scale square coupler

Parameter	**Value [Unit]**
Exterior length of the coils l_{ex}	468 $[mm]$
Interior length of the coils l_{in}	442 $[mm]$
Coil thickness d_c	13 $[mm]$
Ferrite length l_f	600 $[mm]$
Ferrite width w_f	500 $[mm]$
Ferrite thickness t_f	2 $[mm]$
Ferrite type [148]	TDK N27
Relative permeability of ferrite	2500
Cross-sectional area of the wires S	9.82 $[mm^2]$
Air gap	150 $[mm]$

According to the method mentioned in Section 2.3.1, the electrical parameters of the real-scale square coupler are simulated and measured. The results are given in Table 2.8. The relative errors between the measurement and the simulation are around 10%, which may be caused by the real coil shape that is not the same as defined in the simulation or the real coil winding not being well positioned in two layers.

Table 2.8 Comparison of the electrical parameters in the simulation and the measurement

Frequency =85 [kHz]	**Self-inductance [μH]**	**Mutual inductance [μH]**	**Coupling coefficient**
Simulation	63.7	13.4	0.21
Measurement	58.5	12.1	0.20
Relative error of the experiment (%)	8.1%	9.7%	4.8%

After, the measurement plane of the magnetic flux density leakage distribution is 150 mm above the receiver in Figure 2.16.

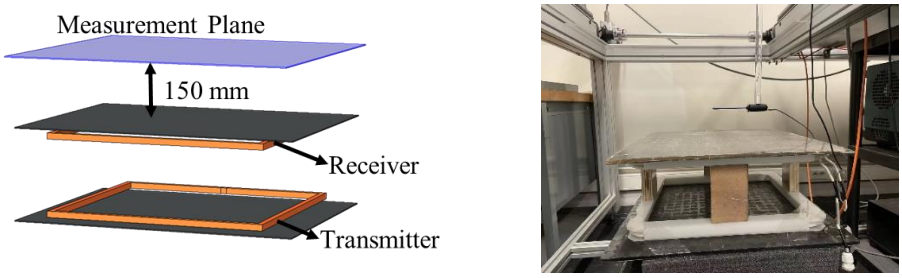

Figure 2.16 Measurement plane of the magnetic flux density leakage above the receiver

Here, the magnetic flux density above the receiver is measured by the same near-field test bench in Figure 2.17.

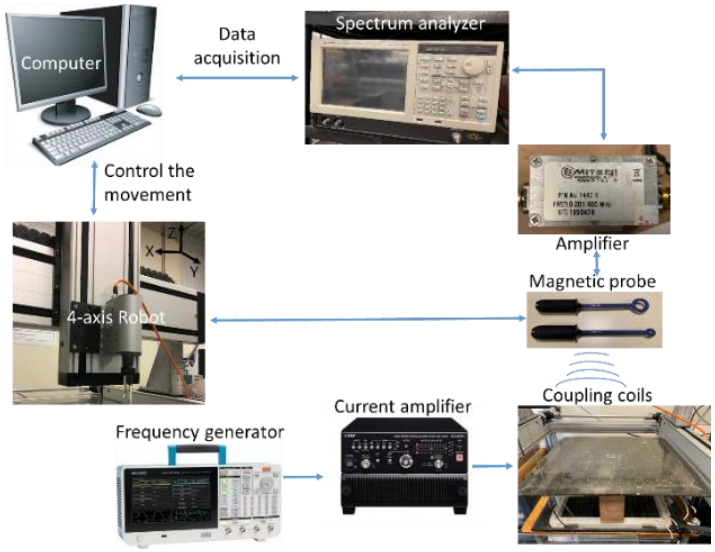

Figure 2.17 Magnetic flux density leakage measurement for real-scale square coupler

The amplitude of the current inside the transmitter is enlarged by the HSA42011 power amplifier [149] for better measurement in the real-scale square coupler. The current in the transmitter is measured by the current probe, and then this value works as the excitation current for the transmitter coil in the 3D FEM simulation performed with COMSOL.

The measurement conditions for the measurement plane are the same as shown in Table 2.9. The size of the measurement plane is limited by the ranges along the X and Y axis in the test bench, so the complete magnetic flux density distribution needs to be obtained by flipping and symmetry the measured result obtained from the test bench (shown in Figure 2.17).

Table 2.9 Measurement settings for the magnetic field distribution

Parameter	**Value [unit]**
Measurement step along X axis	10 [mm]
Measurement step along Y axis	10 [mm]
Measurement plane	370mm×370mm
Height from the receiver with the ferrite plate	150 mm
Number of the measurement points	1369 (37×37)
Measurement frequency	85 kHz
Peak current value in the transmitter	1.03 [A]

In Table 2.10, a comparison of the norm of magnetic flux density distribution between the measurement and simulation is carried out under the same conditions (geometry, the measurement plane, excitation current, etc.). The FSV analysis results are mostly in the range of excellent to good, showing a very good agreement between the measurement and the simulation for the magnetic flux density distribution above the real scale square coupler.

Table 2.10 Measurement results for real-scale square coupler

Real scale square coupler: Above the receiver 150 mm	
Simulation	Measurement
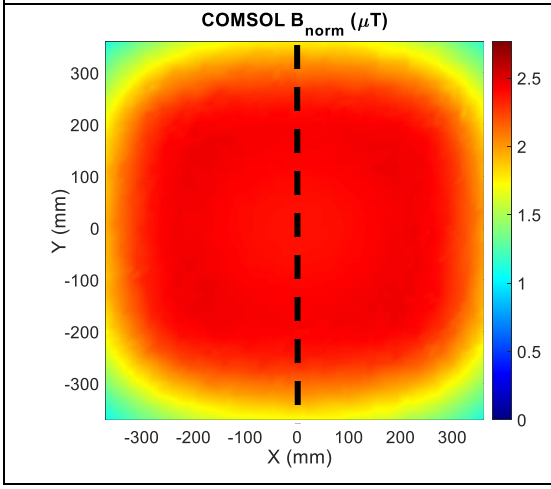	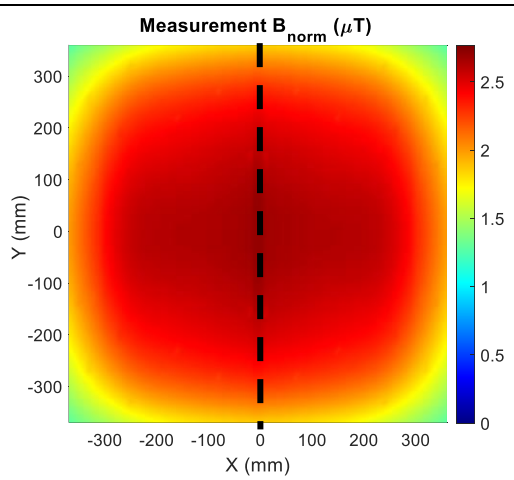

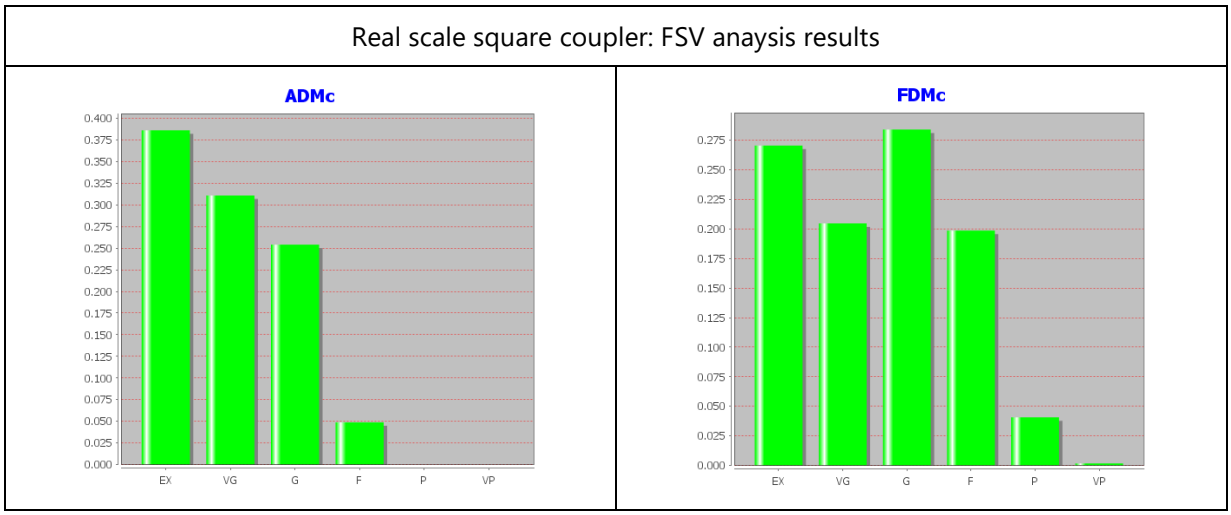

Figure 2.18 presents the comparison of the measured and simulated B_{norm} on the lines indicated in black dotted in Table 2.10. There exist some differences in the position and the amplitude of the magnetic flux density leakage, maybe due to the fact that the coils of the coupler are made by hand, and they are not as same as those defined in the simulation. Moreover, the ferrite plate in the experiment is not as flat as in the simulation. This leads to the phenomenon that the magnetic flux density leakage values in the center of the measurement are not the same as those values in the simulation.

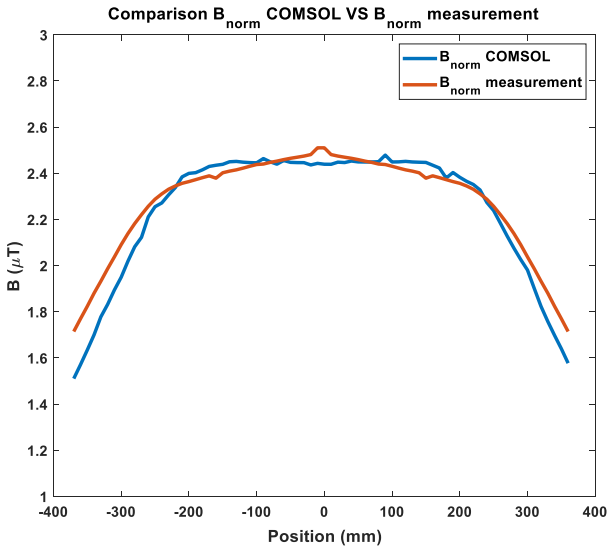

Figure 2.18 Comparison of the magnetic flux density B_{norm} obtained by simulation and measurement

Then, it is meaningful to make the quantitative comparison between the real scale and small-scale coils (which is ten times smaller than the real scale) on the electrical parameters and magnetic parameters. In Table 2.11, it can be found that the ratio of the self-inductances and the

mutual inductances is round 10, which is related to the analytical expression of the inductance [150], and the coupling coefficient ratio is close to 1.

Table 2.11 Electrical parameters comparison between the real-scale of coils and small-scale coils

Comsol simulation	**Self-inductance L (μH)**	**Mutual inductance M (μH)**	**Coupling Coefficient**
Real-scale square coupler	63.69	13.40	0.21
Small-scale square coupler	5.66	1.33	0.23
Ratio between real-scale and small-scale	11.25	10.07	0.91

Then, the magnetic flux density leakage distributions are taken into account from the plane above the receiver and the plane at the side of the coupler.

Table 2.12 Magnetic parameters comparison between the real-scale of coils and small-scale coils

Real-scale square coupler	Small-scale square coupler
Above the receiver 150 mm	Above the receiver 15 mm
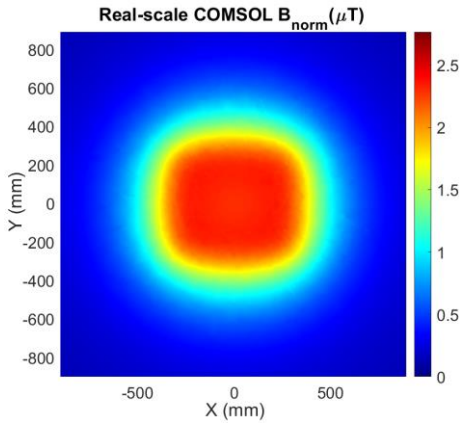	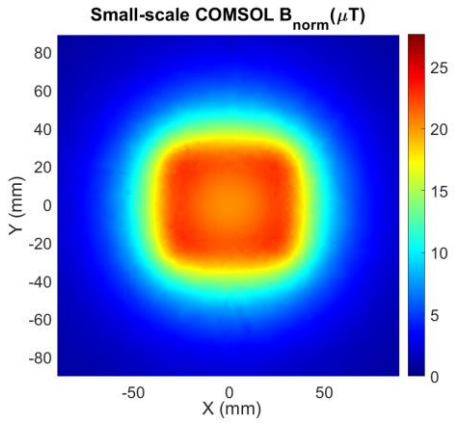
700 mm at the side of the coupler	70 mm at the side of the coupler
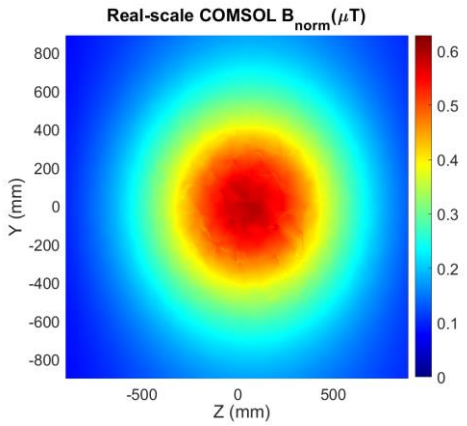	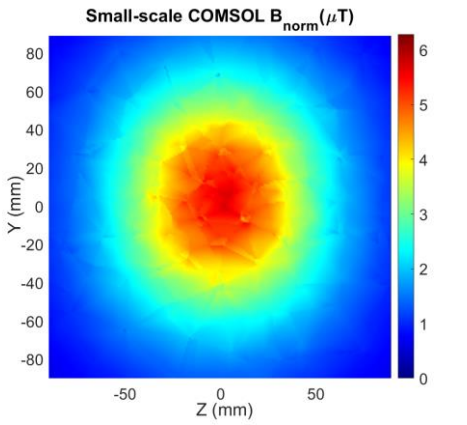

When the current provided in the transmitter is the same, equal to 1.03 A, the small-scale coils can provide around ten times higher magnetic flux density than the real-scale coils, which is deduced from the analytical formula of the magnetic field created by a single loop [151], and the magnetic flux density distribution shape is the same between the real scale square coupler and the small scale square coupler, independent of the size of the coupler.

2.5 Conclusion

In this chapter, studies based on four shapes of couplers for a RIPT system dedicated to EVs are presented.

Section 2.2 analyses how the ratio between the wire length and the mutual inductance influences the maximum transmission efficiency when the transmitter and the receiver are identical, and the frequency is defined. If the wire length is fixed, the mutual inductance will have the most effect on the transmission efficiency.

Section 2.3 makes a comparison of different shapes of couplers using the COMSOL simulation tool and the experimental results on 1:10 scale prototypes developed in the laboratory. Four coupler shapes from the bibliography were selected, and their comparisons were carried out considering the maximum transmission efficiency and the magnetic flux density leakage. For maximum transmission efficiency in RIPT systems, the circular coupler can provide the maximum values among these couplers, but the square coupler has a higher tolerance to misalignment than others; meanwhile, the square coupler has more magnetic flux density leakage above the receiver. However, the square coupler is chosen instead of circular one as it is easier to manufacture and is more suitable in the case of dynamic RIPT system.

Section 2.4 presents the simulation and the measurement on the real-scale square coupler. It can be seen that there is a very good agreement between the simulation and the measurement. At the same time, the quantitative relationship between the real-scale and small-scale can be found in the electrical parameters and the magnetic flux density of the square coupler.

Although the comparison of the coupling coefficient for the four shapes of couplers has been studied previously in [80], the dependence of the variation of maximum transmission efficiency with the misalignment is evaluated for the first time in this work, and the magnetic flux density distribution around the coupler is also carried out for the RIPT system. It gives a complete distribution area compared to one or several measurement points of the magnetic flux density in the literature.

However, when the sources of uncertainty (the misalignment along the X or Y axis, the variation in air gap, or the rotation on the receiver) concurs, how the maximum transmission

efficiency varies is unknown. According to the analysis carried out in this chapter, the maximum transmission efficiency is only related to the mutual inductance when the coils and the frequency are predefined. So, it can be a meaningful study of how these uncertainties influence the mutual inductance M.

Furthermore, the reliability of the 3D coupler model has been confirmed through the comparison between the simulated values and the experimental values in the mutual inductance and the magnetic flux density leakage. But a parametric sweep for all these uncertainty parameters is very time-consuming. So, it is substantial to conduct a metamodel procedure by using the COMSOl simulation results, which can help save computational time. In the following chapter, we will see a detailed study of the metamodels of the mutual inductance M for these four couplers taking into account sources of uncertainty.

CHAPTER 3 ANALYSIS OF RIPT SYSTEMS BY METAMODELING

3.1 Introduction

In a real scenario involving RIPT systems, various positions of the receiver may happen during the park (static RIPT) or driving (dynamic RIPT) [30]. A careful design process of RIPT systems requires taking into account multiple parameters (misalignment, relative rotation of the receiver, air gap, etc.). So, multiple 3D FEM computations are needed to assess the performance of the RIPT system when these situations happen. Nevertheless, the use of complex simulation tools leads to high computational costs in case of wide parametric analysis. In this case, a standard Monte Carlo (MC) analysis becomes challenging in terms of computer resources and simulation time [152-153].

In order to solve this problem, the "metamodeling techniques" for the parametric and statistical analysis in complex nonlinear problems have been developed. They can reduce the computational cost by substituting an expensive computational model with a metamodel, an unphysical analytical approximation of the original model that is much faster to evaluate [116, 152, 154]. The metamodels are constructed by learning the approximation from a set of input parameters and their corresponding model responses, for example, generated from running 3D FEM computations. Because it is faster to evaluate, a metamodel can allow more sophisticated analyses, such as sensitivity analysis [115, 121, 155]. However, they also have some limitations, such as how to choose samples effectively and define internal parameters for the metamodeling techniques.

Several metamodeling techniques have been applied to generate several metamodels trained with a limited set of simulation results, such as Support Vector Regression (SVR) [113], Multigene Genetic Programming Algorithm (MGPA) [114], Polynomial Chaos Expansions (PCE) [115], and so on. Reference [154] focuses on the application of the SVR with polynomial kernels to the uncertainty quantification and the parametric modeling of structures. Then, references [116, 154] provide a comparison in terms of accuracy and robustness to noise among the SVR, the least squares SVR [156], and the sparse PCE. In [117-119], a MPGA metamodel is investigated to express the self-inductance and the mutual inductance of the RIPT system versus geometrical parameters of the ferrite and coils, so new equations are proposed for evaluating these values of the inductances.

The goal of this chapter is to choose a metamodeling technique for analyzing the mutual inductance of RIPT systems taking into account the sources of uncertainty (misalignment along the X/Y axis, the variation in air gap, and the rotation on the receiver). First, we present a comparison among the SVR with the Gaussian radial base function (RBF) kernel, MGPA, and PCE metamodels for analyzing the mutual inductance of small-scale square couplers, taking into account the sources of uncertainty. Here, the square couplers are chosen first because they can be used in the static RIPT or dynamic RIPT systems [3-5], and they have a better tolerance to misalignment than circular, DD, and BP couplers. These metamodels are built based on the samples obtained from the 3D-FEM numerical tool-COMSOL [132]. And a sensitivity analysis is also performed to discuss how the sources of uncertainty influence the mutual inductances and the maximum transmission efficiencies of small-scale couplers (circular, square, DD, and BP).

3.2 Metamodeling techniques Introduction

This section provides an overview of the mathematical framework behind these metamodeling techniques:

- Support Vector Regression (SVR) with RBF kernel;
- Multigene Genetic Programming Algorithm (MGPA);
- Sparse Polynomial Chaos Expansions (sparse PCE).

They are considered promising techniques which allow building metamodels for the nonlinear system responses with several variables [116-118, 154].

3.2.1 Support vector regression metamodeling

Support vector regression is a metamodeling technique that can be used to approximate an unknown or expensive-to-evaluate model. It represents a class of learning techniques for regression tasks developed by Vapnik [157]. This method provides it with significant generalization capabilities, thus making them less likely to overfit data.

SVR attempts to approximate the relationship between the input variables $\boldsymbol{x} = [x_1, \cdots, x_d] \in \mathbb{R}^d$ and the output $y \in \mathbb{R}$ given a training data set of N samples $\{(\boldsymbol{x}_i, y_i)\}_{i=1}^N$ ($y = M(\boldsymbol{x})$ is the model response of the system supposed to be a scalar quantity with a finite variance, where M is a numerical model presenting the observed phenomenon). It achieves this through the equation [113, 116]:

$$\mathcal{M}^{SVR}(\boldsymbol{x}) = \boldsymbol{w}^T \Phi(\boldsymbol{x}) + b \tag{3-1}$$

where $\Phi(\boldsymbol{x}) = [\phi_1(\boldsymbol{x}), \cdots, \phi_D(\boldsymbol{x})]$ is a nonlinear mapping function $\Phi(\cdot)$: $\mathbb{R}^d \to \mathbb{R}^D$ which maps the parameter space of dimension d into the corresponding *feature space* of dimension D; $\boldsymbol{w} \in \mathbb{R}^D$ is a vector collecting the unknown coefficients of the nonlinear regression; $b \in \mathbb{R}$ is a bias term that is retrieved as a by-product of the solution in [16]; $\boldsymbol{w}^T \Phi(\boldsymbol{x})$ is defined as the inner product in $\mathbb{R}^D$ [113, 116]. The dimensionality of the *feature space* D is defined by the nonlinear map $\Phi(\boldsymbol{x})$.

Assuming that we can tolerate a deviation of at most ε between $\mathcal{M}^{SVR}(\boldsymbol{x})$ and y, so only when the absolute value of the difference between $\mathcal{M}^{SVR}(\boldsymbol{x})$ and y is greater than ε, it needs to reduce this deviation. Then, the SVR model expression can be formalized to find $\boldsymbol{w}$ following the minimization equation [113]:

$$\min_{\boldsymbol{w}} \frac{1}{2}\|\boldsymbol{w}\|^2 + C \sum_{i=1}^N \mathcal{L}^{\varepsilon}\left(\mathcal{M}^{SVR}(\boldsymbol{x}_i), y_i\right) \tag{3-2}$$

where $C \in \mathbb{R}^+$ is a regularization parameter, chosen by cross-validation, which provides a trade-off between the accuracy of the model on the training data set and its flatness in order to avoid

overfitting leading to an oscillating behavior [113]; $\mathcal{L}^{\varepsilon}$ is the ε-insensitive loss function, which is most widely used as follows (called: $\mathcal{L}_1$-penalization) [113,116]:

$$\mathcal{L}_1^{\varepsilon}(\boldsymbol{x}; y) = \begin{cases} 0 & if \left|\mathcal{M}^{SVR}(\boldsymbol{x}) - y\right| < \varepsilon, \\ \left(\left|\mathcal{M}^{SVR}(\boldsymbol{x}) - y\right| - \varepsilon\right) & otherwise. \end{cases} \tag{3-3}$$

A nonlinear regressor considering this loss function is illustrated in Figure 3.1 (a). Any points that are outside the ε–insensitive tube need to be penalized, illustrated in Figure 3.1 (b).

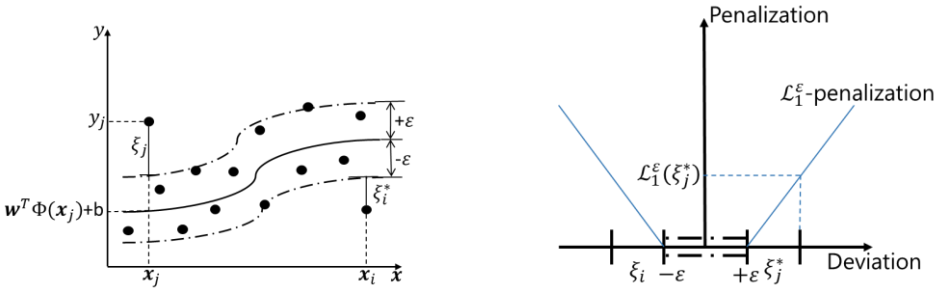

(a) (b)

Figure 3.1 (a) only the vectors outside the ε -insensitive tube (dotted line area) are penalized; (b) Penalization of deviations larger than ε for $\mathcal{L}^{\varepsilon}$ loss function [158]

The best combination of the parameters $(\boldsymbol{w}, b)$ is found to minimize the deviation of the model predictions from the training samples outside the ε-intensive zone. This can be done via the following optimization problem [113, 116]:

$$\begin{aligned} &\underset{\boldsymbol{w}, b}{min}\ \frac{1}{2}\|\boldsymbol{w}\|^2 + C\sum_{i=1}^{N}(\xi_i + \xi_i^*), \\ &\text{Subject to } y_i - \boldsymbol{w}^T\boldsymbol{\Phi}(\boldsymbol{x}_i) - b \le \varepsilon + \xi_i, \\ &\boldsymbol{w}^T\boldsymbol{\Phi}(\boldsymbol{x}_i) + b - y_i \le \varepsilon + \xi_i^*, \\ &\xi_i, \xi_i^* \ge 0, for\ i = 1, \cdots, N \end{aligned} \tag{3-4}$$

where ξ_i and ξ_i^* are the slack variables, which measure the deviation from the insensitive tube.

Then, equation (3-3) can be solved by using the Lagrangian functions [113, 116], which is explained in Appendix D. Therefore, equation (3-1) can be rewritten as [113]:

$$\mathcal{M}^{SVR}(\boldsymbol{x}) = \boldsymbol{w}^T\Phi(\boldsymbol{x}) + b = \sum_{i=1}^{N}(\alpha_i - \alpha_i^*)k(\boldsymbol{x}_i, \boldsymbol{x}) + b \tag{3-5}$$

where the coefficients α_i, α_i^* are Lagrange multipliers that are calculated by maximizing the Lagrangian function in Appendix D.

The parameters for building a SVR metamodel in this chapter are shown below, implemented within UQLAB version 2.0 [158], which is fully compatible with the MATLAB environment. UQLAB is a general purpose Uncertainty Quantification framework developed at ETH Zurich (Switzerland), which is made of open-source scientific modules.

- Loss function: L_1 ε-insensitive.
- Kernel function: Gaussian radial basis function (RBF)

$$k_{Gaussian}(\boldsymbol{x}_i, \boldsymbol{x}_j) = \exp(-\frac{\|\boldsymbol{x}_i - \boldsymbol{x}_j\|^2}{2\sigma^2}) \tag{3-6}$$

where $\|\boldsymbol{x}_i - \boldsymbol{x}_j\|$ is the Euclidean distance between $\boldsymbol{x}_i$ and $\boldsymbol{x}_j$. The larger this distance, the smaller the value of RBF. $\sigma > 0$ is the width of the RBF. The smoothness of the Gaussian RBF is controlled by the magnitude of σ (the higher σ, the smoother the Gaussian RBF).

3.2.2 Multigene genetic programming algorithm metamodeling

In MGPA, each prediction M^{MGPA} of the model output is formed by the weighted output of the genes plus a bias term. Each gene is a function of the d input variables $\boldsymbol{x} = \{x_1, \cdots, x_d\}$ representing the input variables of the system. Given a training data set of N samples $\{(\boldsymbol{x}_i, y_i)\}_{i=1}^{N}$ ($y = M(\boldsymbol{x})$ is the model response of the system supposed to be a scalar quantity with a finite variance, where M is a numerical model presenting the observed phenomenon), the MGPA metamodel can be expressed as [114]:

$$M^{MGPA}(\boldsymbol{x}) = d_0 + d_1 \times gene\ 1 + \cdots + d_Q \times gene\ Q$$

$$= d_0 + d_1 \times$$ 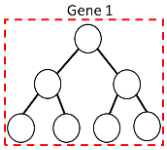

$$+ d_2 \times$$ 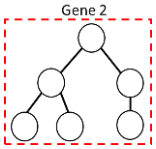

$$+ \cdots + d_Q \times$$ 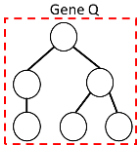

(3-7)

where d_0 is the bias term, $d_1, \cdots, d_Q$ are the gene weights and Q is the number of genes. The weights $\boldsymbol{d}$ ($\boldsymbol{d} = [d_0\ d_1\ \cdots\ d_Q]$) for the genes are automatically determined by using an ordinary least square method to regress the genes against the training data set [114]. Each gene combines a set of elementary functions with the input variables (such as sum, multiplication, division, logarithm, arctangent, hyperbolic tangent, sine, exponential, power function, etc.), and the gene depth is the number of levels in the gene structure. The expression of the MGPA metamodel is evolved automatically by using the training data set [114-118].

The process of building a metamodel with the MGPA method is [114]:

1) Load the training data set (a set of existing input values and corresponding model response values);

2) The genetic algorithm works on a population of metamodels, each one representing a potential solution for expressing the relationship between the input variables and the model response. The initial population of the metamodels is evolved automatically by using the training data set. During its evolution, this algorithm transforms the current population of metamodels into a new population by applying the classical genetic

operations (selections, cross-over, mutation, etc.) [159]. When it achieves the maximum generation, the MGPA metamodel will be picked out in terms of high coefficient of determination (R^2) and low model complexity [114]. The model complexity is computed as the simple sum of the number of nodes (the number of elementary functions plus the number of occurrences of the input variables) inside its constituent genes [160], and R^2 is calculated as below [114]:

$$R^2 = 1 - \frac{\sum_{i=1}^{N}(M(\boldsymbol{x}_i) - M^{MGPA}(\boldsymbol{x}_i))^2}{\sum_{i=1}^{N}(M(\boldsymbol{x}_i) - \frac{1}{N}\sum_{i=1}^{N} M(\boldsymbol{x}_i))^2} \tag{3-8}$$

where $M(\boldsymbol{x}_i)$ is the i^{th} value from the studied system, $M^{MGPA}(\boldsymbol{x}_i)$ is the predicted value on the MGPA metamodel, and N is the number of samples in the training data set. This value ranges from 0 to 1.

In this chapter, the MGPA toolbox is provided by GPTIPS, which is a free, open-source MATLAB-based software platform [114]. It can automatically evolve both the structure and the parameters of the mathematical model from the training data set, but how to appropriately define the maximum number of genes and the maximum gene depth for an accurate MGPA metamodel needs to be carefully considered.

3.2.3 Sparse polynomial chaos expansions metamodeling

Polynomial Chaos Expansions (PCE) is a metamodeling technique that aims at providing a functional approximation for the relationship between the input variables and model output in a non-intrusive way [115, 161-162]. It means that it focuses only on the one-to-one mapping relationship between input and output. Furthermore, the post-process of the PCE metamodel can also help to find the most influential input variable to the model output.

3.2.3.1 Sparse PCE

It starts by considering the vector $\boldsymbol{x} \in \mathbb{R}^d$ collecting d independent input variables $\{x_1, \cdots, x_d\}$ with a joint probability density function (PDF) $f_{\boldsymbol{X}}(x)$, representing the input variables of the physic system. Given a training data set of N samples $\{(\boldsymbol{x}_i, y_i)\}_{i=1}^{N}$ ($y = M(\boldsymbol{x})$ is the model response of the system supposed to be a scalar quantity with a finite variance, where M is a numerical model presenting the observed phenomenon), the PCE metamodel is established to simulate the varying trend of the model response [115, 163]:

$$M^{PCE}(\boldsymbol{x}) = \sum_{\alpha \in \mathbb{N}^d} \hat{c}_\alpha \Phi_\alpha(\boldsymbol{x}) \tag{3-9}$$

where $\hat{c}_\alpha$ are the unknown deterministic coefficients, and $\Phi_\alpha(\boldsymbol{x})$ are multivariate polynomials basis functions which are orthonormal with respect to the joint PDF $f_{\boldsymbol{x}}(x)$. $\alpha \in \mathbb{N}^d$ is a multi-index that identifies the components of the multivariate polynomials Φ_α. If the input variables have a uniform distribution, the orthogonal polynomial is Legendre; while if the input variables have a Gaussian distribution, the orthogonal polynomial is Hermite [163]. The distribution of input variables and orthogonal polynomials used in PCE is shown in Table 3.1, where k is the corresponding

polynomial degree.

Table 3.1 Distribution of input variable and orthogonal polynomial used in PCE [163]

Type of input variable	Distribution	Orthogonal polynomials	Polynomial basis
Uniform	$1_{]-1,1[}(x)/2$	Legendre $P_k(x)$	$P_k(x)/\sqrt{\frac{1}{2k+1}}$
Gaussian	$\frac{1}{\sqrt{2\pi}}e^{-\frac{x^2}{2}}$	Hermite $H_{ek}(x)$	$H_{ek}(x)/\sqrt{k!}$

The coefficients $\hat{c}_\alpha$ are obtained by post-processing of the experimental design $\{(\boldsymbol{x}_i, y_i)\}_{i=1}^N$, a training data set consisting of N samples of the input variables and the corresponding model responses y. From the set of model responses, the coefficients can be estimated by the ordinary least square regression method [115-116, 152, 163]. For this, the infinite series in equation (3-8) has to be truncated. Choosing a maximum polynomial degree p, the usual truncation scheme preserves all polynomials associated with the set [115-116, 152, 163]:

$$\mathcal{A}^{d,p} = \{\alpha \in \mathbb{N}^d : \|\alpha\|_1 = \sum_{i=1}^d \alpha_i \leq p\} \tag{3-10}$$

Thus, the cardinal of the set $\mathcal{A}^{d,p}$ denoted $L = \frac{(d+p)!}{d!p!}$ increases quickly with the number of input variables d and the degree p of the polynomials [115-116]. This leads that the size of the PCE retained in the set $\mathcal{A}^{d,p}$ will be too large when dealing with high-dimensional problems.

In order to overcome this limitation, a hyperbolic truncation strategy $\mathcal{A}_q^{d,p}$ based on the total degree p and a parameter q, with $0 < q < 1$, allowing to reduce the size of the PCE basis is then defined as follows [115-116, 152, 163]:

$$\mathcal{A}_q^{d,p} = \left\{\alpha \in \mathbb{N}^d : \|\alpha\|_q = \left(\sum_{i=1}^d \alpha_i^q\right)^{\frac{1}{q}} \leq p\right\}. \tag{3-11}$$

This favors the most relevant effects and low-order interactions, which are known to have the largest impact on the variability of the model response according to the sparsity-of-effects principle [163-165]. It is important to point out that lower values of q imply a larger number of neglected high-rank interactions. In addition, when $q = 1$, this scheme is equivalent to the standard PCE. When $q < 1$, the retained terms of the polynomial basis can be substantially reduced [115-116, 152]. These truncation schemes are represented for two input variables ($d = 2$) in Figure 3.2 (a) and (b), with the squares illustrating the terms of the polynomial basis of degree less than or equal to $p = 5$. It can be found that for $q = 0.5$, this scheme chooses a number of polynomials smaller than those selected from a standard truncation set $\mathcal{A}^{d,p}$ as in Figure 3.2 (a).

When the number of input variables is large, the standard truncation needs a lot of numerical model responses to calculate all the coefficients of the PCE metamodel, but the hyperbolic truncation strategy can reduce the number of coefficients that are estimated in PCE. However, this method may still demand many numerical model responses to evaluate the remaining coefficients. So, the number of elements of the polynomial basis may be further decreased by using the Least

Angle Regression (LARS) algorithm [115-116, 152, 163]. This allows selecting the polynomial bases having the most effect on the model response in the truncation set $\mathcal{A}_q^{d,p}$. Noting the K cardinal of the hyperbolic truncation strategy and the K polynomial bases, LARS builds up a sparse representation containing from 1 to K polynomial bases in an iterative manner according to their decreasing impact. The algorithm begins by researching the basis Φ_{α_1}, which is the most correlative with the model response y. In fact, the correlation is evaluated from a set of the model response y. Next, the second polynomial basis Φ_{α_2} is estimated to have the same correlation with the residual $y - \hat{c}_{\alpha_1}^{(1)}\Phi_{\alpha_1}$. Then, the improvement of the basis is carried out by moving in the direction $(\Phi_{\alpha_1} + \Phi_{\alpha_2})$ until the current residual has the same correlation as a third polynomial basis Φ_{α_3}, and so on. Finally, the LARS algorithm provides a set of sparse approximations containing more and more polynomial terms. An illustration of the selected polynomials by LARS after some iterations is given by the cyan squares in Figure 3.2 (c).

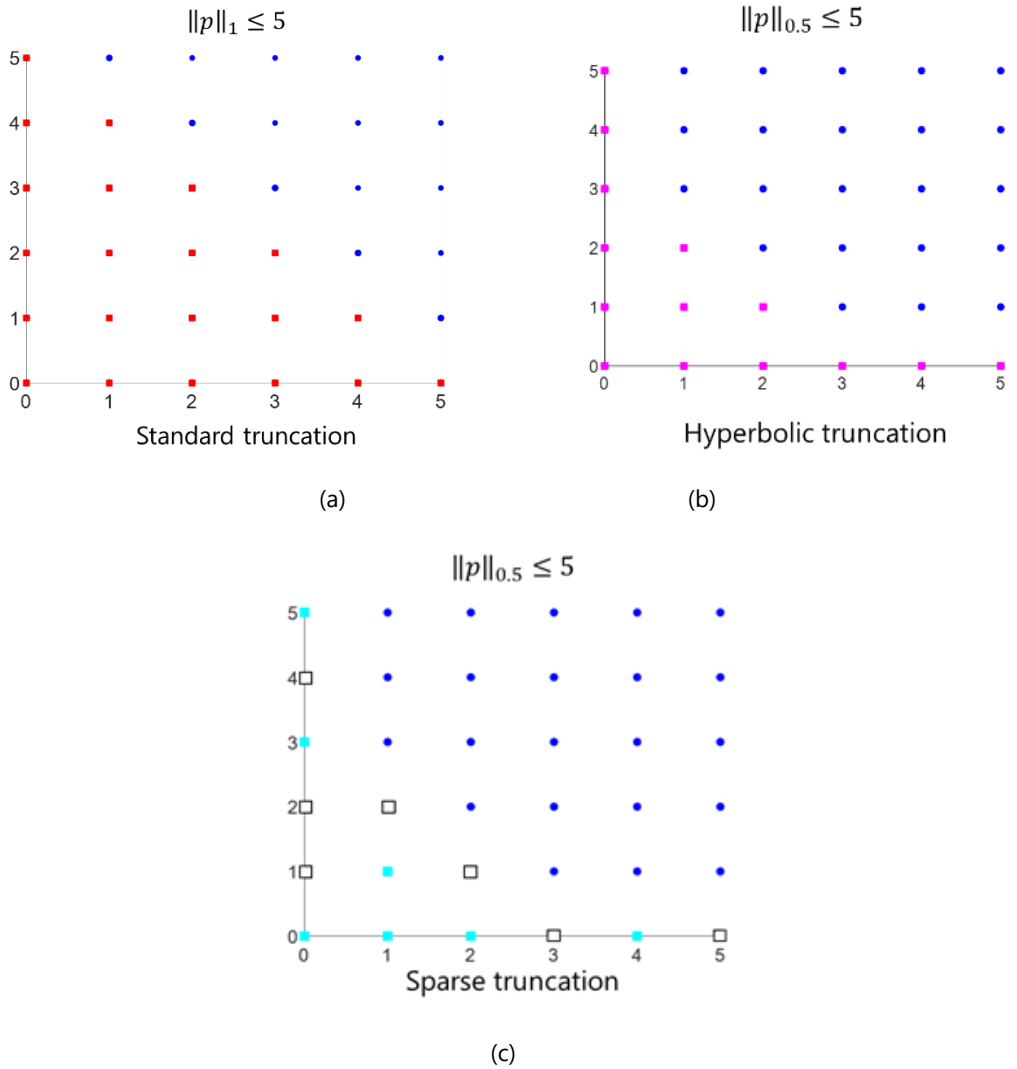

Figure 3.2 Number of terms of the polynomial basis of degree less or equal to the degree $p = 5$ retained by the hyperbolic truncation strategy when (a) $q = 1$ (squares) and (b) $q = 0.5$ (squares). (c) Numbered squares are the polynomial basis terms selected by the LARS algorithm [115]

3.2.3.2 Sensitivity Analysis-PCE based Sobol' indices

Post-processing of the coefficients of the PCE metamodel can be performed at a relatively low computational cost. Indeed, the orthonormality property of the polynomial basis allows estimating the expectation (statistical mean value) and the variance of the model response y for the given input variables and their probability distributions [115, 163]. The mean value of the PCE metamodel is the coefficient of the constant basis term $\Phi_0 = 1$, and the variance summarizes the coefficients of the non-constant basis terms, which are shown below:

$$\text{Mean value: } \hat{\mu}_y = \mathbb{E}[\mathrm{y}] = \hat{c}_0 \tag{3-12}$$

$$\text{Variance: } \hat{\sigma}_y^2 = \mathbb{V}[M^{PCE}(\boldsymbol{x})] = \mathbb{E}\left[\left(\sum_{\substack{\alpha \epsilon A \\ \alpha \neq 0}} \hat{c}_\alpha \Phi_\alpha(\boldsymbol{x})\right)^2\right] = \sum_{\substack{\alpha \epsilon \mathcal{A} \\ \alpha \neq 0}} \hat{c}_\alpha^2 \tag{3-13}$$

The global sensitivity analysis aims at quantifying which input variable (for a given probability distribution) influences the model response variability most. It can be calculated on the PCE coefficients. The first-order PCE-based Sobol index S_i of the model response y quantifies the additive effect of each input parameter separately [115, 121, 155-156, 165]:

$$S_i = \frac{D_i}{D} = \frac{\mathbb{V}_{\boldsymbol{x}_i}(\mathbb{E}_{\boldsymbol{x}_{\sim i}}(M^{PCE}(\boldsymbol{x})|\boldsymbol{x}_i))}{\mathbb{V}[M^{PCE}(\boldsymbol{x})]} = \frac{\sum_{\alpha \epsilon \mathcal{A}_i} \hat{c}_\alpha^2}{\sum_{\substack{\alpha \epsilon \mathcal{A} \\ \alpha \neq 0}} \hat{c}_\alpha^2} \tag{3-14}$$

with $\mathcal{A}_i = \{\alpha \in \mathcal{A}: \alpha_i > 0, \alpha_j = 0 \; \forall j \neq i\}$ and $\boldsymbol{x}_{\sim i}$ notation indicates the set of all variables except $\boldsymbol{x}_i$. The first-order PC-based Sobol indices of the i^{th} variable is closer to 1 means that the i^{th} variable has more impact on the model response y.

The PCE metamodeling technique used in the thesis is also implemented within UQLAB version 2.0 [158]. The advantage of the PCE method is that it needs a small number of training samples to achieve accurate results when using the LAR method compared to the standard PCE models. Another strong advantage, as described above, is to easily perform a sensitivity analysis to determine the most impacting variable since Sobol's indices can be directly expressed with the coefficients of the polynomials. However, how to define the maximum degree p and the parameter q effectively needs to be carefully considered.

3.2.4 Error estimates of a metamodel

After the metamodel is constructed, its accuracy can be quantified by estimating the Root Mean Square Error (RMSE) obtained with the metamodel on the training data set. It is defined as:

$$\varepsilon_{RMSE} = \sqrt{\frac{\sum_{i=1}^{\mathrm{N}} (M^{metamodel}(\boldsymbol{x}_i) - M(\boldsymbol{x}_i))^2}{N}} \tag{3-15}$$

where $M(\boldsymbol{x}_i)$ is the model response of the training data set, $M^{metamodel}(\boldsymbol{x}_i)$ is the prediction value from the metamodels above, and N is the number of samples in the training data set.

Except the training data set used to construct the metamodel, a test data set different from the training samples, can be used to validate the predictive performance. The test error between

the test data set and the predictive values on the metamodel can be calculated by RMSE.

If no test data set is available, especially when it is the case with expensive computational models, a way to estimate the accuracy is the Leave-One-Out (LOO) cross-validation technique. It consists in building N separate metamodels $M^{metamodel\backslash i}$, each one created on a reduced model evaluation $\boldsymbol{x}\backslash\boldsymbol{x}_i = \{\boldsymbol{x}_j, j = 1, \cdots, N, j \neq i\}$ and comparing its prediction on the excluded point $\boldsymbol{x}_i$ with the real value $M(\boldsymbol{x}_i)$. The error criterion used in this work to calculate LOO error can be written as [115, 121, 155-156]:

$$\epsilon_{LOO} = \frac{\sum_{i=1}^{N}(M(\boldsymbol{x}_i) - M^{metamodel\backslash i}(\boldsymbol{x}_i))^2}{\sum_{i=1}^{N}(M(\boldsymbol{x}_i) - \frac{1}{N}\sum_{i=1}^{N} M(\boldsymbol{x}_i))^2} \tag{3-16}$$

It is important to note that the smaller the LOO error is, the better the prediction of the metamodel is.

3.3 Metamodels for different couplers taking into account sources of uncertainty

The aim of this section is to determine how the performance of a static RIPT system can be affected by the sources of uncertainty, such as the misalignment along the X/Y axis, the variation in the air gap, and the rotation on the receiver with regard to the transmitter.

3.3.1 Sources of uncertainty

To investigate the efficiency of the static RIPT system, it is mandatory to take into account the sources of uncertainty, such as variations in the misalignment of the receiver due to imperfect parking alignment and variations in the air gap due to loading and unloading the vehicle. Figure 3.3 shows the rotation angle along the Z axis α, the misalignment along the X axis Δx, the misalignment along the Y axis Δy, and the air gap between two coils Δz for the circular couplers. These situations also take place in the square, DD, and BP couplers.

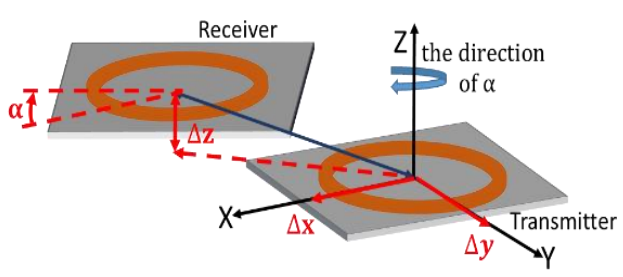

(a) Influencing factors in the couplers (example of circular couplers)

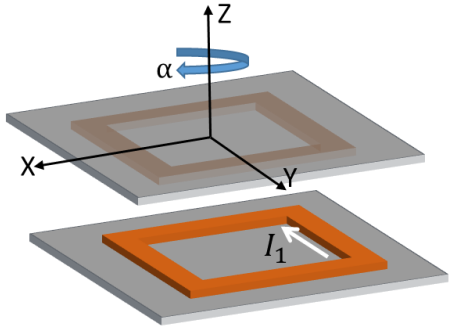

(b) Square couplers

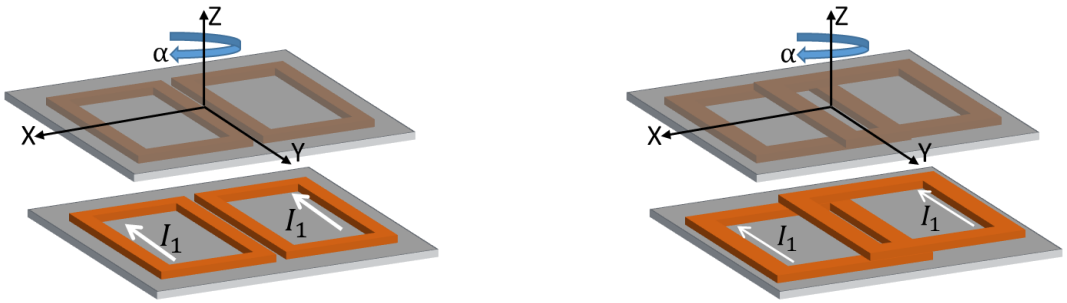

(c) DD couplers (d) BP couplers

Figure 3.3 Influencing factors for the four shapes of couplers

The impact of these influencing factors on the static RIPT system's maximum transmission efficiency can be approximated to the impact on the mutual inductance M due to Equation (2-5) when the length of coils is predefined. The mutual inductance M is numerically computed as $M = \left|\frac{V_2}{2\pi f_0 I_1}\right|$ defined as the ratio between the open-circuit voltage V_2 of the receiver and the current I_1 in the transmitter.

Before performing the uncertainty analysis, it is necessary to assume a probability distribution for the sources of uncertainty. Here, a Gaussian distribution is chosen for these influencing factors, which conforms to the probability that may happen in reality. The statistical parameters of the influencing factors are displayed in Table 3.2. The range of the air gap and the rotation angle along the Z axis are referred to [40]. Meanwhile, the range for the misalignment along the X/Y axis is considered reasonably due to the size of the parking space and the size of the EV chassis. Nonetheless, the small-scale couplers are studied in this chapter, so these ranges are also reduced by the same scaling factor of 10 (indicated in Chapter 2).

Table 3.2 Properties of the influencing factors

Parameters	Symbol	Distribution	Mean value	Standard Deviation
Misalignment along X axis [mm]	Δx	Gaussian	0	15
Misalignment along Y axis [mm]	Δy	Gaussian	0	15
Air gap between two coils [mm]	Δz	Gaussian	15	2
Rotation angle along Z axis [deg]	α	Gaussian	0	3

3.3.2 Comparison of the metamodels on small-scale square couplers

Here, the square couplers are taken into account first because they can be used in the static RIPT or dynamic RIPT systems [3-5]. Then, the SVR with RBF kernel, MGPA, and the sparse PCE metamodeling techniques are implemented to build a metamodel for small-scale square couplers and are compared below. The results given in this section were done with a XEON E5-1620, 8-cores processor, working at 3.70 GHz. The 3D model of the couplers is obtained by COMSOL 5.6, and the SVR and PCE metamodels are calculated in MATLAB 2019b with the UQLAB Framework,

while the MGPA metamodel is calculated in MATLAB 2017b due to the limitation of the GPTIPS toolbox functions.

3.3.2.1 Latin hypercube sampling method

Building an accurate metamodel often requires a large number of samples. Meanwhile, considering the complexity of the studied model and the high number of input variables, how to effectively sample from the space of input variables is a problem. So, the Latin Hypercube Sampling (LHS) method was first proposed in 1979 and pointed out by McKay that it was an effective and practical technique for taking samples from constrained sampling spaces [166-167]. In the LHS method, the number of samples can be specified arbitrarily according to the requirements and does not increase with the number of input variables. The way to take samples by the LHS method is as follows.

The number of input variables is d, and the number of samples in the data set is N. Next, the probability distribution of each input variable is divided into N equal probability intervals. Then, one sample is randomly selected from each probability interval in each variable. Finally, these samples are randomly combined together to form the data set.

In this thesis, the LHS method is used to select the data sets for the metamodeling techniques.

3.3.2.2 Comparison of the metamodels on small-scale square couplers

The SVR with RBF kernel, MGPA, and the sparse PCE methods have been adopted to quantify the impact of these uncertainty parameters on the mutual inductance M of small-scale square couplers. In addition, the parameters on MGPA and sparse PCE methods are chosen considering the metamodel accuracy and the computational time to build an accurate metamodel. The SVR with RBF kernel builds a metamodel in light of the L_1 ε-insensitive loss function. The MGPA metamodel is performed with the following settings: Population size = 300, Number of generations = 100, Maximum number of genes = 6 and Maximum gene depth = 4. The sparse PCE metamodel is constructed by the adaptive degree method [115, 163], in which the degree of PCE metamodel varies from 3 to 15 in order to select the most accurate one. The hyperbolic scheme in Equation (3-10) is set to $q = 0.75$ to reduce the size of the polynomial basis.

All of the metamodels have been trained from the same training dataset containing 387 samples distributed according to the LHS method. This data set results from COMSOL simulations with a computational cost of 6h (one simulation with the full solver of the COMSOL model takes about 50 s). In order to investigate the performance of the obtained metamodels, their predictions are then compared with a test data set containing 613 samples. The test data set is totally different from the training data set and is also selected by the LHS method. Table 3.3 provides a detailed comparison of the accuracy and the computational cost of the proposed metamodelling techniques by collecting the RMSE on the training data set and on the test data set, along with the corresponding computational time $t_{training}$ and the predictive time $t_{predictive}$ (to predict one output) respectively. It also shows that the sparse PCE metamodel turns out to use the least

computational time and to be the most accurate metamodel with a training RMSE and a test RMSE, which is better than the accuracies obtained by the SVR and MPGA metamodels.

Table 3.3 Comparison of the accuracy and the computational cost of the SVM, MPGA, and PCE metamodels computed for the square couplers

Method	**Training RMSE**	**Test RMSE**	$t_{training}$	$t_{predictive}$
COMSOL computations	-	-	6.45 hours	60 s
SVR (RBF)	0.0266	0.0420	2.48 s	<1s
MGPA	0.0233	0.0475	313.54 s	<1s
Sparse PCE	0.0158	0.0270	0.357 s	<1s

Furthermore, 1000 samples selected by the MC method are computed in COMSOL to form a new data set. Figure 3.4 provides the scatter plots for the metamodels of the mutual inductance on the SVR, MGPA, and sparse PCE methods. These plots emphasize a good agreement between these metamodels and this data set for the reason that the samples are very close to the solid lines.

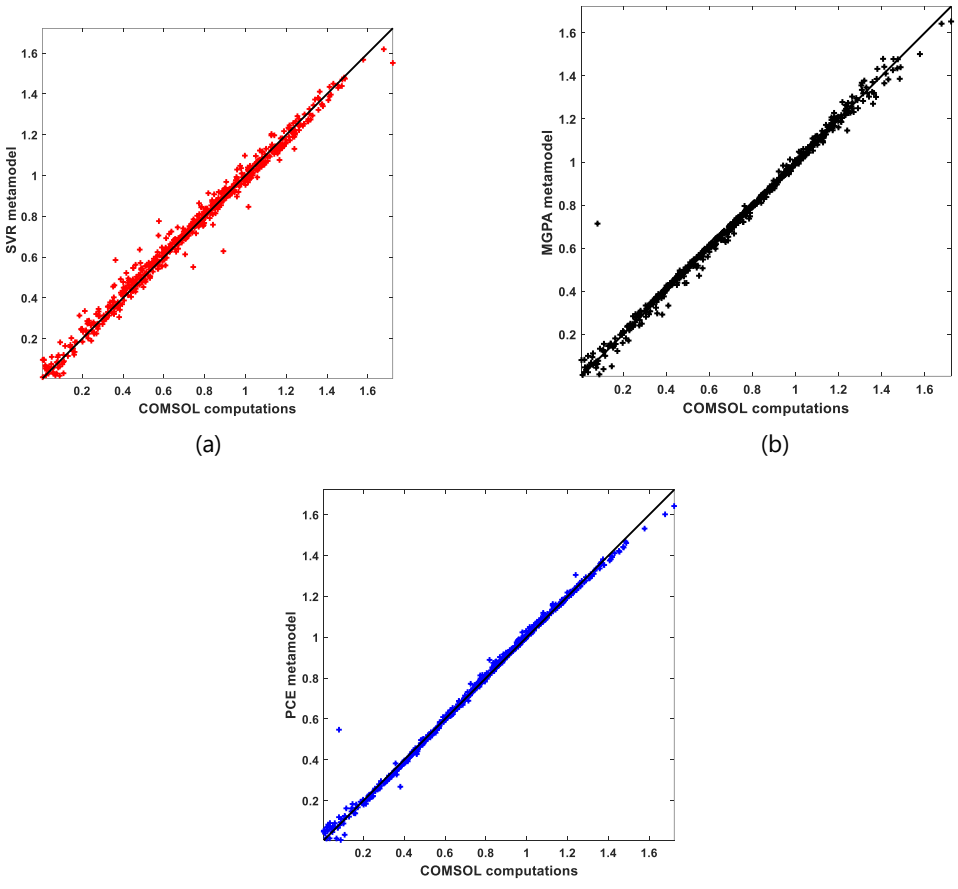

Figure 3.4 Scatter plots of the mutual inductance providing a comparison among the predictions of the SVR metamodel with RBF kernel (red marker in (a)), the MGPA metamodel (black marker in (b)), the sparse PCE metamodel (blue marker in (c)) and the results of COMSOL computations.

Then, the impact of the influencing factors on the mutual inductance is illustrated in Figure 3.5, where the probability density functions (PDFs) of the mutual inductance estimated via the SVR, MGPA, and sparse PCE metamodels are compared with the PDF of the COMSOL computations. It can be seen that the variability of the mutual inductance is well captured by these metamodels, which confirms a good estimation of the PDF of the mutual inductance with these metamodels and highlights a similar level of accuracy. In terms of computational cost, this data set, including 1000 samples, required about 14 h to compute in COMSOL, while the metamodels on the SVR, MGPA, and sparse PCE need less than 1 s, as shown in Table 3.3. It is worth noting that this computational cost does not include the time to generate the 387 training samples from LHS needed for constructing the metamodels, which cost nearly 5.5 h in COMSOL.

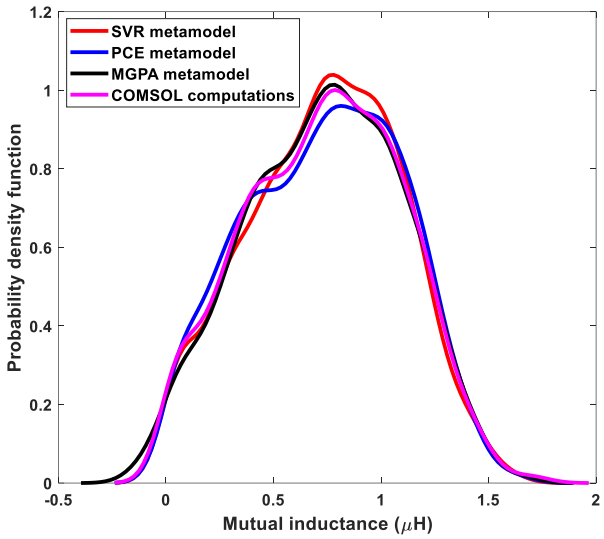

Figure 3.5 PDFs of the mutual inductance obtained from the SVR (solid red curve), MGPA (solid black curve) and sparse PCE metamodels (solid blue curve) compared with the PDF of COMSOL computations (solid magenta curve).

Compared to the other metamodeling techniques based on the same dataset, the sparse PCE metamodeling technique uses less time to build a metamodel and provides more accurate results. So, it is chosen to analyze the mutual inductance of different couplers, taking into account sources of uncertainty.

3.3.3 Sparse PCE metamodels for different shapes of couplers

Although the four shapes of couplers have been compared with regard to the misalignment in Figure 2.5, they are not discussed, taking into account the sources of uncertainties. So, sparse PCE metamodels on circular, square, DD, and BP couplers will be analyzed below.

3.3.3.1 Sparse PCE metamodel process

To examine the effect of the influencing factors defined above (Figure 3.3) on the mutual inductance M for different shapes of couplers, the sparse PCE metamodels are built up with the

adaptive degree l varying from 3 to 15, and the hyperbolic scheme in Equation (3-10) is set to $q = 0.75$. Due to the tradeoff between the accuracy of the sparse PCE metamodel and the computation time, the training data sets containing 387 samples obtained from LHS are chosen for circular, square, DD, and BP couplers.

In order to observe the quality of the sparse PCE metamodels on different shapes of couplers, the training LOO errors are presented in Table 3.4, and PDFs of the mutual inductance M given by sparse PCE metamodels on test data sets are presented in Figure 3.6. It can be seen that the variability of the mutual inductance is well captured by circular/square sparse PCE metamodels, which confirms a good estimation of the PDF of the mutual inductance with these metamodels and highlights a similar level of accuracy. However, the variability of the mutual inductance for DD/BP couplers has some difference between sparse PCE metamodels and the test data sets. Then, it can be deduced that the number of the training samples from COMSOL to build accurate sparse PCE metamodels also depends on the shape of the coils. The relationship between the mutual inductance M and the influencing factors of DD/BP coils is more complex than that of the circular/square coils, so to improve the accuracy of the sparse PCE metamodel of the DD/BP coils, more samples from COMSOL need to be considered. The time to calculate one mutual inductance M in COMSOL is about 1 min, but the time to calculate the mutual inductance on the sparse PCE metamodel is less than 1s.

Table 3.4 Properties of sparse PCE metamodels for different couplers

Coil Shape	Size of the training data set	Sparse PCE metamodel LOO Error (%)
Circular	387	0.014%
Square	387	0.024%
DD	387	4.4%
BP	387	5.1%

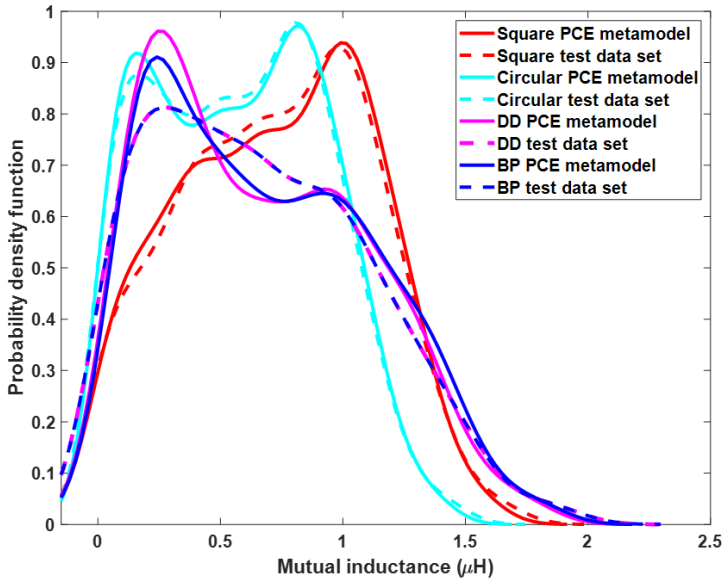

Figure 3.6 PDFs of mutual inductance M obtained from the sparse PCE metamodel for different couplers

3.3.3.2 PCE metamodel post-process-Sensitivity analysis

Beyond the quantification of the variability of the mutual inductance M, the sparse PCE metamodel provides a sensitivity analysis at a low computational cost. To better explain the sensitivity analysis, the influencing factors in the four shapes of couplers are shown in Figure 3.3. Then, Figure 3.7 presents the bars showing the values of the First-order Sobol index, calculated from Equation (3-13), of the sparse PCE metamodels for the four shapes of couplers.

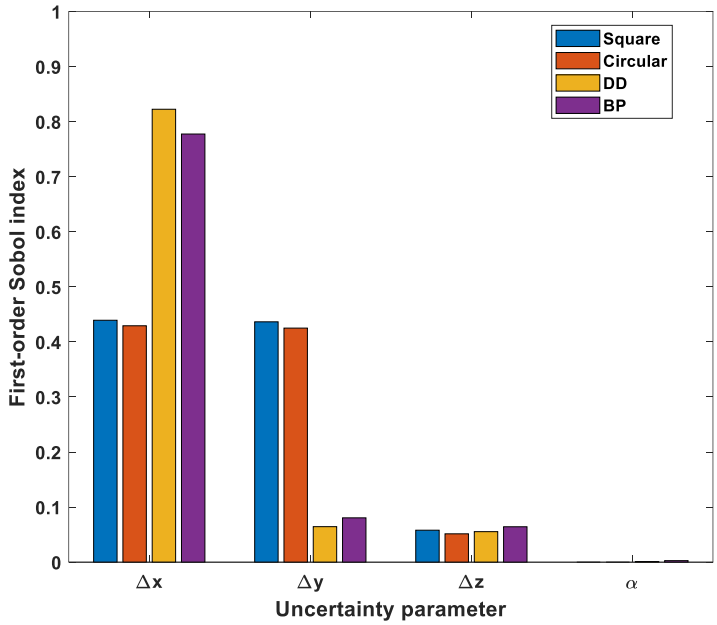

Figure 3.7 First-order Sobol index of mutual inductance M for different couplers

It can be seen that the variations of the mutual inductance M are mainly related to the misalignment along the X axis, as shown in Figure 3.7 for DD/BP coils, because of a larger area reduction where the magnetic field lines pass through, compared to along the Y axis (see in Figure 2.5). However, for square and circular coils, the misalignment along the X or Y axis demonstrates nearly the same impact on the mutual inductance M due to the symmetry of the shape. The rotation along the Z axis has almost no effect on the mutual inductance M, independently of the shape of the coils compared to other influencing factors (for the given deviation range of the influencing factors).

In order to further study the impact of the misalignment along the X/Y axis for the different couplers, the influence of different ranges of the misalignment is also studied with the air gap = 15 mm and a rotation angle of 0 degrees. According to the trend between the coupling coefficient and the misalignment in [161], the standard deviations of these uncertainties are considered to be 2 mm, 5 mm, and 10 mm, as shown in Table 3.5. They are based on the small scale of the couplers (which is ten times smaller compared to the real scale of coils considering the real situation in daily life).

Table 3.5 Different standard deviations of misalignment for different couplers

Parameters	Symbol	Distribution	Mean value	Standard Deviation
Misalignment along X axis [mm]	Δx	Gaussian	0	2/5/10
Misalignment along Y axis [mm]	Δy	Gaussian	0	

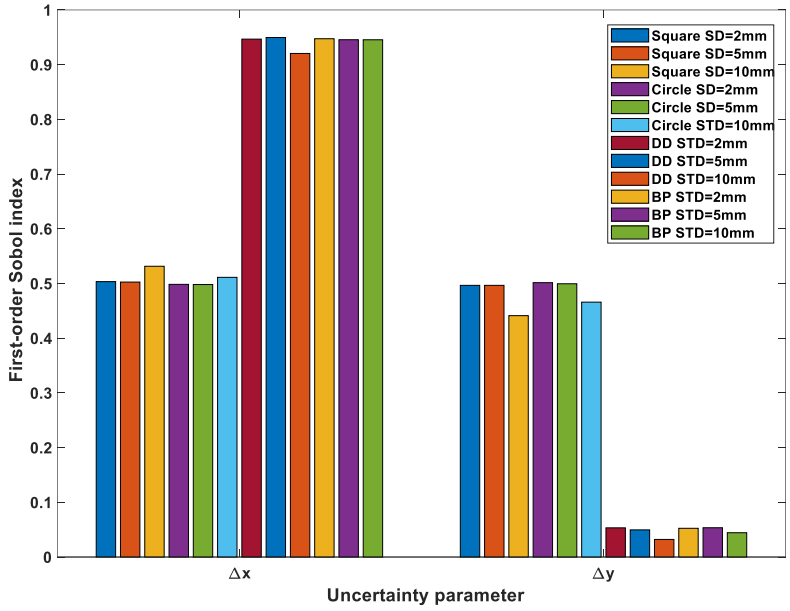

Figure 3.8 First-order Sobol index of mutual inductance M for different couplers with different standard deviations

From Figure 3.8, it is shown that the relative influence of the misalignment along the X/Y axis is independent of the standard deviations for different couplers as long as they vary in the same way for both parameters. For DD/BP couplers, the misalignment along the X axis is still the most important parameter for the mutual inductance M.

3.3.4 Comparison of the couplers and discussion

Due to Equation (2-5), it shows that the maximum transmission efficiency η_{max} increases with the ratio $\frac{l}{M}$ decreasing when the frequency is predefined. So, the ratio $\frac{l}{M}$ can be chosen as a criterion to verify which shape of coils leads to the maximum transmission efficiency. According to the sparse PCE metamodel analysis above, how the sources of uncertainty impact the mutual inductance M of the four shapes of couplers is clear.

Table 3.6 shows the nominal mutual inductance M, the nominal ratio $\frac{l}{M}$ and the maximum transmission efficiency η_{max} for the different couplers at the nominal position (the nominal position means that the transmitter and the receiver are in alignment). It can be observed that circular couplers lead to the least length of wires and to the maximum transmission efficiency compared to the other shapes of coils.

Table 3.6 Properties of the static RIPT couplers in the nominal position

Coil Shape	Length l [cm]	M [μH]	Ratio $\frac{l}{M}$ [cm/ μH]	Maximum Transmission Efficiency η_{max} %
Square	93.1	1.26	73.9	95.0%
Circle	73.1	1.08	67.7	95.5%
DD	131.0	1.34	97.8	92.9%
BP	139.9	1.36	102.9	91.9%

When the sources of uncertainty (in Table 3.2) are taken into account in the couplers, the results obtained by the sparse PCE metamodel for different couplers provide interesting information on the behavior of the mutual inductance M.

Table 3.7 gives the mean value and the standard deviation of the mutual inductances M based on the sparse PCE metamodels. The M for DD/BP couplers varies more than those of circular/square couplers within these influencing factors. So, DD/BP are not the best configurations for the coils in the static RIPT system. Then this table also shows the mean value of the ratio $\frac{l}{M}$, the mean value, and the standard deviation of maximum transmission efficiency. According to the sensitivity analysis above, the misalignment along the X/Y axis has the most effect on the mutual inductance M, and these factors will make the mean value of the mutual inductance much smaller than the nominal one (in Table 3.6).

From the point of the mean value and the standard deviation of η_{max} shown in Table 3.7, circular couplers appear to reach better performances for the given distribution of influencing factors (defined in Table 3.2), even if a significant difference occurs in the value of the mutual inductance for different coils. Nonetheless, the mean value of η_{max} of circular couplers is very close to that of square couplers. These findings also show an interest in investigating the maximum transmission efficiency rather than only the mutual inductances when comparing different couplings systems.

Table 3.7 Statistical properties of the sparse PCE metamodel for static RIPT couplers

Sparse PCE Metamodel	Coil Shape	Mean Value of M $E[M^{PCE}]$ [μH]	Standard Deviation of M^{PCE} $\sigma_{M^{PCE}}$ [μH]	Mean Value of Ratio $E[\frac{l}{M^{PCE}}]$ [cm/ μH]	Mean Value of Maximum Transmission Efficiency $E[\eta_{max}]$%	Standard Deviation of η_{max} $\sigma_{\eta_{max}}$ %
$M^{PCE}(\boldsymbol{x})$	Square	0.730	0.375	127.5	91.45%	83.36%
	Circle	0.574	0.341	127.3	91.48%	85.63%
	DD	0.674	0.532	194.4	86.97%	83.50%
	BP	0.694	0.498	201.6	86.49%	81.17%

3.4 Conclusion

This chapter has highlighted the metamodel techniques for the comparisons of different coupling coils with ferrite plates taking into account the sources of uncertainty for the RIPT system. It verifies that the metamodel techniques are helpful in analyzing the RIPT system.

Section 3.2 provides an overview of SVR with RBF kernel, MGPA, and PCE metamodeling techniques. When the metamodels are built by these techniques, the ways to evaluate the accuracy and build the PDF are also summarized.

In Section 3.3, some metamodel techniques (SVR with RBF kernel, MGPA, and PCE) are built and compared for analyzing the mutual inductance M on the small-scale square couplers considering sources of uncertainty. Due to the tradeoff between the computational time and the accuracy of the metamodel, the sparse PCE metamodel is chosen to analyze the mutual inductance M for different shapes of couplers. Then, sparse PCE metamodels on these four couplers are performed. According to the sensitivity analysis based on the coefficients of PCE metamodels, the misalignment along the X axis appears to be the most influential factor in the mutual inductance M for DD/BP couplers, whereas the misalignment along the X/Y axis has the same effect as the circular and the square couplers, due to their symmetries. Meanwhile, the ratio $\frac{l}{M}$ helps to design the shape of the coils for maximum transmission efficiency, considering the sources of uncertainty defined in this chapter. Circular couplers should be recommended for the static inductive power transfer system due to their higher value of the maximum transmission efficiency (compared to the other couplers), taking into account the given sources of uncertainty.

Although circular couplers can provide the maximum transmission efficiency statically in the aligned position, square couplers are chosen for the design of the RIPT system because they have a good performance either in static charging or dynamic charging through the analysis in Figure 2.6 or Table 3.7. How to design the ferrite and aluminum plate for square couplers remains a difficult task due to the absence of analytical expressions between the efficiency and the dimension parameters.

However, the sparse PCE metamodeling technique is verified that it is a very useful tool in the analysis of RIPT systems in order to save computational time and computational resources. How to combine this metamodeling technique with the design process on the ferrite and aluminum will be studied in the next chapter.

CHAPTER 4 DESIGN AND OPTIMIZATION OF RIPT SYSTEMS

4.1 Introduction

Design optimization is an engineering methodology to select the optimal design among many alternatives. Design optimization exists in several forms that are applied in RIPT systems:

- Parameter optimization: It allows for doing a parametric sweep on geometry dimensions or material properties, such as the ferrite length and width, coil wire position, number of coil turns, a separation between turns, size and position of ferrites, etc. [51, 55, 88-106];

- Shape optimization: It allows to deform the boundaries of the geometry, such as the coil shape, the ferrite shape, or the shielding shape;

- Topology optimization (TO): It allows to determine whether a certain point of the predefined candidate volume is void or solid, for example, how to arrange the ferrite structure under the transmitter or above the receiver [107-110].

Recently, much literature used multiobjective optimization algorithms with 3D FEMs to analyze the performance of RIPT systems with several design variables [51, 55, 88-106, 168]. However, a comprehensive parametric sweep can be very time-consuming, depending on the number and the ranges of design variables. To save computational time, some approaches are proposed by some researchers:

1) To deduce the mathematical expressions describing the relationships between the design variables and the objectives (such as self-inductances, mutual inductances, magnetic flux density leakage, and so on);

2) To simulate every design configuration based on 3D numerical methods, e.g. FEM.

If a complex coupler configuration with a large number of variables is involved in the design process, it is very difficult to deduce the analytical expressions between design variables and the objectives for RIPT systems. Meanwhile, in COMSOL, the time for a single 3D FEM calculation could be between about 1~5 minutes on an Intel Xeon W-2125 processor, which depends on the size of the 3D model and the size of the mesh elements. Until now, there is no comprehensive methodology allowing stable and efficient design optimization for RIPT systems.

In addition to parameter optimization methods used in RIPT systems, TO is also developed in the ferrite design of RIPT systems [107-110]. The main TO methods are the solid isotropic material with the penalization (SIMP) method [111], the on-off method [112], and others. The main advantage of TO is that it can lead to novel structures, but it is limited by the size of the design domain and the discretization of the domain. In [107-108], the coil and magnetic-core shapes are optimized using the on-off method with the aid of a genetic algorithm and 3D FEM so that the coupling coefficient of the WPT system is maximized. Reference [109] proposed a TO method for the WPT system using the geometry projection method to generate the bar-shaped magnetic cores. In [110], TO is applied with the SIMP method to optimize the ferrite structure for circular couplers. Although these papers optimize the ferrite installed on circular/DD couplers, they do not consider

how the ferrite structure varies under different ferrite volume constraints, and they do not give any guidelines to arrange the ferrite placement.

Therefore, the purpose of this chapter is to come up with a fast and reliable methodology for the optimization of the RIPT system. The method is to combine the PCE metamodeling technique with multiobjective optimization algorithms, and the optimization process takes into account the transmission efficiency and the volume/cost of the RIPT system. Next, the objective functions in this work are shown below:

- the mutual inductance PCE metamodel M^{PCE} with design variables $\boldsymbol{x}$, which has to be maximized referred to the equation (2-5) for the maximum transmission efficiency;
- the volume of the ferrite plates / the cost of the shielding (the ferrite plates and an aluminum plate above the receiver), which has to be minimized in order to save the budget of the RIPT system.

After, two multiobjective optimization methods (Non-dominated Sorting Genetic Algorithm II (NSGA-II) [122]/ Multiobjective Particle Swarm Optimization (MOPSO) [123]) are both used and compared to find a more efficient one combing the PCE metamodeling method. Then, TO with the SIMP method is used in this obtained size of the ferrite plates. It can further arrange the ferrite placement by minimizing the reduction in the value of the mutual inductance under the ferrite volume constraints.

4.2 Multiobjective optimization with PCE metamodeling technique

The multiobjective optimization process of the RIPT system proposed in our work is presented in Figure 4.1. First, a PCE metamodel is built to describe the mutual inductance M dependence with the design variables (in the orange line framework) based on a number of training samples from 3D FEM computations, and it works as the first objective functions instead of 3D FEM calculations (in the dotted line framework). Although the process of generating a number of training samples by 3D FEM takes a certain amount of time, the prediction of the mutual inductance M on PCE metamodel costs less than 1 second. Next, the second objective function is the volume of the ferrite plates / the cost of the shielding (the ferrite plates and an aluminum plate above the receiver). Then, it can save several times the computational time for the whole optimization process compared to the 3D FEM computations with multiobjective optimization algorithms.

The proposed methodology is applied in 2 cases: one case is the RIPT system without shielding, and the other case is the RIPT system with shielding.

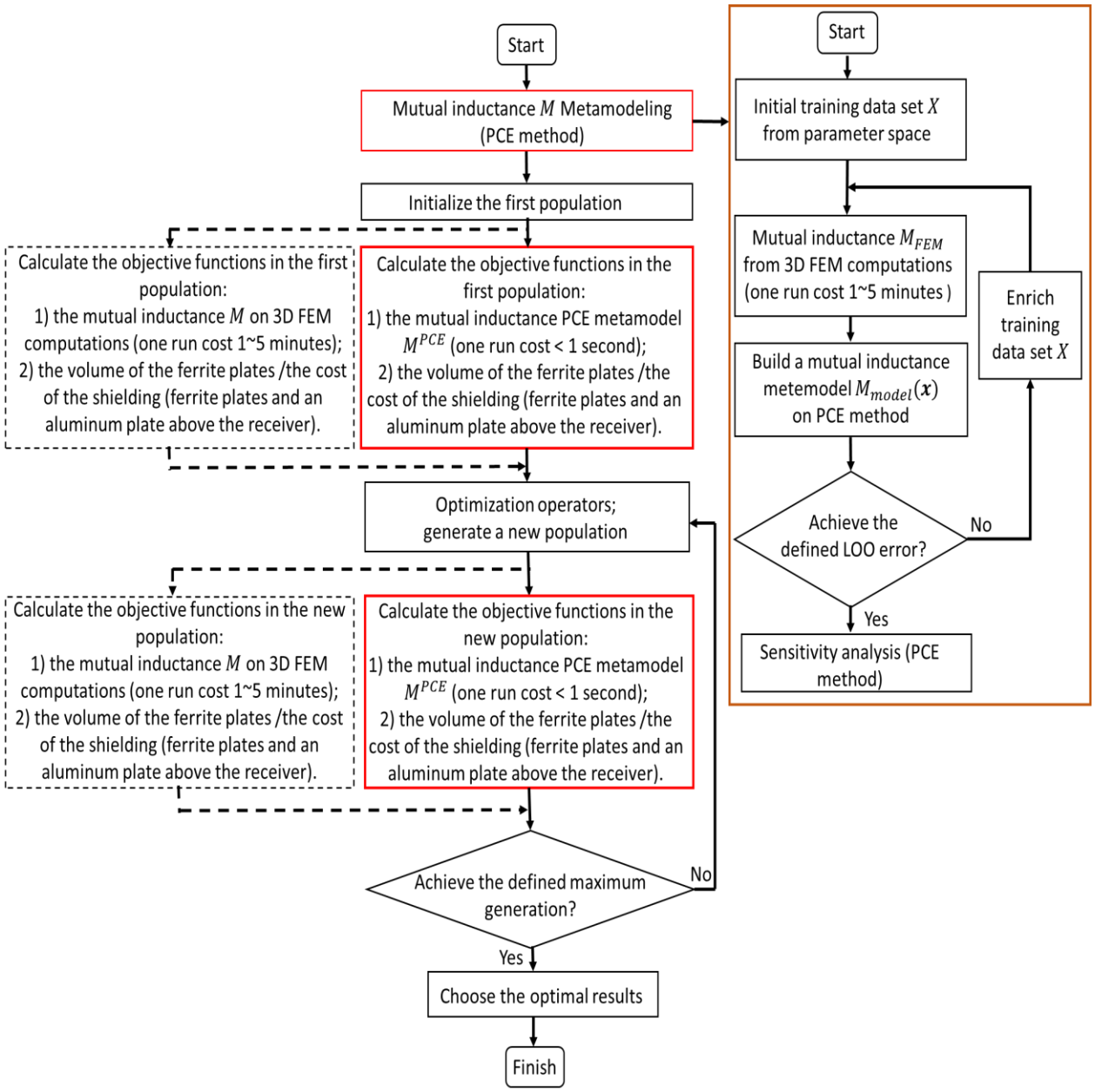

Figure 4.1 General flowchart of the design optimization process for the RIPT system

4.2.1 RIPT system without shielding

Normally, the ferrite plates are used to retain the flow of magnetic flux between the transmitter and receiver coils to enhance the charging efficiency. In contrast, the ferrite volume will increase the weight of the RIPT system and lead to a high price. So, the dimension of ferrite plates should be optimized with respect to improving the mutual inductance. Here, the NSGA-II optimization algorithm is adopted for optimizing the dimensions of ferrite plates. It is a well-known, fast sorting and elite multiobjective genetic algorithm. Then, one of two objective functions is the mutual

inductance PCE metamodel M^{PCE}, and the other is the volume of the ferrite plates, which is proportional to the weight of the ferrite plates.

Generally, the NSGA-II initializes the population based on the ranges of design variables and constraints. Then, it sorts the initialized population on nondomination criteria. Once the sorting is complete, the crowding distance value is assigned front wire. The individuals in the population are selected based on rank and crowding distance. The selection of individuals is carried out using a binary tournament selection with a crowded-comparison operator [122]. The offspring population and current generation population are combined, and the individuals of the next generation are set by selection. The new generation is filled by each front subsequently until the population size exceeds the current population size. The NSGA-II stops when the maximum number of generations is exceeded. The flowchart of NSGA-II is presented in Figure 4.2.

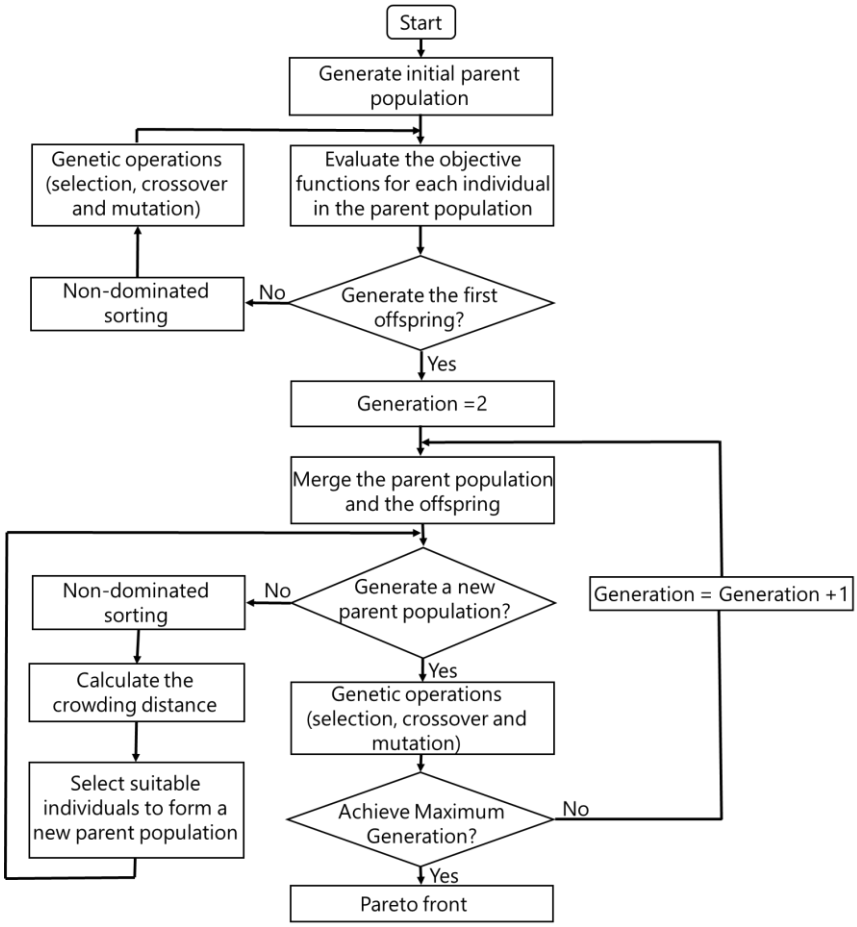

Figure 4.2 Flowchart of NSGA-II [122, 169]

In this section, the optimization process is performed by using the function "gamultiobj" in MATLAB Global Optimization Toolbox [169]. The number of individuals in the population is defined to 100, the generations are limited to 200, the crossover probability is 0.8, and the mutation probability is 0.2.

4.2.1.1 GeePs practical RIPT system

Here, the practical RIPT configuration developed by GeePs laboratory and Vedecom institute is shown in Figure 4.3, and structure parameters are listed in Table 4.1 [80, 170]. The shape of the transmitter and receiver coils is square, and they are made of Litz wires in two layers (one layer has three turns). The external length of the coils is 468 mm, and the thickness is 13 mm; the relative permeability of the ferrite is 3000.

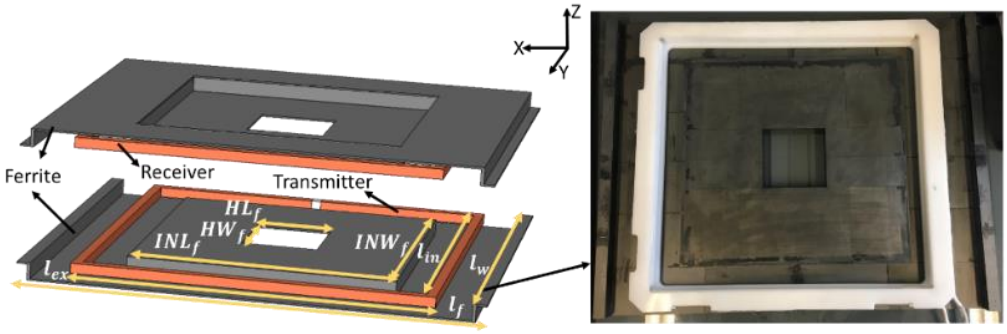

(a) 3D structure view

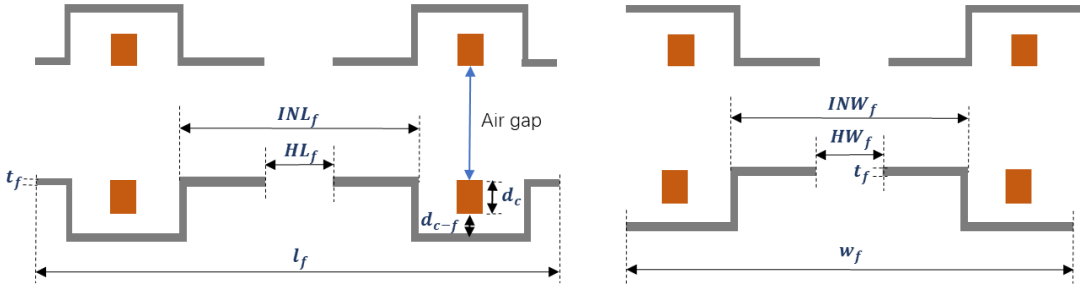

(b) 2D Cross section structure view (more details are in Appendix F)

Figure 4.3 Studied RIPT configuration [80, 170]

Table 4.1 Parameters of the studied RIPT configuration [80]

Symbol	Quantity	Value [Unit]
l_{ex}	External length dimension of the coils	468 [mm]
l_{in}	Internal length dimension of the coils	442 [mm]
d_c	Coil thickness	13 [mm]
w_f	Ferrite length	600 [mm]
l_f	Ferrite width	500 [mm]
t_f	Ferrite thickness	2 [mm]
INL_f	Inner ferrite length	350 [mm]
INW_f	Inner ferrite width	350 [mm]
HL_f	Hole length	100 [mm]
HW_f	Hole width	100 [mm]
d_{c-f}	Distance between coil and ferrite	8 [mm]
Air gap	Distance between the transmitter and receiver	150 [mm]

Then, five structural variables are considered for the optimization. Although they have been studied separately for improving the mutual inductance M [80], the volume of ferrite is not paid attention to before. The range and probability density distribution of these variables are listed in Table 4.2.

Table 4.2 Structural variables of the studied RIPT configuration

Variables Number	Structural Variables	Min [mm]	Max [mm]	Probability Density Distribution
1	Ferrite length l_f	500	600	Uniform
2	Inner ferrite length INL_f	300	400	
3	Inner ferrite width INW_f	300	400	
4	Hole length HL_f	50	150	
5	Hole width HW_f	50	150	

So, a sparse PCE metamodel is established to express the varying trend of the mutual inductance M. The training data set to calculate in COMSOL is selected by the LHS method. The hyperbolic scheme in Equation (3-10) is set to $q = 0.4$ to reduce the size of the polynomial basis. In Figure 4.4, it is shown that LOO error decreases with the number of training samples increasing. That is to say, the accuracy of PCE metamodel increases with more training samples. To make a balance between the LOO error and the computation time of training samples, 135 samples are chosen to build an accurate PCE metamodel of the mutual inductance M with these five design variables.

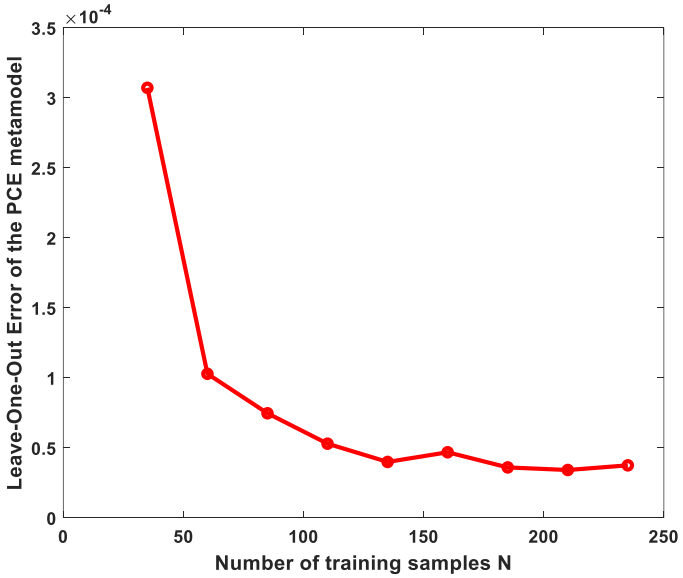

Figure 4.4 Leave-one-out Error with number of training data N

According to the sensitivity analysis of the PCE metamodel in Figure 4.5, it appears that the ferrite length is the most important parameter related to the mutual inductance M among these input variables. This will be helpful in choosing the values from the optimization results in the next step.

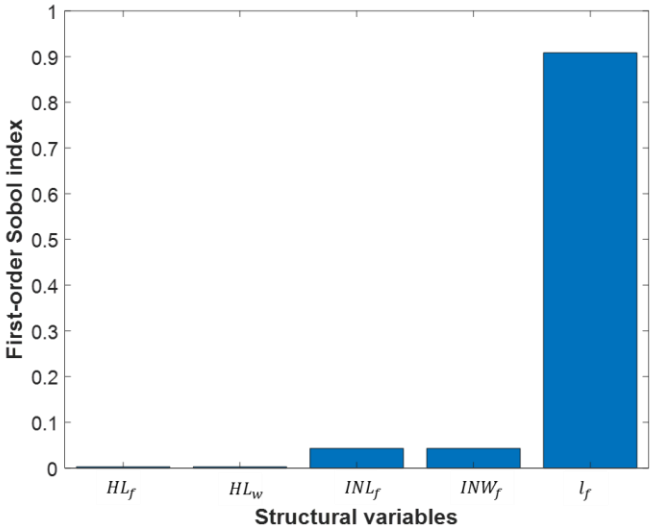

Figure 4.5 First-order Sobol index of mutual inductance M on practical RIPT system

In Figure 4.6, it can be seen that the mutual inductance M increases with the ferrite volume V increasing even if the ferrite thickness t_f keeps the same value during this optimization process. The red point represents the initial mutual inductance and the initial ferrite volume (based on the existing coupler in Figure 4.3). All the points on the Pareto front satisfy the compromise between the objective functions above, but the chosen point should keep nearly the same mutual inductance M as the initial values in the studied configuration and decrease the ferrite volume V. Therefore, the blue asterisk point is picked out from these points.

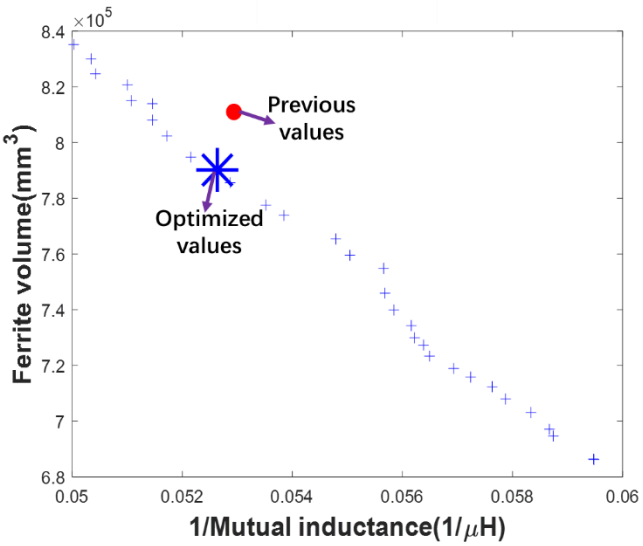

Figure 4.6 Pareto front between $1/M$ and V on Practical RIPT system

Since the evaluation of M based on the PCE metamodel requires one or two seconds, the multi-objective optimization procedure with PCE metamodels needs less than 10 minutes. The optimized parameters of the studied RIPT configuration are shown in Table 4.3. Compared to the initial size of

the ferrite in Figure 4.3, the optimized results help to save 44156 mm^3 of the ferrite (22078 mm^2 of the ferrite surface), which means that it decreases by nearly 3% of the ferrite.

Table 4.3 Optimized values of the studied RIPT configuration

Structural Parameter	Optimized value [mm]
Ferrite length l_f	573
Inner ferrite length INL_f	387
Inner ferrite width INW_f	378
Hole length HL_f	114
Hole width HW_f	126

To evaluate the performance of the RIPT system, the mutual inductance M, and the magnetic flux density leakage B_{max} should be carefully studied. The measurement point of B_{max} is determined along a vertical line at 800 mm from the center of the coupler, shown in Figure 4.7 [40]. A comparison between the optimized design and the initial structure is performed in case of misalignment during the charging process.

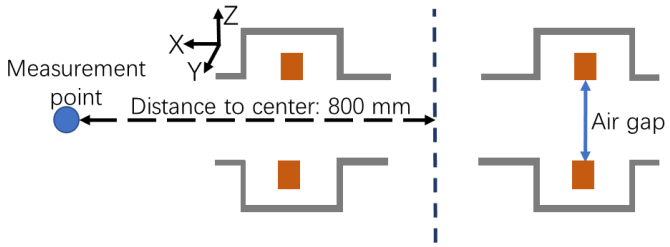

Figure 4.7 Measurement point for the magnetic flux density B_{max}

In Figure 4.8, the mutual inductance M in the studied configuration with the optimized values nearly keeps the same value as that with the initial values, no matter which misalignment along the X or Y axis happens.

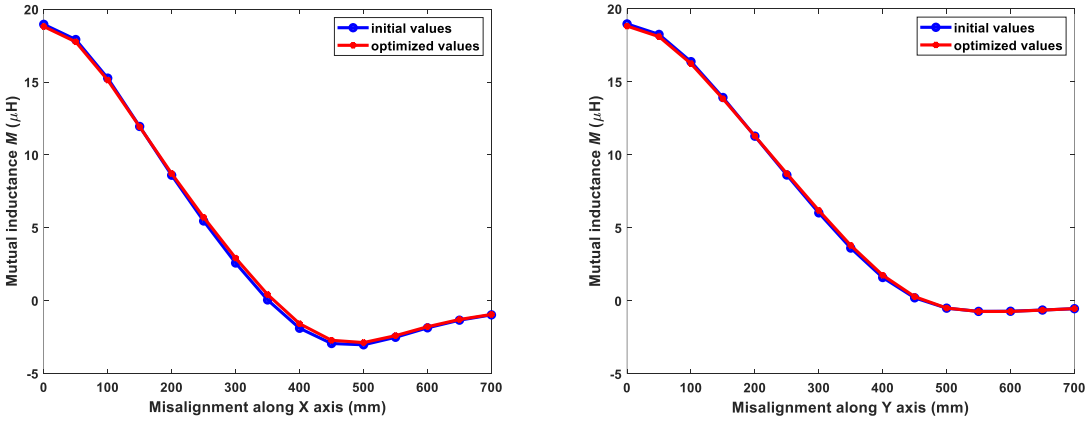

Figure 4.8 Variation of the mutual inductance M with the variation of the misalignment

Figure 4.9 dedicates that the magnetic flux density B_{max} from the initial values and the optimized values are both smaller than the RMS value 27μT and meet the ICNIRP regulations [45].

However, B_{max} from the optimized values is smaller than that from the initial values, independently of the misalignment along the X or Y axis.

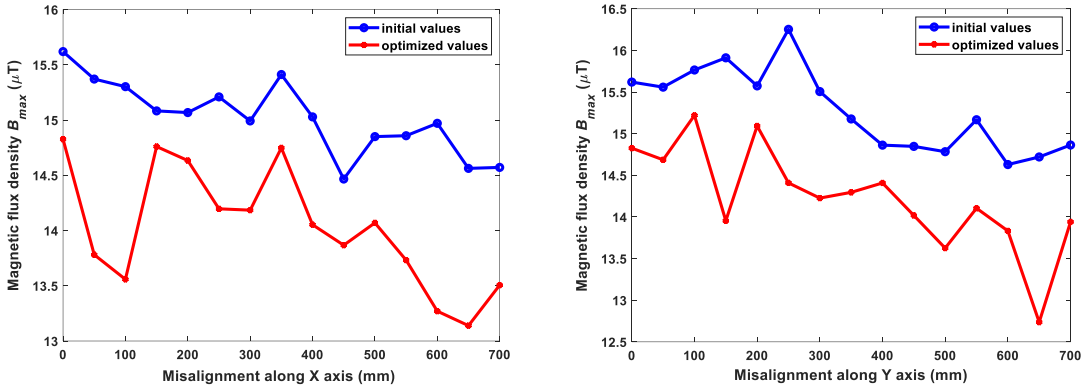

Figure 4.9 Variation of the magnetic flux density B_{max} with the variation of the misalignment

4.2.1.2 General ferrite design for a standard configuration of RIPT system

In general, the ferrite plate in many RIPT systems is a rectangular or square plate, just as shown in Figure 4.10. The parameters of the general RIPT system are listed in Table 4.4. However, finding the proper dimensions of the ferrite plate (length, width, and thickness) is a difficult task. There is no general criteria or rule to help in this choice for a given coil size. So it is meaningful to find the relationship between the coil size and the ferrite size. The ranges of structural variables are displayed in Table 4.5 when the square coil size is 468 mm. This size corresponds to a case developed in the GeePs laboratory before [80], and the relative permeability of this ferrite plate is 2500.

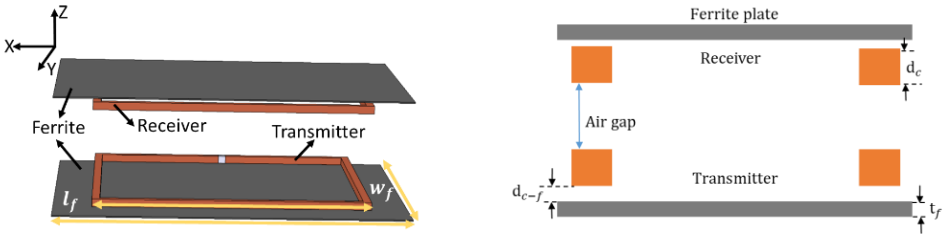

(a) General view (b) Cross-sectional view

Figure 4.10 General RIPT ferrite plates structure illustrating the design variables

Table 4.4 Parameters of the general RIPT system

Symbol	Quantity	Value [Unit]
d_c	Coil thickness	13 [mm]
w_f	Ferrite length	600 [mm]
l_f	Ferrite width	500 [mm]
d_{c-f}	Distance between coil and ferrite	8 [mm]
t_f	Ferrite thickness	2 [mm]
N	Coil turns	6
Air gap	Distance between the transmitter and receiver	150 [mm]

Table 4.5 Structural variables of the ferrite plate

Variable Number	Structural Variable	Min [mm]	Max [mm]	Probability density distribution
1	Ferrite length l_f	468	936	Uniform
2	Ferrite width l_w	468	936	
3	Ferrite thickness t_f	2	10	
4	Distance between coil and ferrite d_{c-f}	1	10	

The PCE metamodel for the mutual inductance M^{PCE} is based on 116 training samples, and the LOO error is 3.12×10^{-6}. It is chosen according to the trade-off between the LOO error and the computation time of training samples. Then, considering the sensitivity analysis for the mutual inductance M in Figure 4.11, the length and width of ferrite are quite important for the mutual inductance M. This will help to decide the result during the optimization procedure, especially when there exist several results meeting the optimization conditions.

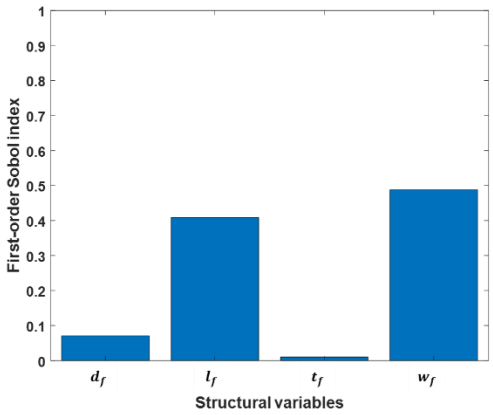

Figure 4.11 First-order Sobol index of the mutual inductance M and ferrite volume V

Then, using the NSGA-II optimization algorithm defined above, the Pareto front between the reciprocal of the mutual inductance M and the ferrite volume V is displayed in Figure 4.12.

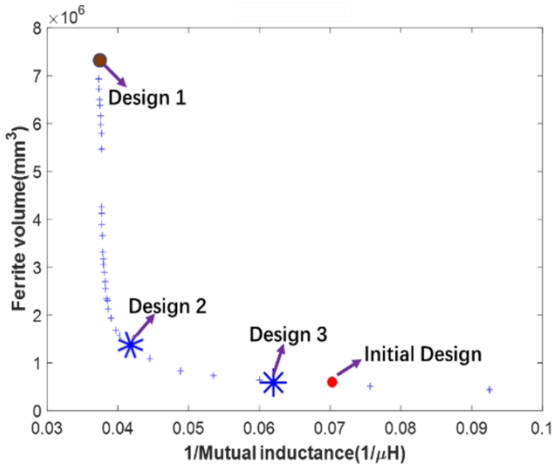

Figure 4.12 Pareto front between 1/Mutual inductance and ferrite volume for a general RIPT system

Table 4.6 Optimal structural variables of the ferrite plates

Design Number	**Ferrite length** $l_f\ [mm]$	**Ferrite width** $w_f\ [mm]$	**Ferrite thickness** $t_f\ [mm]$	**Distance between coil and ferrite** $d_{c-f}\ [mm]$	**Mutual inductance** $M\ [\mu H]$	**One ferrite volume** $V\ [mm^3]$
1	928	870	9	1.2	27.2	72.7×10^5
2	781	784	2	1.5	24.1	12.2×10^5
3	541	536	2	1.2	15.9	5.8×10^5
Initial	600	500	2	8.0	14.2	6.0×10^5

Table 4.6 concludes several possible designs of the ferrite plates from the Pareto front. In the table, Design 1 significantly improves the mutual inductance but leads to the most ferrite volume. Compared to the initial design, all the designs improves the mutual inductance, but only Design 3 decreases by nearly 3% of ferrite. In the studies above, it appears that Design 2 may be the best choice because it achieves nearly the maximum mutual inductance and the smallest ferrite volume on the Pareto front. At the same time, the mutual inductance can also be further improved by changing the structure of the ferrite, as described in Section 4.3.1.2.

However, considering a practical system for an electric vehicle, a low ferrite volume and a high mutual inductance are preferred, especially for the receiver which is installed in the electric vehicle. Therefore, in order to make a trade-off between the mutual inductance M and ferrite volume V, Design 2 can be used in the transmitter, and Design 3 can be used in the receiver, as shown in Figure 4.13.

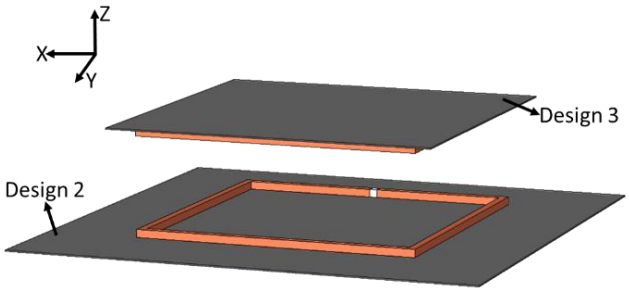

Figure 4.13 New ferrite arrangement for a general rectangular RIPT system

As shown in Figure 4.14 and Figure 4.15, the new ferrite arrangement improves the mutual inductance M and the tolerance to the misalignment and the magnetic flux density leakage (at the same position as shown in Figure 4.8).

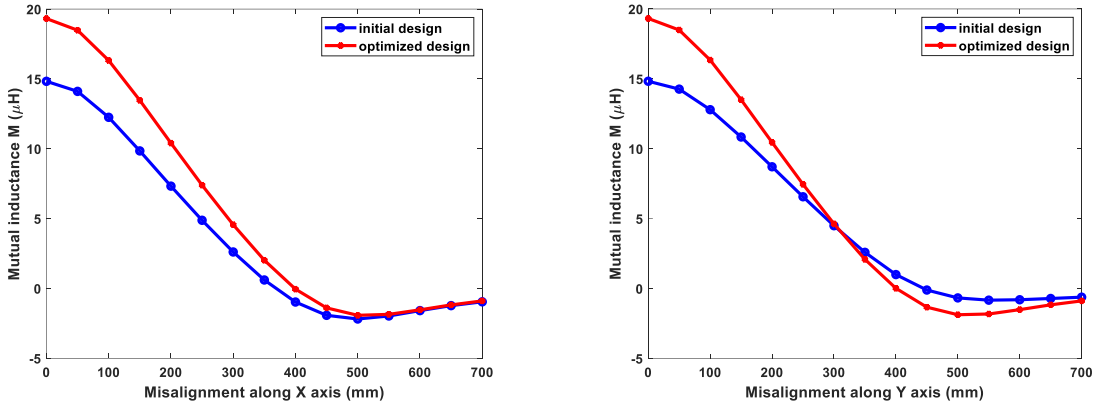

Figure 4.14 Comparison of the mutual inductance M with the variation of the misalignment between Figure 4.10 and Figure 4.13

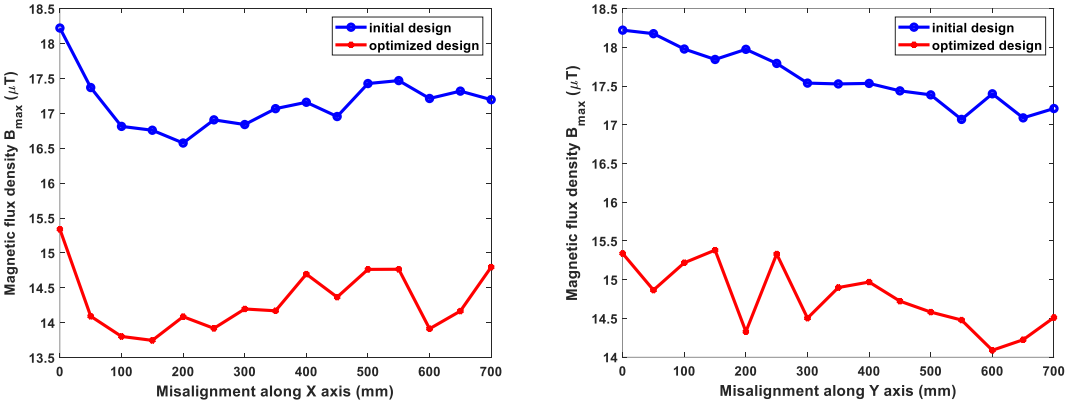

Figure 4.15 Variation of the magnetic flux density B_{max} with the variation of the misalignment between Figure 4.10 and Figure 4.13

4.2.2 RIPT system with shielding

The setting of the ferrite plates enhances the transmission field strength, improves the coupling between two coils, and shields the magnetic flux leakage. However, relying on them for the shielding is not only expensive but also often ineffective and heavy for the receiver installed on the EVs (the magnetic flux density above the receiver may exceed the limited value). Furthermore, the EV's chassis plate also acts as a shield to decrease the magnetic flux leakage. The chassis plate is generally made of two different materials respectively: one is steel material, and the other is carbon-fiber laminate (CF). In an EV charging RIPT system, the conductive chassis causes eddy current losses generated by the transmitting coil, and there is still a strong magnetic flux leakage outside the ferrite core plate [171]. Compared to steel plates, carbon fibers are slightly stiffer. Nowadays, carbon fiber production is expensive, so carbon-laminate composites are only used in structures that are entirely performance-oriented. However, the shielding performances of the CF composite panels are very poor [172]. So, it is necessary to place another material between the chassis and the receiver to shield the magnetic flux leakage. According to the literature, an aluminum plate is always added between the chassis and the ferrite for the receiver to mitigate the magnetic field generated by the RIPT transmitting coil, but it also reduces the transmission efficiency to a certain extent. Thus, how

to design such a size of the aluminum plate in practical 3D configurations remains a key point for maintaining transmission efficiency and mitigating the magnetic field leakage in the RIPT systems.

In the GeePs laboratory (see reference [80]), an aluminum plate has been designed above the receiver with the ferrite plate, as shown in Figure 4.16. The dimension of the aluminum plate is shown in Table 4.7.

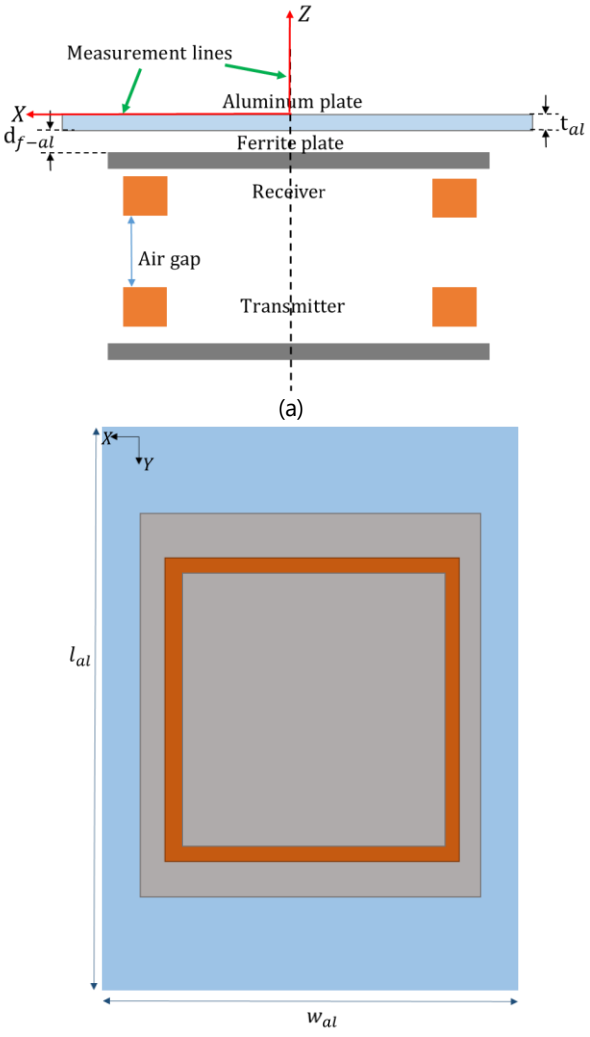

Figure 4.16 (a) A pair of coils (orange) with ferrite plates (grey) and an aluminum plate (blue); (b) a single square coil with a ferrite plate (grey) and an aluminum plate

Table 4.7 Parameters of the aluminum plate

Symbol	Quantity	Value [Unit]
w_{al}	Aluminum length	1800 [mm]
l_{al}	Aluminum width	800 [mm]
t_{al}	Aluminum thickness	2 [mm]
d_{f-al}	Distance between ferrite and aluminum	5 [mm]
σ_{al}	Aluminum conductivity	34.2 [MS/m]

4.2.2.1 Second-Order Artificial Material Single-Layer Method used in the aluminum plate

Nonetheless, the thickness of the aluminum plate is 2 mm. When it is modeled in the 3D FEM, it has to be meshed in the element sizes that are much smaller than the skin depth of the aluminum plate, but this method can lead to large memory and computational time requirements. Thus, specific modeling techniques are needed in order to save computational time and get accurate results. To choose the most efficient method, three existing methods are applied in the aluminum plate: traditional FEM [173], FEM using the transition boundary condition (TBC) [174], and the second-order Artificial Material Single Layer Method (AMSL_2nd order) [175].

In Table 4.8 (a), the thickness of the aluminum plate and its material properties are presented. Then, according to the equations in [175], the physical constants of AMSL_2nd order are shown in Table 4.8 (b), and these values replace the real material properties of the aluminum plate. After, the aluminum plate is discretized using only a single finite element layer [175-176].

Table 4.8 Aluminum material properties and physical constants of AMSL_ 2nd order

f [kHz]	Material	Thickness t_{al} [m]	Relative permittivity ε_{r_al}	Relative permeability μ_{r_al}	Conductivity σ_{al} [S/m]
85	aluminum	2×10^{-3}	1	1	3.42×10^{7}

(a) Aluminum material properties

f [kHz]	Material	Skin depth [m]	Relative permittivity $\tilde{\varepsilon}_r$	Relative permeability $\tilde{\mu}_r$	Conductivity $\tilde{\sigma}_r$ [S/m]
85	aluminum	2.9519×10^{-4}	-9.9374×10^{11}	$0.4082 - 0.0854\mathrm{i}$	1.2962×10^{7}

(b) Physical constants of AMSL_2nd order

Next, the results are obtained by calculating the coupler system with different meshing methods in the aluminum plate. The number of elements used to model the aluminum plate, the computational time, and the electrical parameters are reported in Table 4.9. Different meshing methods used in the aluminum plate don't influence the electrical parameters of the coupler system, but the AMSL_2nd order method uses less computational time than other methods.

Table 4.9 Computational time and electrical parameters for FEM with swept, TBC, and AMSL_2nd order methods

Mesh method in the aluminum plate	**Numbers of meshing elements in the aluminum plate**	**Total computation time [s]**	**Transmitter resistor R_1 $[\Omega]$**	**Transmitter self-inductance L_1 $[\mu H]$**	**Receiver resistor R_2 $[\Omega]$**	**Receiver self-inductance L_2 $[\mu H]$**	**Mutual inductance M $[\mu H]$**
traditional FEM	19000	294 s	0.183	63.0	0.192	57.7	10.9
FEM with TBC	0	195 s	0.183	63.0	0.193	58.1	11.0
AMSL_2nd order	105	59 s	0.183	63.0	0.191	57.7	10.9

Next, the magnetic flux density above the aluminum plate is measured separately along the X axis and Z-axis, as defined in Figure 4.16 (a), and the values are compared in Figure 4.17. They have a good agreement along the Z axis among these methods, but the AMSL_2nd order method and FEM with swept perform better than TBC along the X axis.

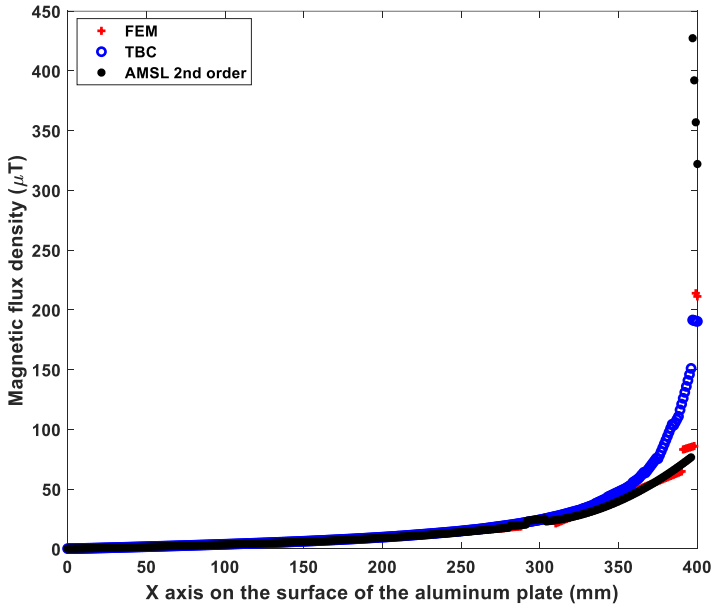

(a) X axis on the surface

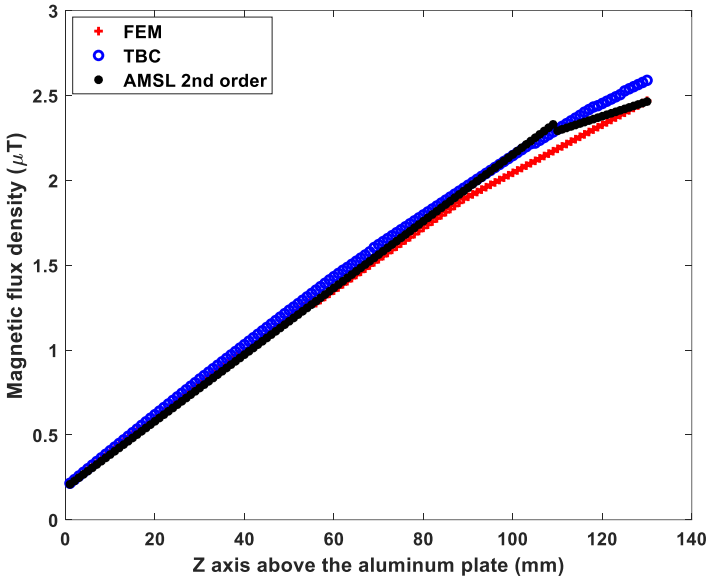

(b) Z axis from the surface

Figure 4.17 Magnetic flux density norm on the aluminum plate surface

So, the AMSL_2nd order method is a very powerful and accurate way to model the aluminum plate, and it will be used in the following process.

4.2.2.2 Fast shielding optimization of a RIPT system

Before doing the optimization on the aluminum plate, the dimensions of the transmitter and the receiver can be changed according to the design guidelines suggesting that the width of a coil should be three times the air gap between the transmitter and the receiver [94, 177-178]. The air gap defined for the RIPT system is 150 mm, based on which the external coil width w_c is selected to be 450 mm. Accordingly, for a total coil area of $468 \times 468\ \mathrm{mm}^2$ built and studied in the GeePs laboratory, the coil dimensions ($l_c \times w_c$) are changed to be $486 \times 450\ \mathrm{mm}^2$ so that it is useful when the EVs move along the length of the coil during the charging process, and it leads to an improved magnetic coupling. At the same time, the arrangement of wires in the coils has been changed from two layers to one layer for ease of practical installation, as shown in Figure 4.18 (a). So, the coil thickness d_c is changed to $5\ \mathrm{mm}$, equal to the diameter of the wire. The other dimensions of the system are kept the same as defined in Table 4.7.

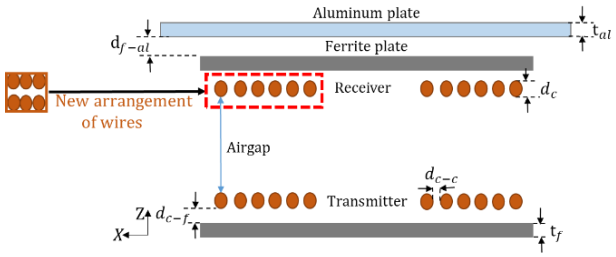

(a)

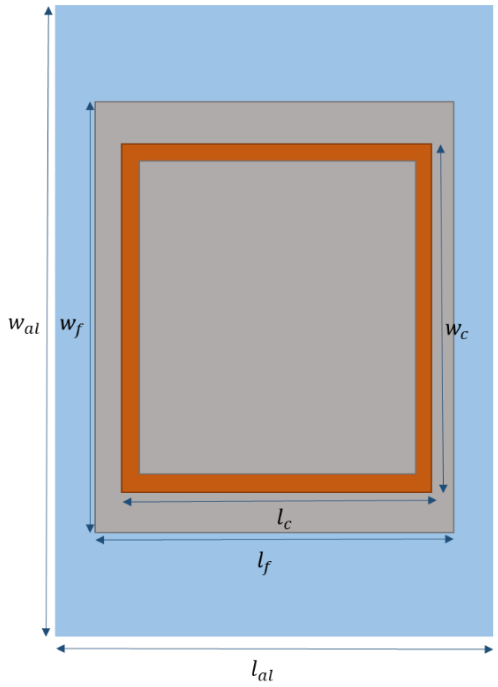

(b)

Figure 4.18 Dimensions of the RIPT system: (a) new arrangement of the wires of the coils (orange); (b) new geometry of the system

Then, the ferrite plates, which are the conventional magnetic shielding, and the aluminum plate that works as the conductive shielding, can be collectively referred to form the shielding. Taking into account the transmission efficiency and the cost of the system, the dimensions of the shielding should be carefully designed based on the predefined size of the transmitter and the receiver. Given the geometry and the ranges of possible geometrical dimensions of the shielding, the design can be achieved by working on the following eight design variables $\boldsymbol{x}$ with their range of values in Table 4.10:

Table 4.10 Range of the design variables $\boldsymbol{x}$

Parameter	Min [mm]	Max [mm]
d_{c-c}	1	5
w_f	536	974
l_f	495	900
d_{c-f}	1	10
t_f	1	10
w_{al}	590	1072
l_{al}	545	990
d_{f-al}	1	20

Firstly, the PCE metamodel M^{PCE} for the mutual inductance is constructed based on 400 training samples with the degree 15, and the hyperbolic scheme in Equation (3-10) is set as 0.45 to reduce the size of the polynomial basis. In order to verify the accuracy of the PCE metamodel, another 136 test samples are used to do the validation, and the validation error is 2.6×10^{-3}. Then, due to the

sensitivity analysis of this sparse PCE metamodel, Figure 4.19 reveals that the length and the width of ferrite have more influence on the mutual inductance M compared to other design variables, so in order to get more mutual inductance, the ferrite should be much longer and much wider.

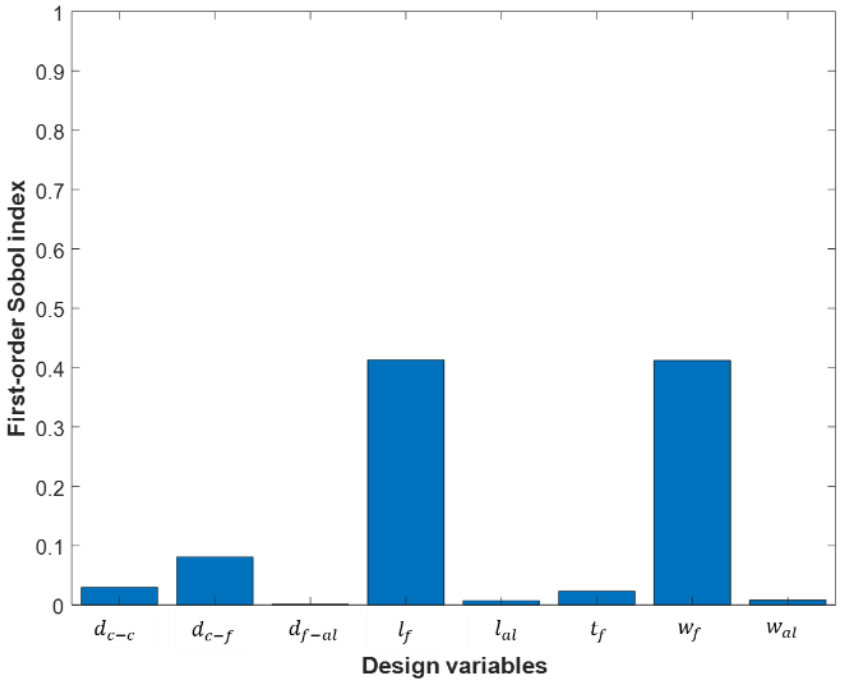

Figure 4.19 First-order Sobol index of the PCE metamodel M^{PCE} for the mutual inductance

Next, for the multiobjective optimization process, the objective functions are: the mutual inductance metamodel $M^{PCE}(\boldsymbol{x})$ with design variables $\boldsymbol{x}$, and the cost C of the shielding. They are described in the following equations:

$$\begin{aligned} M &= M^{PCE}(\boldsymbol{x}): \text{To find the maximum mutual inductance} \\ C &= l_f \times w_f \times t_f \times c_f + l_{al} \times w_{al} \times c_{al}: \text{To find the minimum the shielding cost} \end{aligned} \tag{4-1}$$

where l_f, w_f, t_f are the dimensions of the ferrite plate, l_{al} and w_{al} are the dimensions of the aluminum plate; c_f and c_{al} are the cost coefficients of ferrite and aluminum, respectively, shown in Table 4.11 [92].

Table 4.11 Cost coefficients of ferrite and aluminum [92]

Symbol	Quantity	Value [Unit]
c_f	Ferrite price	0.18 [\$/cm^3]
c_{al}	Aluminum price	333.68 [\$/m^2]

In order to better choose the optimization algorithm for the shielding design, two population-based optimization algorithms have been selected and compared: NSGA-II [122, 169] and MOPSO [123, 179]. The flowchart of NSGA-II is presented in Figure 4.2, and the flowchart of MOPSO is shown in Figure 4.20.

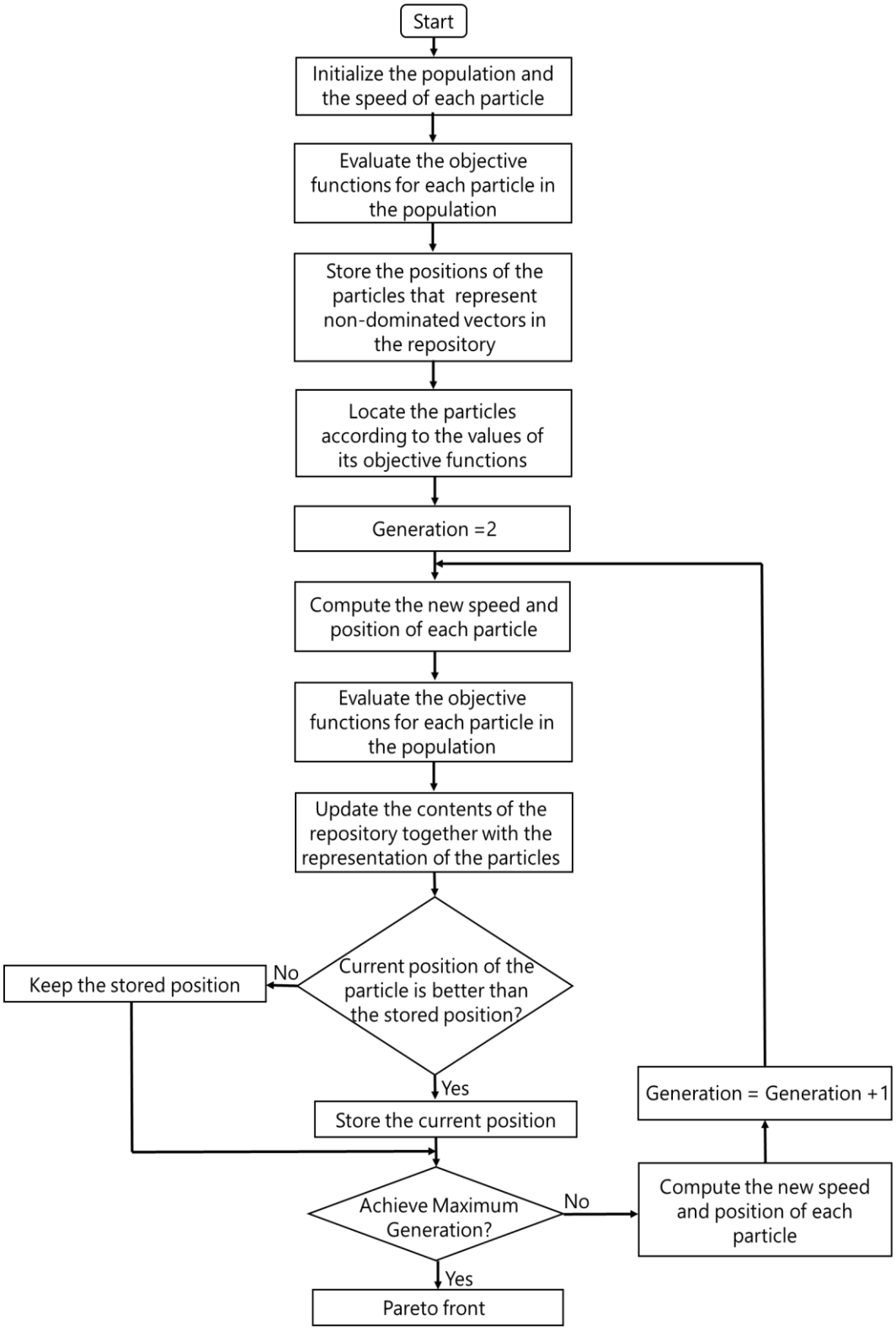

Figure 4.20 Flowcharts of MOPSO [123, 179]

The optimization settings of these algorithms are listed in Table 4.12.

Table 4.12 Optimization Settings

Parameter	NSGA-II	Parameter	MOPSO
Population size	400	Population size	400
		Repository size	200
Maximum generation	150	Maximum generation	150
Crossover probability	0.8	Inertia weight	0.5
Mutation probability	0.2	Personal & Global learning coefficients	2

During the optimization process, some practical constraints are taken into account to maximize the mutual inductance with the least cost of the shielding and limit the analysis to only feasible designs. The scheme to handle these constraints in the optimization process is that whenever two individuals (particles) are compared: if both are feasible, non dominance is directly applied to decide who is the selected one; if one is feasible and the other is infeasible, the feasible dominates; if both are in feasible, then the one with the lowest amount of constraint violation dominates the other (see references [122-123]).

Here, the first constraint shown in (4-2) is: that the size of the aluminum should be bigger than the size of the ferrite. In fact, an aluminum plate of the same size as the ferrite plate cannot shield the uncovered area's magnetic field on the surface of the chassis and lead to eddy current loss on the surface of the chassis [171]:

$$l_f < l_{al}, w_f < w_{al} \tag{4-2}$$

The other constraint is that the magnetic flux density leakage B_{max} at the point which is 800 mm far from the center of the air gap should be smaller than 27 μT (RMS value) defined by ICNIRP guidelines [45], as Figure 4.21 shows.

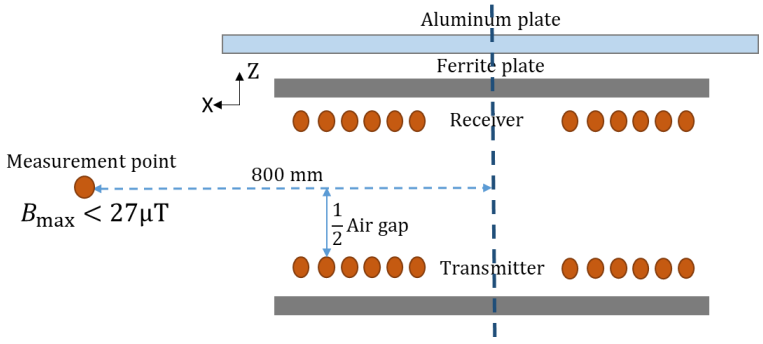

Figure 4.21 Measurement point of the magnetic flux density leakage

Here, Figure 4.22 shows that the Pareto front between the cost of the shielding and 1/Mutual inductance, and the mutual inductance increases with the cost of the shielding. Through the comparison of the solutions from NSGA-II and MOPSO, MOPSO can find a larger set of feasible solutions than NSGA-II. In order to simultaneously reach the maximum mutual inductance and

achieve the minimum cost of the shielding in the defined ranges of design variables, the magenta value from NSGA-II and the green value from MOPSO are chosen as the optimal results.

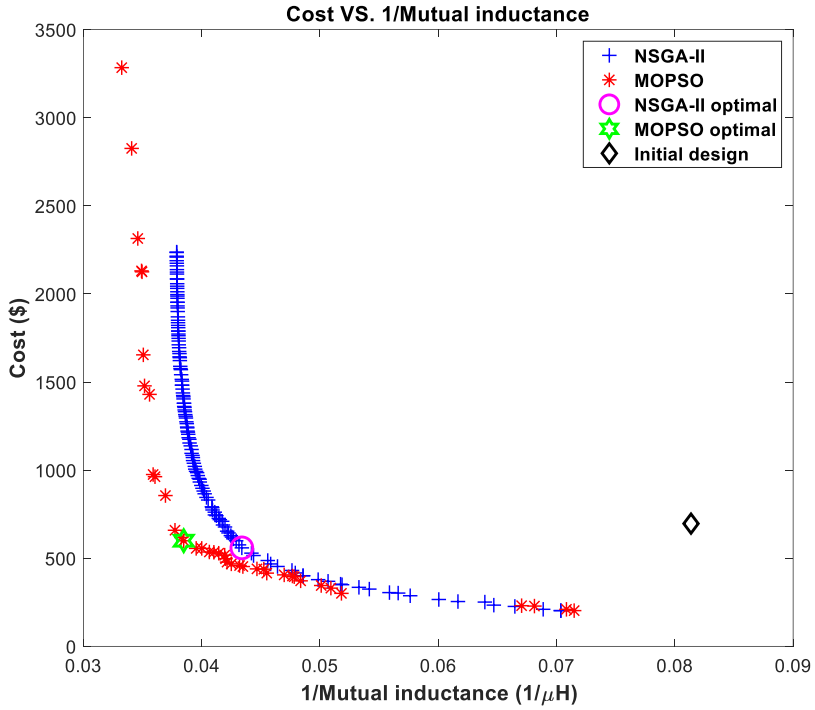

Figure 4.22 Cost VS. 1/Mutual inductance

The comparison results among the initial results (from Figure 4.16), the optimization results from NSGA-II and MOPSO are listed in Table 4.13. MOPSO combined with the PCE metamodeling technique can use less optimization time and find a bigger mutual inductance and smaller cost of the shielding than NSGA-II with PCE metamodeling. So, MOPSO combined with the PCE metamodeling method is an adequate choice for designing the shielding in the studied RIPT system.

Table 4.13 Comparison between the optimization results and the initial result

Parameter	Initial	NSGA-II	MOPSO	Parameter	Initial	NSGA-II	MOPSO
d_{c-c} $[mm]$	0.3	1.5	1	d_{f-sh} $[mm]$	5	8.4	20
w_f $[mm]$	600	793	940	L_1 $[\mu H]$	59.56	75.82	80.44
l_f $[mm]$	500	752	832	L_2 $[\mu H]$	55.95	75.56	80.28
d_{c-f} $[mm]$	8	1.8	1.1	M $[\mu H]$	12.29	22.80	25.05
t_f $[mm]$	2	1.4	1	Cost [$]	696.5	558.8	599.6
w_{al} $[mm]$	1800	917	1036	B_{max} $[\mu T]$	7.31	7.76	8.57
l_{al} $[mm]$	800	844	920	Optimization Time [s]	/	886.5	714.3

Compared with the initial design, the optimization results of MOPSO improved approximately 104 % the mutual inductance M, and saved 14 % of the cost C for the shielding. Considering the

constraints, the magnetic flux density leakage B_{max} is 1.2 times higher than the initial value, but it still meets the ICNIRP guidelines.

So, it comes out that combining a metamodel on the PCE method with MOPSO can be proposed as an appropriate approach to take into account the geometric parameters defining the ferrite and aluminum shielding, thus improving the mutual inductance and reducing the cost of the RIPT system under the ICNIRP guidelines.

4.3 Topology optimization on the ferrite plate

In a classical approach, the dimensions of the ferrite and aluminum shielding can be easily selected by parametric optimization. However, it is limited to how to properly arrange the ferrite part in the specified size. So, in order to solve this problem, TO is used in this section to find a ferrite distribution that maximizes the mutual inductance M, while constraining the volume of the ferrite plate, obtaining a light design for the RIPT system. Although there are several TO methods in the literature, the SIMP method, which is today the most commonly used due to its easy and intuitive implementation, is adopted to arrange the ferrite distribution [110].

4.3.1 Introduction to SIMP-based topology optimization

The SIMP method discretizes a studied domain Ω into numerous fine elements, for which artificial density values are introduced as design variables ρ_i, as illustrated in Figure 4.23. ρ_i is the material density in the i^{th} element. The artificial density value of ρ_i lying between 0 and 1 represents a proportion of solid material or void. It is desired to have either solid material ($\rho_i = 1$), or void ($\rho_i = 0$) as the final material in the element instead of having intermediates (unless they are materials that existed in the COMSOL material library). The material properties between the solid and void are interpolated with a smooth continuous function which depends on the material density ρ_i.

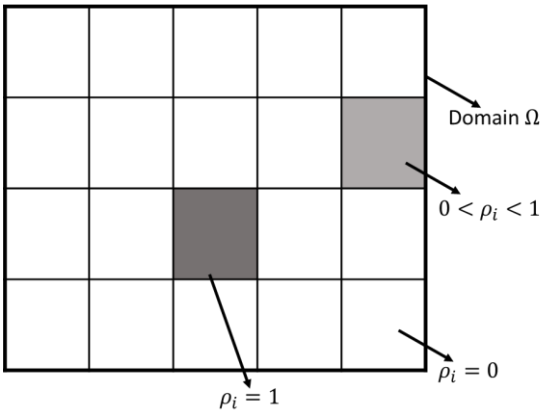

Figure 4.23 Domain Ω with SIMP method

Then, as it is desired here to optimize the topology of ferromagnetic materials, the adequate choice is to consider only permeability as the material property. So, the function of the ferrite's relative permeability μ_r is achieved in the following equation [111, 180-181]:

$$\mu_{r_i} = \mu_{r0} + (\mu_r - \mu_{r0})\rho_i^n \tag{4-3}$$

where μ_r is the relative permeability of ferrite, equal to 3000; μ_{r0} is the relative permeability of air, equal to 1, and $0 \leq \rho_i \leq 1$. The penalization coefficient n, (usually set between 2 and 5) is used to change the interpolation behavior with $n \geq 1$, and it works on the design variable ρ_i. The gradient-based optimization solver defined in COMSOL is used to solve the variable, and each variable is allowed to take the relative permeability of either ferrite (μ_r) or air (μ_{r0}) so as to maximize the objective function [180,182]. Figure 4.24 (a) shows the initial domain to be optimized, where each discretization represents a variable of the problem, and the color legend for the materials, with the corresponding ρ and μ_r. The TO result should be composed of ferrite and air, as shown in Figure 4.24 (b).

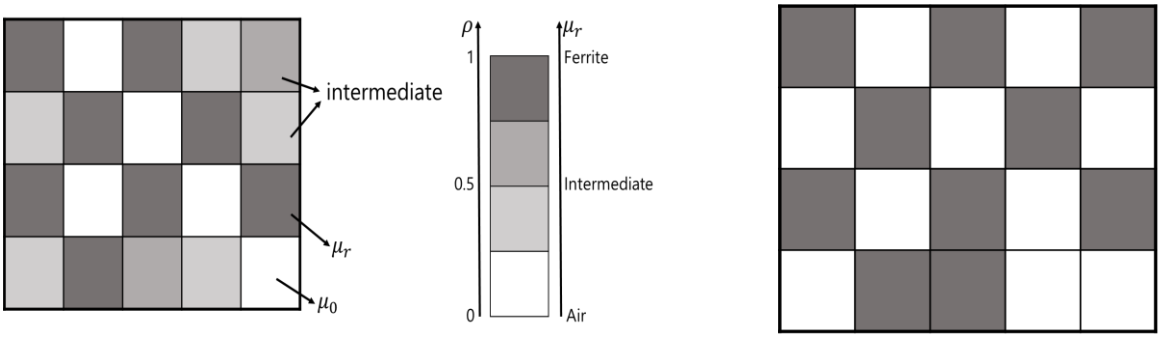

(a) TO process on SIMP method (b) TO result

Figure 4.24 Ferrite placement with TO on SIMP method

In this section, the objective function of the ferrite placement optimization is to minimize the ratio $\frac{M_{initial\ ferrite\ domain}}{M_{\mu r_i\ optimized\ ferrite\ domain}}$ under the defined ferrite volume constraint. The optimization process is based on the assumption that the ferrite is not in the saturation state [110-111, 181].

The process for the TO on the ferrite placement includes the following steps:

1) Define the design domain and the function of the ferrite's relative permeability;

2) Optimize the ferrite's relative permeability distribution through SIMP method with COMSOL optimization module;

3) Obtain the optimized ferrite structure and get the mutual inductance M with the optimized ferrite structure;

The constraint of ferrite volume can be defined manually, but the optimization of the ferrite placement aims at minimizing the reduction in the value of the mutual inductance M compared to M with the initial domain. The TO result allows some ferrite parts to be removed. And the penalization coefficient n is set to 4, which is suggested by some authors in order to produce no intermediate values [180,182].

4.3.2 Topology optimization applied to the ferrite plate

The ferrite structure is discussed in two situations: without an aluminum plate above the receiver and with an aluminum plate above the receiver. The TO process works with the optimization module [181] from COMSOL 5.6 on an Intel Xeon W-2125 processor.

4.3.2.1 Without an aluminum plate

The dimensions of ferrite plates are from the multiobjective optimization results of section 4.2.1.2. Then, in order to further save ferrite volume and keep nearly the same mutual inductance, TO with SIMP method is used to find a good arrangement of ferrite. The previously optimal dimension of the ferrite plate from Section 4.2.1.2 and the ferrite structure under different volume constraints are shown separately in Figure 4.25.

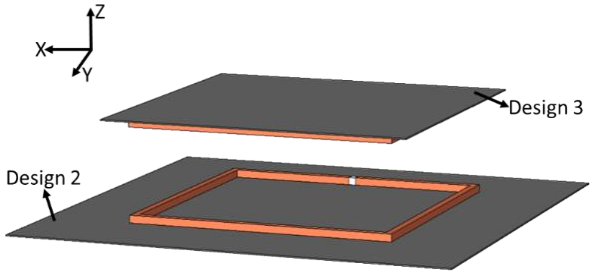

(a) Initial ferrite volume from Section 4.2.1.2

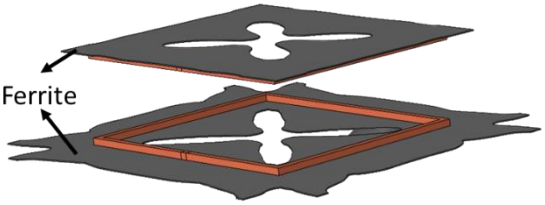

(b) Structure from TO under 70% of the ferrite volume

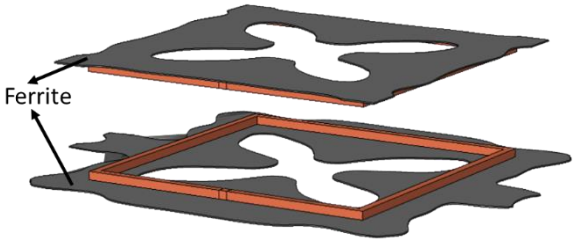

(c) Structure from TO under 50% of the ferrite volume

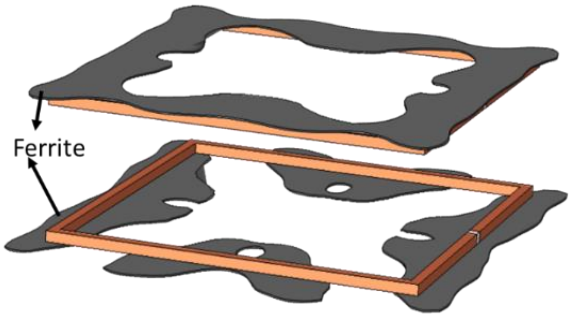

(d) Structure from TO under 30% of the ferrite volume

Figure 4.25 Ferrite placement without an aluminum plate

However, the ferrite placement also has an impact on the ferrite core loss. The ferrite core loss can be calculated with the equation (4-4) [182]:

$$W_{ferrite\ core\ loss} = \iiint_0^{V_{ferrite}} q\ dv \tag{4-4}$$

where q represents the volumetric loss density, v is the volumetric element of the ferrite.

The relationship among the ferrite volume, the mutual inductance, and the ferrite core loss is shown in Figure 4.26.

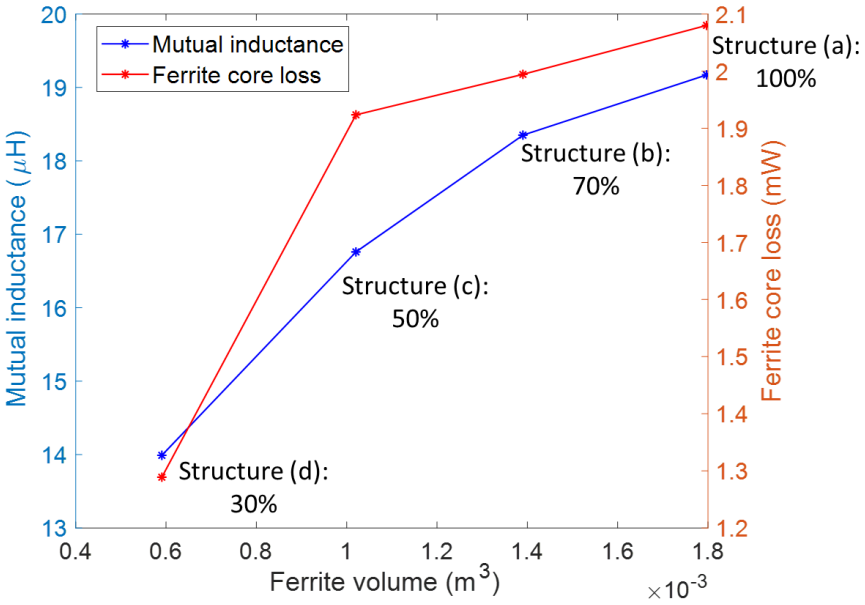

Figure 4.26 Relationship among ferrite volume, mutual inductance, and ferrite core loss

Then, it can be observed that during TO process, removing a part of the ferrite from the center and the edges of the ferrite plates are recommended, no matter the constraint of the ferrite volume ratio. Arranging the ferrite plates with this tip can facilitate a 40% reduction of the ferrite volume and decrease 5% of the ferrite core loss. Moreover, it also has an approximate 10% reduction in the mutual inductance.

4.3.2.2 Influence of an aluminum plate

Even if there is an aluminum plate above the receiver, TO with the SIMP method is also used to find a good arrangement of ferrite for saving ferrite volume and keeping nearly the same mutual inductance. The previously optimal dimension of the ferrite plate from Section 4.2.2.2 and the ferrite structure under different volume constraints are presented separately in Figure 4.27. It shows that during TO process, a part of the ferrite from the center and the edges of the ferrite plates should be removed no matter the constraint of the ferrite volume ratio. However, due to the effect of the aluminum plate, the ferrite on the receiver side has to be larger than that on the transmitter side through TO with the SIMP method.

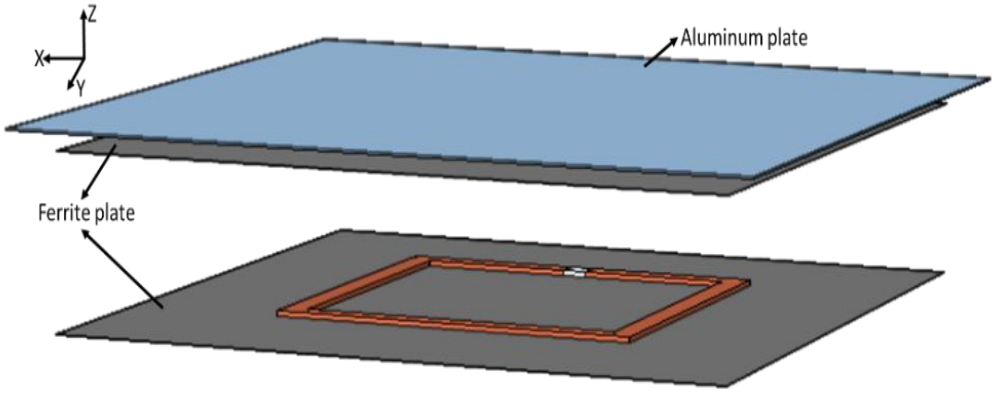

(a) Ferrite volume from Section 4.2.2.2

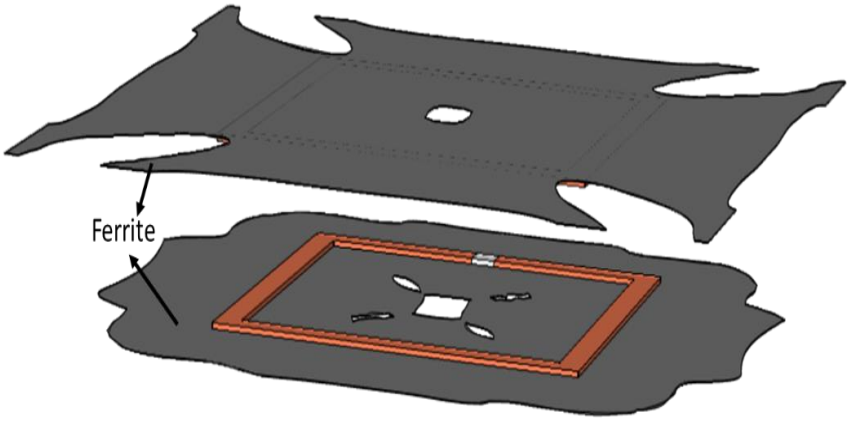

(b) Structure from TO under 70% of ferrite volume (the aluminum plate is hidden)

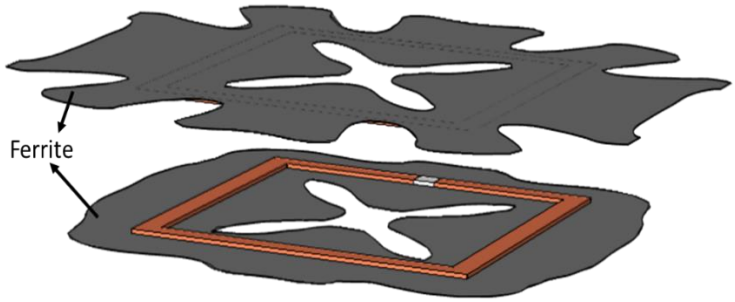

(c) Structure from TO under 50% of ferrite volume (the aluminum plate is hidden)

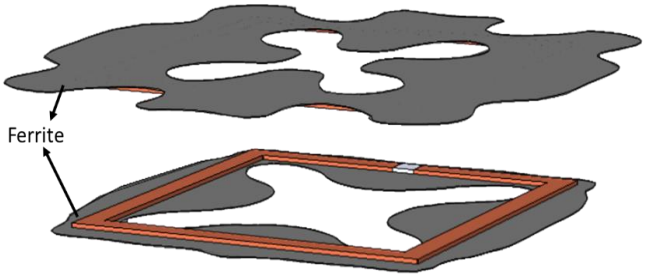

(d) Structure from TO under 30% of ferrite volume (the aluminum plate is hidden)

Figure 4.27 Ferrite placement with an aluminum plate

Then, the relationship among the ferrite volume, the mutual inductance, and the ferrite core loss is summarized in Figure 4.28.

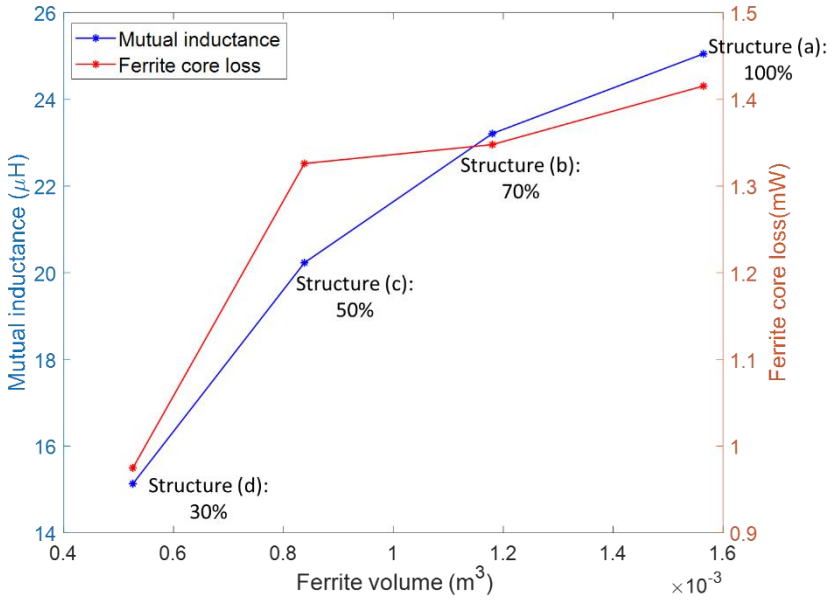

Figure 4.28 Relationship among ferrite volume, mutual inductance, and ferrite core loss

Compared to Ferrite structure (a), Ferrite structure (d) saves almost 30% of ferrite, and the ferrite core loss reduces by about 5%, but the mutual inductance decreases by around 10%.

4.3.2.3 Discussion

TO, with the SIMP method, can be used to arrange the ferrite placement. A part of the ferrite from the center and the edges of the ferrite design domain can be removed to decrease the volume and keep the minimal reduction of the mutual inductance (calculated with the initial ferrite design domain) when the transmitter and the receiver are aligned. However, the results from TO are influenced by the aluminum plate near the ferrite design domain. With the existence of the aluminum plate, the ferrite on the receiver side has to be larger than that on the transmitter side through TO with the SIMP method. These results give some guideline for arranging the ferrite configuration. If the structures from TO are taken into account to use, they have to be further simplified because the TO results cannot be easily manufactured in reality. Then, there are some features that can be indicated how ferrite should be placed in a manufactural form [110]:

- The optimized structures of the ferrite are similar but not entirely symmetrical plates. This is due to the optimization randomness. In practice, the placement of the ferrite should be symmetrical, as the coils are rectangular. Therefore, the ferrite should be simplified as symmetrical.

- The appearance of curves is inevitable in ferrite topology optimization. Therefore, curves will be approximated by straight lines for simplification and operability.

4.4 Conclusion

This chapter has highlighted the approach to design the RIPT system:

- Using a parametric multiobjective optimization based on the PCE metamodeling technique;

- TO with the SIMP method for arranging the ferrite placement on the given design domain.

Section 4.2 proposes the method to apply the multiobjective optimization with the PCE metamodeling technique into the RIPT system without shielding and the case with shielding. It may save several times the computational time (including the time to calculate the training samples) compared to 3D FEM computations with the multiobjective optimization in this chapter. Furthermore, two popular optimization algorithms: NSGA-II and MOPSO are compared to find the most efficient one for combining with the PCE metamodeling technique. Then, it comes out that utilizing a metamodel on the PCE method with MOPSO is proposed to take into account the geometric parameters defining the ferrite and aluminum shielding, thus improving the mutual inductance and reducing the cost of the RIPT system under the ICNIRP guidelines.

In Section 4.3, TO with the SIMP method is used to arrange the ferrite placement on the previously optimal dimensions of the ferrite. By discussing the ferrite structures on the RIPT system without an aluminum plate and with an aluminum plate, it is found that a part of the ferrite from the center and the edges of the predefined ferrite plate can be removed to save the ferrite volume and achieve the minimal reduction of the mutual inductance value. Moreover, the results from TO are influenced by the aluminum plate near the ferrite design domain, and the ferrite on the receiver side has to be bigger than the one on the transmitter side. These results give some guidelines for arranging the ferrite placement.

The multiobjective optimization with the PCE metamodeling technique can accelerate the parameter optimization of the RIPT system, and then the obtained ferrite dimension can be used to define the design area for TO. TO gives the guideline to arrange the ferrite on the prefixed size.

Conclusion and Perspectives

Conclusion

In this thesis, the conclusions can be summarized in the following parts:

1) How the ratio between the wire length and the mutual inductance influences the maximum transmission efficiency is analyzed when the transmitter and the receiver are identical. If the wire length is fixed, the mutual inductance has the most effect on the transmission efficiency. Then, a comparison of different shapes of couplers (circular, square, DD, and BP) is shown by using the 3D COMSOL simulation tool and the experimental results on 1:10 scale prototypes made in the laboratory. For maximum transmission efficiency in RIPT systems, the circular coupler can provide the maximum values among these couplers, but the square coupler has a higher tolerance to misalignment than others; meanwhile, the square coupler has more magnetic flux density leakage above the receiver. However, the square coupler is chosen instead of the circular one as it is easier to manufacture and is more suitable in the case of dynamic RIPT.
2) To take into account the sources of uncertainty (the misalignment along the X/Y axis, the variation in the airgap, or the rotation on the receiver), various metamodels (SVR, MGPA, and sparse PCE) were built and compared for analyzing the mutual inductance on the small scale square couplers. Due to the tradeoff between the computational time and the accuracy of the metamodel, the sparse PCE was chosen to analyze the mutual inductance for different shapes of couplers. It was proved that the sparse PCE was a very useful tool in the analysis of the RIPT system in order to save significant computational time. Then, according to the sensitivity analysis established on the coefficients of sparse PCE metamodels, the misalignment along the X axis (along the length of the coil) appeared to be the most influential factor in the mutual inductance for DD/BP couplers, whereas the misalignment along the X/Y axis (along the length/width of the coil) has the same effect as the circular and the square couplers, due to their symmetries. Considering the impact of the sources of uncertainty on the mutual inductance, the ratio between the wire length and the mutual inductance may be helpful in designing the shape of the coils in view of the maximum transmission efficiency. Circular couplers should be recommended for the static RIPT system due to their higher value of the maximum transmission efficiency (compared to other couplers), taking into account the given sources of uncertainty.
3) The sparse PCE metamodeling technique is proposed with optimization methods for assessing the efficiency of RIPT systems and satisfying EMC constraints around EVs. The proposed methodology simultaneously includes various aspects of the electromagnetic problem: geometrical dimensions of the system and placement of the materials. Compared to 3D FEM with multiobjective optimization methods, it may save several times the computational time (including the time to calculate the training samples). At the same time, it also saves at least two times computational resources (the price of the Intel Xeon W-2125 processor is higher than the Intel(R) Core i5-8365U processor). The sparse PCE metamodels describe the mutual inductance dependence with the design variables, and

the optimization algorithms perform the optimization for the system under perfect alignment conditions. Two traditional optimization algorithms: NSGA-II and MOPSO are compared, and it comes out that associating a metamodel on the PCE method with MOPSO uses a shorter computational time, and it can find a larger set of feasible solutions than that with NSGA-II. What's more, TO with the SIMP method can arrange the ferrite placement in the studied area in order to save the ferrite volume and achieve the minimal reduction of the mutual inductance. But if the structures issued from TO are taken into account to use, they have to be further simplified because the TO results cannot be easily manufactured in reality.

Perspectives

Our works mainly concentrate on the design and optimization of the RIPT system for satisfying EMC constraints around EVs. Even though we've been working on the above questions for about three years, there is still a long way to go on further. From my point of view, future research is suggested in the following aspects:

1) More design variables (such as materials properties, and turns of the wires) in the magnetic and thermal coupled field analysis should be taken into account during the design process of the sparse PCE metamodel combined with MOPSO method. Because when the RIPT system works for a long time, the heating of the magnetic coupler brings adverse effects on the stability of the system.
2) The magnetic flux density leakage around the coupler should be combined into TO process for arranging the ferrite placement in the studied area because the magnetic flux density leakage is limited by the ICNIRP guidelines, and the ferrite works as a guide of the magnetic flux density in the RIPT system.
3) For the study of MGPA algorithms, the MGPA metamodel is picked out in terms of high coefficient of determination and low model complexity, but the coefficient of determination is not an adequate measurement to evaluate the accuracy of nonlinear models [183-185]. Therefore, some other criteria would be added in the process to evaluate the accuracy of the MGPA metamodel.
4) The experimental validation of the optimal results should be done to show that such an optimization approach could be efficiently used for various RIPT systems.
5) Hybrid couplers combining the RIPT and capacitive WPT for dynamic charging may be designed to decrease the cost of the system and achieve the SAE J2954 standards because the hybrid couplers have the potential to improve transmission efficiency and reduce the compensation components [49, 186-187].

Appendix

Appendix A

Maximum transmission efficiency on series-series compensation topology

Here, the SS compensation is taken into account to analyze the power transmission efficiency of the IPT system shown in Figure A.1. I_1, I_2 are the current in the transmitter and the receiver; R_{L} is the load resistance; R_1,R_2 represent the resistances of the transmitter and the receiver; C_1 and C_2 are the capacitors of the transmitter and the receiver; L_1, L_2 represent the self-inductances of the transmitter and the receiver; M is the mutual inductance between the transmitter and the receiver.

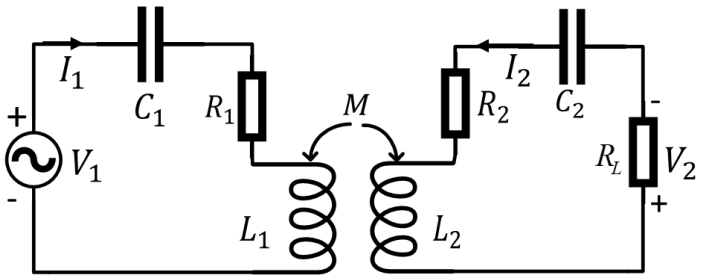

Figure A.1 Equivalent electrical circuit in the SS compensation topology

According to Kirchhoff's voltage law, the equations for the output voltage V_2 are shown in Equation (A-1):

$$\begin{gathered} 0 = jwL_2I_2 + jwMI_1 + \frac{1}{jwC_2}I_2 + R_2I_2 + V_2 \\ V_2 = I_2R_L \end{gathered} \tag{A-1}$$

where w is the angular frequency.

Thus, the ratio between the currents I_1 and I_2 can be calculated from Equation (A-1):

$$\frac{I_1}{I_2} = -\frac{R_2+R_L+j\left(wL_2-\frac{1}{wC_2}\right)}{jwM} \tag{A-2}$$

So, the equation to calculate the transmission efficiency η can be achieved by replacing I_1 with $-\frac{R_2+R_L+j\left(wL_2-\frac{1}{wC_2}\right)}{jwM}I_2$:

$$\eta = \frac{P_2}{P_1} = \frac{P_2}{P_{R_1}+P_{R_2}+P_2} = \frac{Re\{I_2I_2^*\cdot R_L\}}{Re\{I_1I_1^*\cdot R_1\}+Re\{I_2I_2^*\cdot R_2\}+Re\{I_2I_2^*\cdot R_L\}} = \frac{(wM)^2R_L}{\left\{(R_2+R_L)^2+\left(wL_2-\frac{1}{wC_2}\right)^2\right\}R_1+(wM)^2R_2+(wM)^2R_L} \tag{A-3}$$

where P_1 is the input power; P_2 is the power consumed by the load; P_{R_1}, P_{R_2} are the power losses in the transmitter and the receiver.

Equation (A-3) shows that the capacitor on the primary side has no effect on the efficiency, as it does not contain C_1. Instead, the value of C_2 impacts efficiency. Furthermore, considering the resonance conditions, the resonant angular frequency w_0 is equal on the transmitter and receiver sides:

$$w_0 = w = \sqrt{\frac{1}{L_1 C_1}} = \sqrt{\frac{1}{L_2 C_2}} \tag{A-4}$$

the equation for the efficiency becomes:

$$\eta = \frac{(w_0 M)^2 R_L}{(R_2+R_L)^2 R_1 + (w_0 M)^2 R_2 + (w_0 M)^2 R_L} \tag{A-5}$$

For the maximum transmission efficiency η_{max}, the load R_{Lopt} is obtained from Equations (A-4) and (A-5).

$$\frac{\partial \eta}{\partial R_{\mathrm{L}}} = 0 \tag{A-6}$$

$$\frac{\partial \eta}{\partial R_{\mathrm{L}}} = \frac{(w_0 M)^2[(R_2 + R_L)^2 R_1 + (w_0 M)^2 R_2 + (w_0 M)^2 R_L] - (w_0 M)^2 R_L[2R_1(R_2 + R_L) + (w_0 M)^2]}{[(R_2 + R_L)^2 R_1 + (w_0 M)^2 R_2 + (w_0 M)^2 R_L]^2}$$

$$= \frac{(w_0 M)^2 R_1 R_2^2 - R_1 R_L^2 (w_0 M)^2 + (w_0 M)^4 R_2}{[(R_2 + R_L)^2 R_1 + (w_0 M)^2 R_2 + (w_0 M)^2 R_L]^2} = 0$$

$$R_{\mathrm{Lopt}} = \sqrt{R_2^2 + (w_0 M)^2 \frac{R_2}{R_1}} \tag{A-7}$$

Then, Equation (A-8) gives the maximum transmission efficiency under the resonance conditions and the optimal load.

$$\eta_{max} = \frac{(w_0 M)^2}{(\sqrt{R_1 R_2} + \sqrt{R_1 R_2 + (w_0 M)^2})^2} \tag{A-8}$$

The coupling coefficient k is defined by the ratio of the mutual inductance M (between the transmitter and the receiver) and the geometric mean of the two self-inductances $L_1 \mathrm{and}\ L_2$:

$$k = \frac{M}{\sqrt{L_1 L_2}} \tag{A-9}$$

The transmitter and the receiver coil quality factors at the resonant angular frequency w_0 are defined as:

$$Q_i = \frac{w_0 L_i}{R_i} \tag{A-10}$$

where $i = 1,2$ stands for the transmitter and the receiver respectively. Moreover, the system quality factor Q is defined as the geometric mean of the quality factors Q_1 and Q_2 of the two coils.

$$Q = \sqrt{Q_1 Q_2} = w_0 \sqrt{\frac{L_1 L_2}{R_1 R_2}} \tag{A-11}$$

The product of the coupling coefficient k and the system quality factor Q is equal to

$$kQ = \frac{M}{\sqrt{L_1 L_2}} \times w_0 \sqrt{\frac{L_1 L_2}{R_1 R_2}} = \frac{w_0 M}{\sqrt{R_1 R_2}} \tag{A-12}$$

Then, the maximum transmission efficiency η_{max} can be written below

$$\eta_{max} = \frac{(w_0 M)^2}{\left(\sqrt{R_1 R_2} + \sqrt{R_1 R_2 + (w_0 M)^2}\right)^2} = \frac{(w_0 M)^2}{2R_1 R_2 + 2\sqrt{(R_1 R_2)^2 + R_1 R_2 (w_0 M)^2} + (w_0 M)^2} =$$
$$\frac{(kQ)^2 R_1 R_2}{2R_1 R_2 + 2\sqrt{(R_1 R_2)^2 + (R_1 R_2)^2 (kQ)^2} + (kQ)^2 R_1 R_2} = \frac{(kQ)^2}{2 + 2\sqrt{1 + (kQ)^2} + (kQ)^2} = \frac{(kQ)^2}{(1 + \sqrt{1 + (kQ)^2})^2} \tag{A-13}$$

Therefore, the maximum transmission efficiency η_{max} achieves the maximum value:

$$\eta_{max} = \frac{(kQ)^2}{\left(1 + \sqrt{1 + (kQ)^2}\right)^2} = \left(\frac{kQ}{1 + \sqrt{1 + (kQ)^2}}\right)^2 = \left(\frac{kQ\left(1 - \sqrt{1 + (kQ)^2}\right)}{\left(1 + \sqrt{1 + (kQ)^2}\right)\left(1 - \sqrt{1 + (kQ)^2}\right)}\right)^2$$

$$= \left(\frac{kQ\left(1 - \sqrt{1 + (kQ)^2}\right)}{(1 - 1 - (kQ)^2)}\right)^2 = \left(\frac{1 - \sqrt{1 + (kQ)^2}}{kQ}\right)^2 = \frac{1 - 2\sqrt{1 + (kQ)^2} + 1 + (kQ)^2}{(kQ)^2}$$

$$= 1 - 2\frac{\sqrt{1 + (kQ)^2} - 1}{(kQ)^2} = 1 - 2\frac{\left(\sqrt{1 + (kQ)^2} - 1\right)\left(\sqrt{1 + (kQ)^2} + 1\right)}{(kQ)^2\left(\sqrt{1 + (kQ)^2} + 1\right)}$$

$$= 1 - \frac{2}{1 + \sqrt{1 + (kQ)^2}} \approx 1 - \frac{2}{kQ} \tag{A-14}$$

under the condition $kQ \gg 2$.

Furthermore, when the transmitter and the receiver are identical, the maximum transmission efficiency η_{max} can also be expressed as below with Equation (A-12):

$$\eta_{max} \approx 1 - \frac{2}{kQ} = 1 - \frac{2\sqrt{R_1 R_2}}{w_0 M} = 1 - \frac{R_1}{\pi f_0 M} = 1 - \frac{\rho}{\pi f_0 S}\frac{l}{M} \tag{A-15}$$

where $w_0 = 2\pi f_0$, f_0 is the resonance frequency, l is the conducting wire length of a coil, S is the cross-sectional area of the conducting wires, ρ is the electrical resistivity of the wires.

Appendix B

Measurement of the electrical parameters of the coupler

The first measurement is the resistance R_1, self-inductance L_1 of the transmitter when the receiver is in the open circuit.

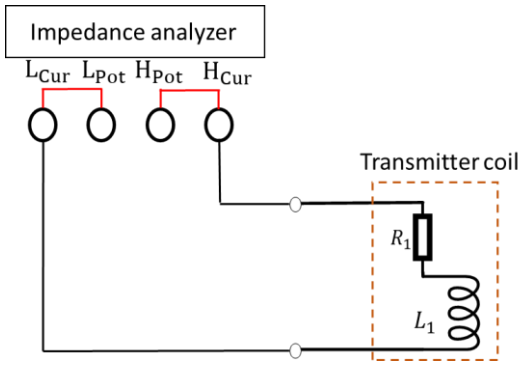

Figure B.1 Method to measure the self-inductance L_1

The second measurement is the resistance R_2, self-inductance L_2 of the receiver when the transmitter is in the open circuit.

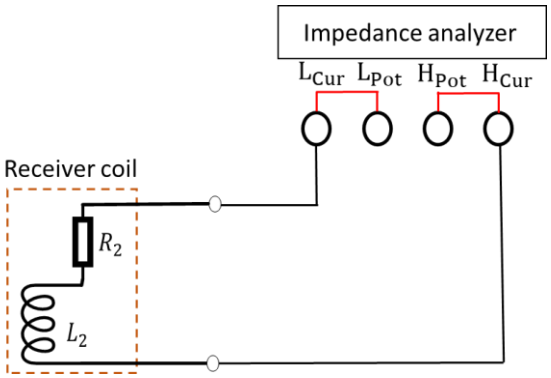

Figure B.2 Method to measure the self-inductance L_2

The third measurement is the mutual inductance M between the transmitter and the receiver. For measuring the mutual inductance, the impedance analyzer is set in a four-wire measurement configuration with two wires providing the current to the transmitter, the other two measuring the voltage of the receiver. The equations are as follows:

$$\begin{cases} v_1 = R_1 i_1 + j \times 2\pi f \times L_1 i_1 + jM \times 2\pi f \times i_2 \\ v_2 = R_2 i_2 + jL_2 \times 2\pi f \times i_2 + jM \times 2\pi f \times i_1 \rightarrow M = \frac{v_2}{j \times 2\pi f \times i_1} \\ i_2 = 0 \end{cases} \quad \text{(B-1)}$$

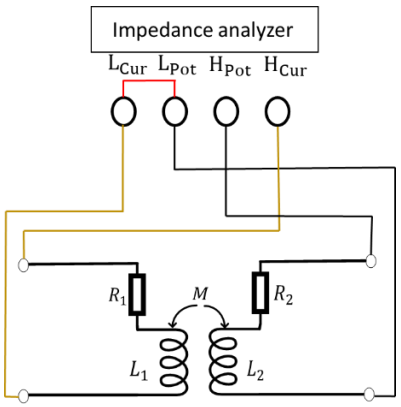

(a)

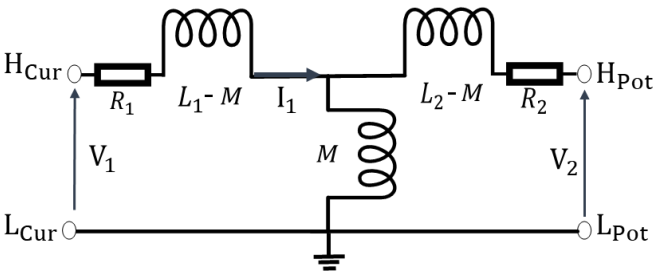

(b)

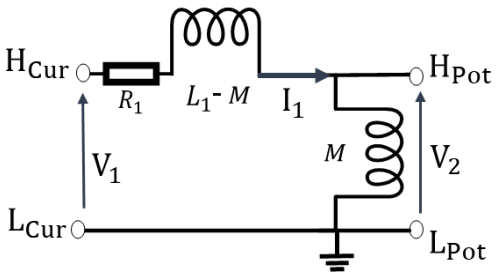

(c)

Figure B.3 Method to measure the mutual inductance M

Appendix C

Calibration of magnetic probes

The measurement of the magnetic field is generally based on the use of probes that are dedicated to capturing three components of the magnetic field separately. These probes are formed of a conductive loop that generates a voltage according to Faraday's law, once it intercepts a variable magnetic field. Figure C.1 below shows the PBS H3/H2 magnetic probe from AARONIA. PHS H3 with a diameter of 25 mm and PHS H2 with a diameter of 12 mm are used in the measurements of the magnetic field radiated by the wireless power transfer system.

Figure C.1 Magnetic probe PBS H3/H2

Here are some brief principles to operate these probes, as well as the different calibration techniques.

1) Theory and operation of the probes

The magnetic probes are made up of one or more turns and can have different shapes (circle, square…). The measuring principle of these probes is based on Faraday law: when a variable magnetic field passes through a closed circuit, the variation in flux"φ" causes an electromotive force "e" across the loop:

$$\mathrm{e} = -\mathrm{n}\frac{\partial \varphi}{\partial t} \tag{C-1}$$

where n represents the number of turns of the probe.

For a sinusoidal field, the equation can be transformed into a harmonic:

$$\mathrm{e(jw)} = -\mathrm{njw}\emptyset\mathrm{(jw)} \tag{C-2}$$

In order to measure different components of the field, it is necessary to place the loop in a way corresponding with the measured component, as the figure below shows.

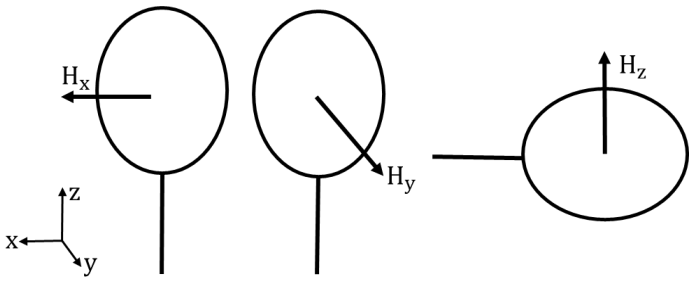

Figure C.2 Magnetic probes to measure different components

Considering that the magnetic induction B is perpendicular to the surface of the loop and is uniformly distributed on the surface s of the loop and that there is only one turn of the loop, the electromotive force is written in the following way:

$$e = -jwBs \tag{C-3}$$

2) Different technologies of calibration

There are different technologies to calibrate the magnetic probes, for example:

- Calibration by using a reference probe instead;
- Calibration by using electromagnetic fields acquired digitally;
- Calibration by analyzing known electromagnetic fields;

The last method is the one used in the research, and we are interested in calibrating using a circular conductor above a ground plane.

3) Performance factor

The performance factor (PF) coefficient characterizes the ability of the probe with its measurement chain to capture a component of the electromagnetic field. This coefficient is independent of the radiating structure and of the position of the probe above the radiation source but depends on the characteristics of the probe, the amplifier which is connected between the probe and the spectrum analyzer, and the frequency. This ratio takes into account the effect of the probe and the effect of the amplifier. Figure C.3 schematizes the measurement chain in the near-field bench.

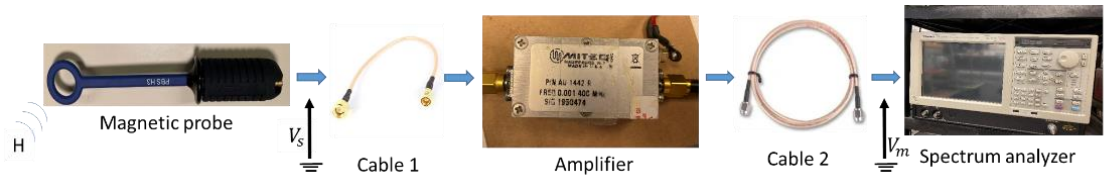

Figure C.3 Measurement chain for the performance factor

The voltage V_m measured by the spectrum analyzer (as shown in Figure C.4) is an image of the radiated H field, and the ratio related to the voltage measured by the spectrum analyzer and the magnetic field is the way to determine the PF in the frequency domain:

$$\mathrm{PF} = \frac{V_m(f)}{H(f)} \tag{C-4}$$

Therefore, the calibration of the measurement chain is equivalent to determining its performance factor as a function of frequency.

The voltage V_s induced by the probe is:

$$V_s(x,y,z,f) = A(f) * H(x,y,z,f) \qquad \forall(x,y,z,f) \tag{C-5}$$

where $A(f)$ is a function that depends for a given probe only on the frequency f of the measured magnetic field.

The relation between the magnetic field and the input voltage of the spectrum analyzer is

$$V_m(f) = G(f) * A_{cable}(f) * \mathrm{A}(f) * H_z(x,y,z,f) \tag{C-6}$$

where $A_{cable}(f)$ corresponds to the dielectric loss introduced by the coaxial cable and the connection between the probe and the measuring device; $G(f)$ is the transfer function of the amplifier (gain) (here the MITEQ AU-1442 type amplifier is used, and the gain is 35 dB).

In the case of a spectrum analyzer having a $50\,\Omega$ input impedance, there is a simple relationship between the voltage V_m and the power P_m provided to the analyzer:

$$P_m(x,y,z,f) = \frac{[V_m(x,y,z,f)]^2}{50} \tag{C-7}$$

$$P_m(x,y,z,f) = \frac{[G(f)*A_{cable}(f)*\mathrm{A}(f)*H_z(x,y,z,f)]^2}{50} * [H_z(x,y,z,f)]^2 \tag{C-8}$$

Hence in the logarithmic form:

$$\mathrm{PF(f)}|_{dBm.\frac{m}{A}} = P_m(x,y,z,f)|_{dBm} - H_z(x,y,z,f)|_{dB\frac{A}{m}} \tag{C-9}$$

$$\mathrm{PF(f)}|_{dBm.\frac{m}{A}} = 10log\,\frac{[G(f)*A_{cable}(f)*\mathrm{A}(f)*H_z(x,y,z,f)]^2}{50} \tag{C-10}$$

One way to characterize the performance factor of the measurement chain is to use a radiation source whose analytical equation of the magnetic field is known and correlate the value of the field obtained by the analytical solution with the value of the voltage measured by an analyzer.

In the framework of this study, a transmission line placed on a ground plane is used to determine the PF by measuring the input power of the spectrum analyzer and calculating the analytical magnetic field. The calibration of the magnetic probe is carried out on a frequency band and at several points in space around the transmission line. This transmission line which the theoretical radiation is known, determines the PF of the probe. The measurement consists in making a horizontal scan (xy plane, see in Figure C.4) with the measurement probe above the conductive wire of the transmission line. The latter is placed above the ground plane at a height equal to 2.05 mm. Figure C.4 shows the calibration circuit carried out in the laboratory. The test setup used to calibrate the probe is composed of the transmission line loaded by Z_0 (50 Ω

impedance). The line is connected to a generator delivering a power P. The parameters h and a are shown in Figure C.4.

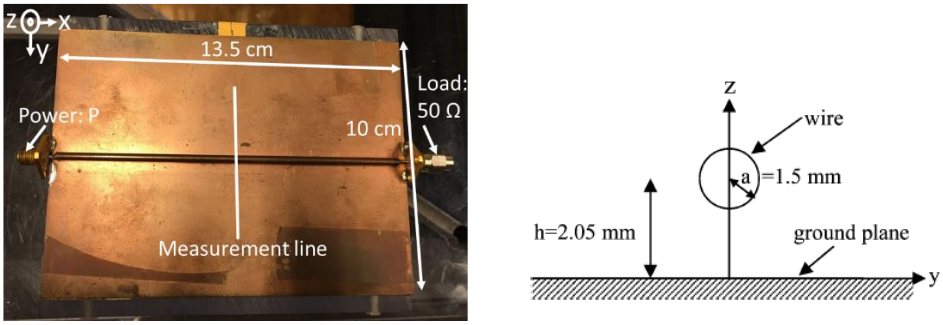

Figure C.4 Transmission line configuration

The analytical formulas allowing to give the components of the magnetic field created by the transmission line are given below. We will assume that the ground plane is a perfect conductor of infinite dimensions.

$$H_x = 0 \tag{C-11}$$

$$H_y = -\frac{1}{\eta} 4K \frac{n(y^2-z^2+n^2)}{(y^2+(z+n)^2)(y^2+(z-n)^2)} \tag{C-12}$$

$$H_z = -\frac{1}{\eta} 8K \frac{yzn}{(y^2+(z+n)^2)(y^2+(z-n)^2)} \tag{C-13}$$

where

$$K = \frac{\sqrt{2PZ_0}}{\ln(\frac{h+n}{h-n})} \tag{C-14}$$

$$\eta = \frac{\mu_0}{\varepsilon_0} \tag{C-15}$$

$$n = \sqrt{h^2 - a^2} \tag{C-16}$$

The selection of the component for the magnetic field H used to obtain the PF is arbitrary. Therefore, the H_z component is reserved for this. The method used involves the place where the probe is and the sinusoidal signal supplied to the transmission line.

Figure C.5 shows the values of two components H_y, H_z obtained by the analytical model at a distance of 22 mm above the transmission line (taken along the y axis). It is based on the probe PBS H3 at a frequency of 85 kHz.

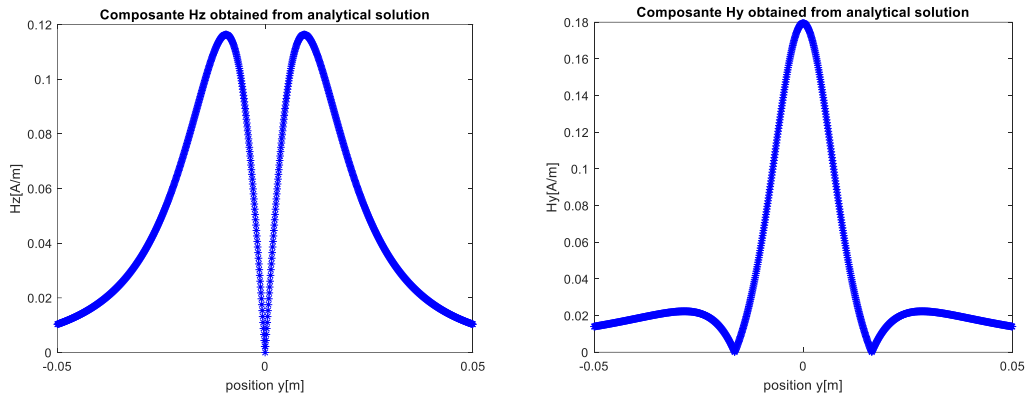

Figure C.5 Component H_z and H_y obtained from the analytical solution (on the transmission line)

The parameters used in the analytical equations are:

$$P_m|_{dBm\ m/A} = -42.14 \text{ (Measured by the spectrum analyzer)}$$

$$P = 0.2927 \text{ W (Supplied by the generator to the line)}$$

So, according to the equations above, the performance factor of PBS H3 is $-24\ dBm\ m/A$.

4) Relation between the frequency and the performance factor

According to the method to determine PF above, PF can be obtained for two probes of the manufacturer AARONIA: probes PBSH3 (25mm) and PBSH2 (12mm) separately. The PF versus frequency curves is displayed in Figure C.6 on different sizes of the probes. It can be observed that the larger size of the probes provides the higher PFs.

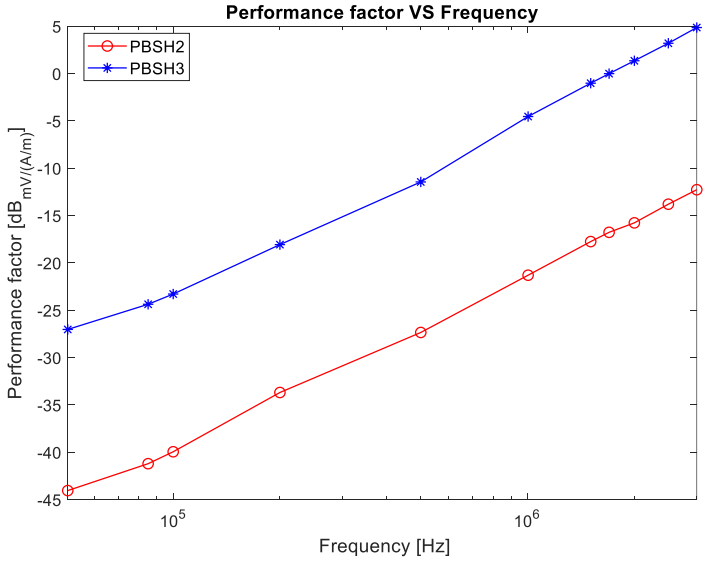

Figure C.6 Performance factor VS Frequency on different probes: PBS H2/PBS H3

Appendix D

Support vector regression

The best combination of the parameters $(\boldsymbol{w}, b)$ is found to minimize the deviation of the model predictions from the training samples outside the ε-intensive zone. This can be done via the following optimization problem:

$$\begin{aligned} &\min_{\boldsymbol{w}, b} \frac{1}{2}\|\boldsymbol{w}\|^2 + C\sum_{i=1}^{N}(\xi_i + \xi_i^*), \\ &\text{Subject to } y_i - \boldsymbol{w}^T\Phi(\boldsymbol{x}_i) - b \le \varepsilon + \xi_i, \\ &\qquad \boldsymbol{w}^T\Phi(\boldsymbol{x}_i) + b - y_i \le \varepsilon + \xi_i^*, \\ &\qquad \xi_i, \xi_i^* \ge 0, for\ i = 1, \cdots, N \end{aligned} \tag{D-1}$$

where ξ_i and ξ_i^* are the slack variables, which measure the deviation from the insensitive tube.

Next, equation (D-1) can be solved by using the Lagrangian function as follows:

$$\begin{aligned} &\min_{\boldsymbol{w}, b, \xi_i, \xi_i^*} \quad \max_{\mu_i \ge 0, \mu_i^* \ge 0, \alpha_i \ge 0, \alpha_i^* \ge 0} \quad L(\boldsymbol{w}, b, \xi_i, \xi_i^*, \mu_i, \mu_i^*, \alpha_i, \alpha_i^*) \\ &= \frac{1}{2}\|\boldsymbol{w}\|^2 + C\sum_{i=1}^{N}(\xi_i + \xi_i^*) - \sum_{i=1}^{N}(\mu_i\xi_i + \mu_i^*\xi_i^*) + \sum_{i=1}^{N}\alpha_i(y_i - \boldsymbol{w}^T\Phi(\boldsymbol{x}_i) - b - \varepsilon - \xi_i) + \\ &\quad \sum_{i=1}^{N}\alpha_i^*(-\varepsilon - \xi_i^* + \boldsymbol{w}^T\Phi(\boldsymbol{x}_i) + b - y_i) \end{aligned} \tag{D-2}$$

where $\mu_i, \mu_i^*, \alpha_i, \alpha_i^*$ are all the Lagrangian coefficients.

Equation (D-2) can be transformed into an equivalent dual problem via Lagrangian duals as follows:

$$\begin{aligned} &\max_{\mu_i \ge 0, \mu_i^* \ge 0, \alpha_i \ge 0, \alpha_i^* \ge 0} \quad \min_{\boldsymbol{w}, b, \xi_i, \xi_i^*} \quad L(\boldsymbol{w}, b, \xi_i, \xi_i^*, \mu_i, \mu_i^*, \alpha_i, \alpha_i^*) \\ &= \frac{1}{2}\|\boldsymbol{w}\|^2 + C\sum_{i=1}^{N}(\xi_i + \xi_i^*) - \sum_{i=1}^{N}(\mu_i\xi_i + \mu_i^*\xi_i^*) \\ &\qquad + \sum_{i=1}^{N}\alpha_i(y_i - \boldsymbol{w}^T\Phi(\boldsymbol{x}_i) - b - \varepsilon - \xi_i) + \sum_{i=1}^{N}\alpha_i^*(\boldsymbol{w}^T\Phi(\boldsymbol{x}_i) + b - y_i - \varepsilon - \xi_i^*) \end{aligned} \tag{D-3}$$

Then, $\boldsymbol{w}, b, \xi_i, \xi_i^*$ are solved for the minimal values separately by finding the partial derivatives on equation (D-3):

$$\frac{\partial L}{\partial \boldsymbol{w}} = 0 \Rightarrow \boldsymbol{w} = \sum_{i=1}^{N}(\alpha_i - \alpha_i^*)\Phi(\boldsymbol{x}_i) \tag{D-4}$$

$$\frac{\partial L}{\partial b} = 0 \Rightarrow \sum_{i=1}^{N}(\alpha_i - \alpha_i^*) = 0 \tag{D-5}$$

$$\frac{\partial L}{\partial \xi_i} = 0 \Rightarrow C - \alpha_i - \mu_i = 0 \Rightarrow C = \alpha_i + \mu_i \tag{D-6}$$

$$\frac{\partial L}{\partial \xi_i^*} = 0 \Rightarrow C - \alpha_i^* - \mu_i^* = 0 \Rightarrow C = \alpha_i^* + \mu_i^* \tag{D-7}$$

These equations from (D-4) to (D-7) are put into equation (D-3) in order to remove $\boldsymbol{w}, b, \xi_i, \xi_i^*$:

$$\begin{aligned}
&\max_{\mu_i \geq 0, \mu_i^* \geq 0, \alpha_i \geq 0, \alpha_i^* \geq 0} L(\boldsymbol{w}, b, \xi_i, \xi_i^*, \mu_i, \mu_i^*, \alpha_i, \alpha_i^*) \\
&= \frac{1}{2}\|\boldsymbol{w}\|^2 + \sum_{i=1}^{N}(\alpha_i + \mu_i)\xi_i + \sum_{i=1}^{N}(\alpha_i^* + \mu_i^*)\xi_i^* - \sum_{i=1}^{N}(\mu_i\xi_i + \mu_i^*\xi_i^*) \\
&+ \sum_{i=1}^{N}\alpha_i(y_i - \boldsymbol{w}^T\Phi(\boldsymbol{x}_i) - b - \varepsilon - \xi_i) + \sum_{i=1}^{N}\alpha_i^*(\boldsymbol{w}^T\Phi(\boldsymbol{x}_i) + b - y_i - \varepsilon - \xi_i^*) \\
&= \frac{1}{2}\|\boldsymbol{w}\|^2 + \sum_{i=1}^{N}\alpha_i(y_i - \boldsymbol{w}^T\Phi(\boldsymbol{x}_i) - b - \varepsilon) + \sum_{i=1}^{N}\alpha_i^*(\boldsymbol{w}^T\Phi(\boldsymbol{x}_i) + b - y_i - \varepsilon) \\
&= \frac{1}{2}\boldsymbol{w}^T\left(\sum_{i=1}^{N}(\alpha_i - \alpha_i^*)\Phi(\boldsymbol{x}_i)\right) + \sum_{i=1}^{N}\alpha_i(y_i - \boldsymbol{w}^T\Phi(\boldsymbol{x}_i) - b - \varepsilon) \\
&+ \sum_{i=1}^{N}\alpha_i^*(\boldsymbol{w}^T\Phi(\boldsymbol{x}_i) + b - y_i - \varepsilon) \\
&= -\frac{1}{2}\boldsymbol{w}^T\sum_{i=1}^{N}(\alpha_i - \alpha_i^*)\Phi(\boldsymbol{x}_i) + \sum_{i=1}^{N}\alpha_i(y_i - b - \varepsilon) + \sum_{i=1}^{N}\alpha_i^*(b - y_i - \varepsilon) \\
&= -\frac{1}{2}\sum_{i=1}^{N}(\alpha_i - \alpha_i^*)\Phi(\boldsymbol{x}_i)^T\sum_{i=1}^{N}(\alpha_i - \alpha_i^*)\Phi(\boldsymbol{x}_i) - \sum_{i=1}^{N}(\alpha_i + \alpha_i^*)\,\varepsilon + \sum_{i=1}^{N}(\alpha_i - \alpha_i^*)\,y_i \\
&+ b\sum_{i=1}^{N}(\alpha_i^* - \alpha_i) \\
&= -\frac{1}{2}\sum_{i=1}^{N}\sum_{j=1}^{N}(\alpha_i - \alpha_i^*)\left(\alpha_j - \alpha_j^*\right)\Phi(\boldsymbol{x}_i)^T\Phi\left(\boldsymbol{x}_j\right) - \sum_{i=1}^{N}(\alpha_i + \alpha_i^*)\,\varepsilon + \sum_{i=1}^{N}(\alpha_i - \alpha_i^*)\,y_i
\end{aligned} \tag{D-8}$$

So, equation (D-8) is transformed below:

$$\arg\max_{\alpha,\,\alpha^*} -\frac{1}{2}\sum_{i=1}^{N}\sum_{j=1}^{N}(\alpha_i - \alpha_i^*)\left(\alpha_j - \alpha_j^*\right)\Phi(\boldsymbol{x}_i)^T\Phi\left(\boldsymbol{x}_j\right) - \sum_{i=1}^{N}(\alpha_i + \alpha_i^*)\,\varepsilon + \sum_{i=1}^{N}(\alpha_i - \alpha_i^*)\,y_i \tag{D-9}$$

under the constraints:

$$\sum_{i=1}^{N}(\alpha_i - \alpha_i^*) = 0 \text{ and } 0 \leq \alpha_i, \alpha_i^* \leq C, i = \{1, \cdots, N\} \tag{D-10}$$

Furthermore, equation (D-9) can be changed to equation (D-11):

$$\arg \underset{\alpha,\, \alpha^*}{min}\ \frac{1}{2}\sum_{i=1}^{N}\sum_{j=1}^{N}(\alpha_i - \alpha_i^*)\left(\alpha_j - \alpha_j^*\right) k\left(\boldsymbol{x}_i, \boldsymbol{x}_j\right) + \sum_{i=1}^{N}(\alpha_i + \alpha_i^*)\,\varepsilon - \sum_{i=1}^{N}(\alpha_i - \alpha_i^*)\,y_i \quad \text{(D-11)}$$

where $k\left(\boldsymbol{x}_i, \boldsymbol{x}_j\right) = \Phi(\boldsymbol{x}_i)^T \Phi\left(\boldsymbol{x}_j\right)$ is the kernel function that defines as the inner product in the *feature space* between the function $\Phi(\boldsymbol{x})$ evaluated at the training samples $\boldsymbol{x}_i$ and $\boldsymbol{x}_j$.

Therefore, the nonlinear SVR can be rewritten in the dual space as follows:

$$\mathcal{M}^{SVR}(\boldsymbol{x}) = \boldsymbol{w}^T \Phi(\boldsymbol{x}) + b = \sum_{i=1}^{N}(\alpha_i - \alpha_i^*) k(\boldsymbol{x}_i, \boldsymbol{x}) + b \quad \text{(D-12)}$$

where the coefficients α_i, α_i^* are calculated by the equation (D-11) with a sequential minimal optimization solver subject to the constraints in the equation (D-10); the bias term b is retrieved as a byproduct of the solution of equation (D-11).

Appendix E

Probability density function of the model response

When the metamodel coefficients are known, it can be used effectively for calculating the Probability Density Function (PDF) of the model response accurately by using large Monte-Carlo samples at a negligible cost. This yields a sample set of response quantities, say $\{y^{(i)} \equiv M^{metamodel}(x^{(i)}), i = 1, \cdots, N_K\}$. In order to obtain an accurate approximation of PDF of the model response, $N_K = 10^5 \sim 10^6$. There are two main ways to perform PDF:

1) Histogram plot

Histograms are a type of bar plot for numeric data that group the data into bins, which can help obtain a graphical representation of the response PDF.

2) Kernel density smoothing

Smoother representations may be obtained using kernel smoothing techniques. Broadly speaking, the kernel density approximation of the response PDF is given by:

$$\hat{f}_Y(y) = \frac{1}{N_K h_K} \sum_{i=1}^{N_K} K\left(\frac{y - M^{metamodel}(\boldsymbol{x}_i)}{h_K}\right) \quad \text{(E-1)}$$

where $K(\boldsymbol{x})$ is a suitable positive function called kernel, and h_K is the bandwith parameter. Well-known kernels are as follows:

- Gaussian kernel: $K(\boldsymbol{x}) = \frac{1}{\sqrt{2\pi}} e^{-\boldsymbol{x}^2/2}$. (E-2)
- Epanechnikov kernel: $K_E(\boldsymbol{x}) = \frac{3}{4}(1 - \boldsymbol{x}^2)1_{|\boldsymbol{x}| \le 1}$. (E-3)

Several values for the bandwidth h_K were proposed in Seather and Jones. In practice, one may select the following value when using a Gaussian kernel:

$$h = 0.9 {N_K}^{-1/5} \min(\hat{\sigma}_Y, (Q_{75} - Q_{25})/1.34) \quad \text{(E-4)}$$

where $Q_{75} - Q_{25}$ is the interquartile range of the data set (Q_{75} is the percentiles of samples in the data set for the percentages 75 in the interval [0,100], and Q_{25} is the percentiles of samples in the same data set for the percentages 25 in the interval [0,100]).

Appendix F

Ferrite structure developed by GeePs laboratory and Vedecom institute

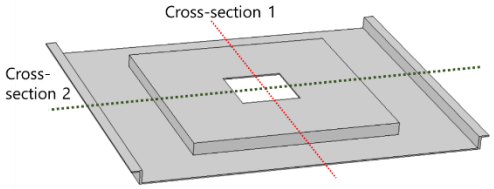

(a) Ferrite structure

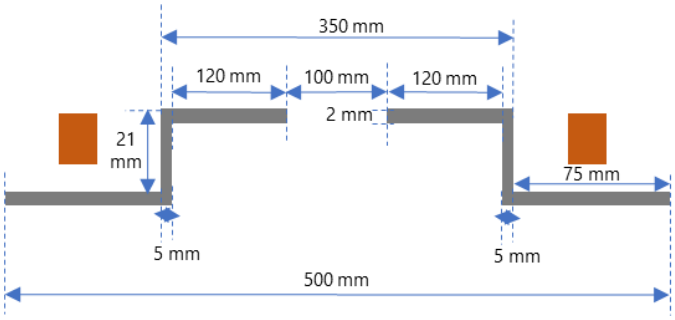

(b) Structure and dimensions of the cross-section 1

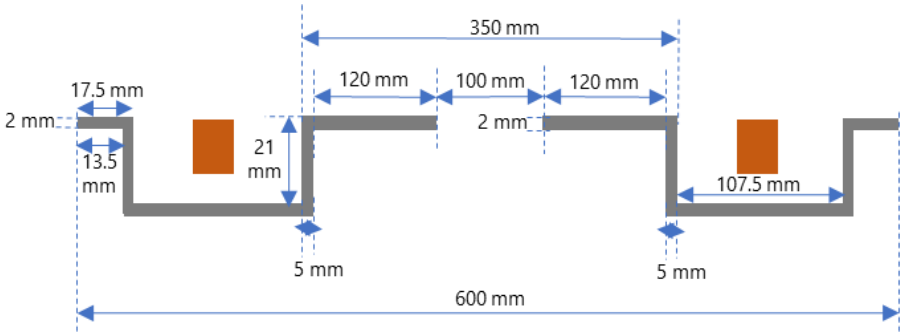

(c) Structure and dimensions of the cross-section 2

PUBLICATIONS

International Journals:

- Y. Pei, L. Pichon, Y. Le Bihan, M. Bensetti, and P. Dessante, "Fast Shielding Optimization of an Inductive Power Transfer System for Electric Vehicles", IEEE Access, vol. 10, pp. 91227–91234, 2022, doi: 10.1109/ACCESS.2022.3198953.
- Y. Pei, L. Pichon, M. Bensetti, and Y. Le Bihan, "Multiobjective optimization based on polynomial chaos expansions in the design of inductive power transfer systems," COMPEL - The international journal for computation and mathematics in electrical and electronic engineering, Jan. 2022.
- Y. Pei, Y. Le Bihan, M. Bensetti, and L. Pichon, "Comparison of Coupling Coils for Static Inductive Power-Transfer Systems Taking into Account Sources of Uncertainty," Sustainability, vol. 13, no. 11, p. 6324, Jun. 2021.
- Y. Pei, L. Pichon, M. Bensetti, and Y. Le Bihan, "Uncertainty quantification in the design of wireless power transfer systems," Open Physics, vol. 18, no. 1, pp. 391–396, Jan. 2020.

International Conferences:

- Y. Pei, K. Kadem, L.Pichon, M. Bensetti, and Y. Le Bihan. "Performance Analysis of a 30 kW Dynamic Wireless Power Transfer System for Electric Vehicle", IEEE Wireless Power Week (WPW 2022), July 2022, Bordeaux, France.
- Y. Pei, M. Bensetti, Y. Le Bihan, L. Pichon and K. Kadem. "Comparison of Maximum Transmission Efficiency and Magnetic Flux Leakage for Different Coupling Coils in Inductive Power Transfer Systems", The 7th Conference on Inductics (University-Industry), May 2022, Constantine, Algeria.
- Y. Pei, L. Pichon, M. Bensetti, and Y. Le Bihan, "Multi-objective Optimization based on Polynomial Chaos Expansions in the Design of Inductive Power Transfer Systems", Szczecin, Poland, Sep. 2021. Accessed: Sep. 02, 2022. [Online]. Available: https://hal.archives-ouvertes.fr/hal-03374275
- Y. Pei, P. Lagouanelle, and L. Pichon, "Uncertainty quantification and metamodeling in the design of inductive power transfer systems", 2021 JOINT IEEE INTERNATIONAL SYMPOSIUM ON ELECTROMAGNETIC COMPATIBILITY, SIGNAL & POWER INTEGRITY, AND EMC EUROPE, Glasgow, United Kingdom, Jul. 2021.
- S. Ding, Y. Pei, L. Pichon, and S. Koulouridis, "Impact of Parameters Variability on the Performances of an Implanted Antenna for Biomedical Applications," 2020 14th European Conference on Antennas and Propagation (EuCAP), 2020, pp. 1-4.

RÉSUMÉ DE THÈSE

Conception et optimisation des systèmes de transfert de puissance inductifs par des techniques de métamodélisation

Candidate: Yao PEI
Directeur de thèse:
Lionel Pichon – Directeur de Recherche au CNRS
Co-encadrants:
Mohamed Bensetti – Professeur à CentraleSupélec
Yann Le Bihan– Professeur à l'Université Paris-Saclay

I. Introduction

Le déploiement à grande échelle des véhicules à moteur à combustion interne dans les systèmes de transport contribue au réchauffement de la planète et au changement climatique. C'est la raison pour laquelle les véhicules électriques (VE) ont gagné en popularité sur le marché afin de réduire la dépendance aux combustibles fossiles comme sources d'énergie et leurs effets néfastes sur la planète. Cependant, les batteries des VE ont une faible densité énergétique, ce qui rend les véhicules lourds et coûteux. En outre, le temps de charge de la batterie est plus long que le temps nécessaire pour faire le plein d'une voiture fonctionnant aux combustibles fossiles. La durée de vie de la batterie est courte en raison de la tendance au vieillissement de son matériau. Et surtout, la capacité de la batterie limite l'autonomie des VE. Pour le développement des VE, les systèmes de charge jouent un rôle essentiel. La technologie actuellement disponible pour la recharge des batteries des VE est la méthode de recharge par branchement en utilisant des câbles électriques. Un des principaux problèmes liés à la recharge par branchement est la présence de câbles. Ils sont généralement difficiles à manipuler. Des risques peuvent survenir en raison de câbles endommagés ou d'une mauvaise manipulation de ceux-ci. Ainsi, en raison de ces inconvénients, le transfert de puissance inductif résonnant (TPIR) a été introduit récemment comme une nouvelle technologie alternative. Cette technologie a la capacité de remplacer l'interface de connexion entre un émetteur et un récepteur, permettant un transfert d'énergie sans contact. De plus, son application pour la charge pendant le déplacement du véhicule est prometteuse à long terme pour surmonter les obstacles que représentent le lourd stockage des batteries à bord des VE et le long temps de recharge.

Figure 1 montre le schéma fonctionnel d'un système TPIR pour les VE. Le réseau électrique fournit une tension de liaison DC pour le système par l'intermédiaire d'un convertisseur AC/DC avec correction du facteur de puissance. Le système se compose

d'un émetteur (placé au sol), d'un récepteur (placé sous le plancher du véhicule), de convertisseurs et de topologies de compensation. Le champ magnétique produit par l'émetteur induit un champ tension alternative dans le récepteur. Le courant alternatif est ensuite redressé afin de charger la batterie. Des topologies de compensation sont ajoutées à l'émetteur et au récepteur pour créer une résonance et réduire les pertes.

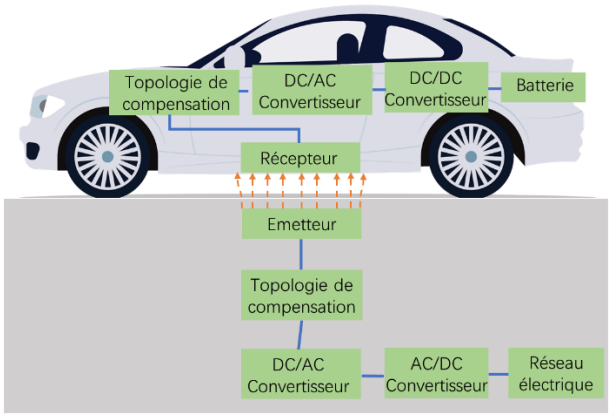

Figure 1 Schéma général des composants d'un système TPIR pour VE

Bien que les systèmes TPIR soient désormais largement étudiés, la conception des coupleurs (ensemble émetteur /récepteur) présente encore plusieurs défis. Jusqu'à présent, il n'existe pas de méthodologie complète permettant une conception et une optimisation rapide, fiable et efficace d'un système TPIR. Les méthodologies adéquates doivent prendre en compte l'environnement du système, y compris l'impact du châssis de la voiture et la présence du corps humain. Il faut en effet évaluer le niveau d'exposition afin d'être conforme aux recommandations internationales, telles que SAE J2954 et ICNIRP 2020. Récemment, des modèles 3D ont été étudiés et exploités pour résoudre le problème électromagnétique associé au système sans contact et son environnement proche. Ces approches de calcul produisent des résultats fiables et précis relatif aux paramètres électriques (inductance mutuelle, efficacité du transfert) et magnétiques (champ magnétique rayonné autour du système). Cependant, la conception du système dépend fortement d'un grand nombre de paramètres divers: forme des bobines, caractéristiques géométriques de la structure (châssis du véhicule, ferrite, plaques de blindage), désalignement possible entre l'émetteur et le récepteur pendant la charge, etc. Au cours du processus de conception du système TPIR, ce point peut conduire à des calculs lourds pour répéter chaque nouvelle configuration. Face à cette situation, l'introduction d'outils stochastiques et de metamodèles permet de traiter la variabilité de tous les paramètres décrivant le problème électromagnétique.

L'objectif de la thèse est de proposer une méthodologie de modélisation afin d'évaluer l'efficacité des systèmes TPIR et de gérer les contraintes CEM dans les VE. La méthode

inclut simultanément divers aspects du problème électromagnétique : forme des bobines, et caractéristiques géométriques des éléments du système (châssis du véhicule, ferrite, plaques de blindage). L'introduction de techniques de métamodélisation permet de gérer la variation de tous les paramètres décrivant le problème électromagnétique et de déterminer quantitativement la contribution de chaque variable de conception au résultat. L'objectif final de l'approche est d'obtenir des conclusions rapides à faible coût pendant le processus de conception du système en considérant l'exposition des personnes.

La méthodologie repose sur la combinaison d'un logiciel 3D de la simulation électromagnétique avec des techniques de métamodélisation (régression par machine à vecteur de support (SVR), algorithme de programmation génétique multigénique (MGPA), expansions de chaos polynomial (PCE)). L'approche proposée combine les techniques de calcul électromagnétique avec des outils statistiques pour construire des méta-modèles. Ceux-ci sont alors utilisés pour obtenir, de manière parcimonieuse, la distribution de la quantité d'intérêt (inductance mutuelle, densité de flux magnétique). Ils remplacent ainsi des équations analytiques approximatives et/ou des simulations numériques très coûteuses. En effet, quand une structure complexe de coupleur est impliquée dans le processus de conception avec un grand nombre de variables, les équations analytiques deviennent très difficiles à obtenir, et une méthode de modélisation 3D (MEF par exemple) prend beaucoup de temps pour simuler toutes les configurations requises. Par ailleurs, dans ce type de problème, les indices de Sobol permettent d'obtenir des estimations quantitatives de la sensibilité de la solution par rapport aux divers paramètres en jeu. Plus l'indice de Sobol est élevé, plus l'influence du paramètre (ou de l'ensemble des paramètres) concerné sur la sortie est forte. Le calcul des indices de Sobol implique des intégrales multidimensionnelles qui sont coûteuses à évaluer dans le cas général. Avec une technique de méta-modélisation, la solution est simple et rapide.

II. Analyse et résultats des coupleurs

Dans une première partie, l'efficacité de transmission maximale et le rayonnement du champ magnétique ont été analysés pour quatre formes de coupleurs (circulaire, carré, bipolaire (BP) et double-D (DD)). Nous avons modélisé ces structures de coupleurs par des calculs FEM COMSOL 3D puis vérifié les prédictions numériques par des mesures expérimentales sur des prototypes à l'échelle 1:10 développés dans le laboratoire GeePs (Figure 2).

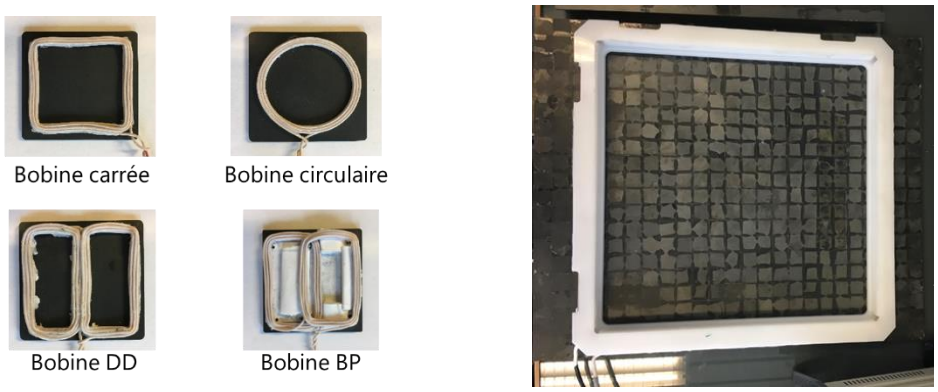

(a) Bobines à échelle réduite d'un facteur 1/10 (b) Bobine carrée à échelle réelle

Figure 2 Prototypes développés au laboratoire GeePs

Le circuit électrique de la topologie de compensation série-série a été considéré pour le système TPIR. Il apparaît que le rapport entre la longueur du fil conducteur de la bobine et l'inductance mutuelle influence directement l'efficacité maximale de la transmission quand l'émetteur et le récepteur sont identiques. Concernant l'efficacité de transmission maximale dans les systèmes TPIR, nous avons montré que les coupleurs circulaires fournissent les valeurs maximales. Cependant, les coupleurs carrés ont une plus grande tolérance au désalignement que les autres. En revanche, les coupleurs carrés ont davantage de fuites de densité de flux magnétique au-dessus du récepteur que les autres. Toutefois, en se concentrant sur la tolérance au désalignement qui est un paramètre critique, des coupleurs carrés peuvent être préconisées pour un système TPIR. Dans une seconde partie, des coupleurs carrés à échelle réelle ont également été étudiées, et nous avons montré qu'il y a un très bon accord entre la simulation et la mesure. De plus pour l'inductance propre et la densité de flux magnétique, nous avons identifié la relation entre les valeurs du système réel et celles du système réduit. Bien que les coefficients de couplage aient été comparés précédemment pour les quatre formes de coupleurs, la variabilité de l'efficacité de transmission maximale avec le désalignement a été évaluée pour la première fois. La distribution du champ magnétique dans toute la zone autour du système de coupleurs a également été déterminée. Il s'agit d'une analyse complète qui va au-delà de ce qui est généralement observé dans la littérature où seulement un ou plusieurs points de mesure sont considérés.

III. Analyse des systèmes TPIR par métamodélisation

Afin de prendre en compte les sources d'incertitude (le désalignement le long des axes X/Y, variation le long de l'axe Z ou la rotation sur le récepteur) illustrées par la figure 3, différents métamodèles SVR, MGPA et PCE ont été comparés pour analyser les variations

de l'inductance mutuelle dans le cas de coupleur carré à échelle réduite. En raison du compromis entre le temps de calcul et la précision du métamodèle, le PCE a été choisi pour prédire les valeurs de l'inductance mutuelle pour différentes formes de coupleurs.

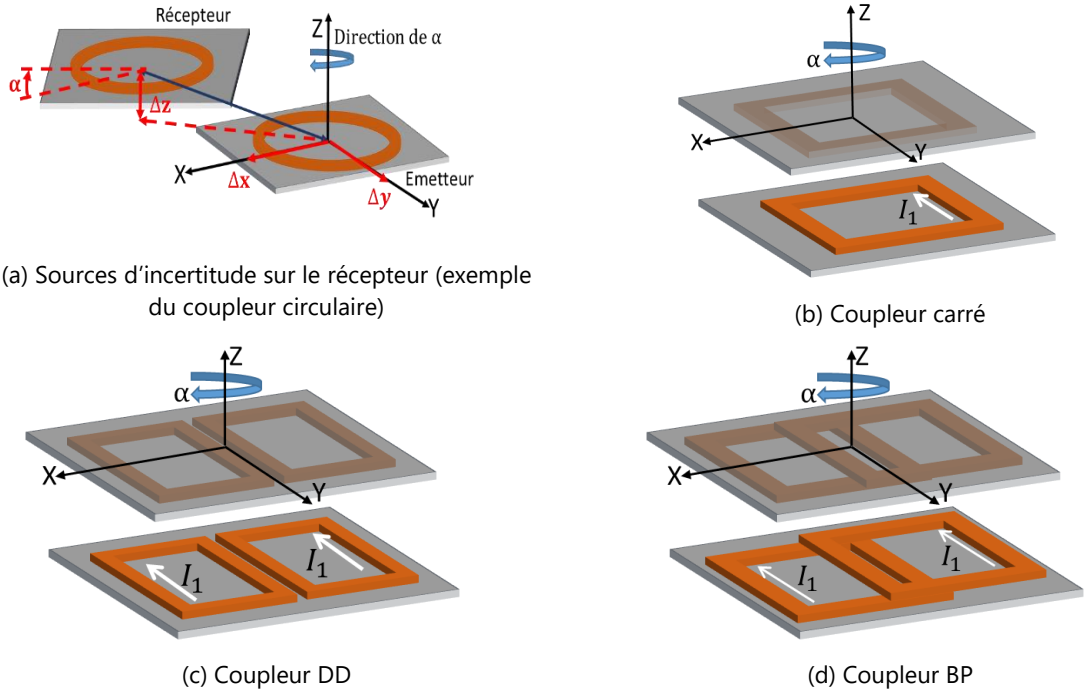

(a) Sources d'incertitude sur le récepteur (exemple du coupleur circulaire)

(b) Coupleur carré

(c) Coupleur DD

(d) Coupleur BP

Figure 3 Sources d'incertitude pour quatre formes de coupleurs

Ensuite, des méta-modèles de type PCE ont été exploités pour les quatre formes de coupleurs. Selon l'analyse de sensibilité basée sur les coefficients des métamodèles PCE, le désalignement le long de l'axe X s'est avéré le facteur le plus influent sur l'inductance mutuelle M pour les coupleurs DD/BP, alors que le désalignement le long de l'axe X/Y a le même effet sur les coupleurs circulaire et carré, en raison de leurs symétries. Compte tenu de l'impact des sources d'incertitude sur l'inductance mutuelle, le rapport entre la longueur du fil conducteur et l'inductance mutuelle peut être aide à concevoir la forme des bobines pour une efficacité de transmission maximale. Les coupleurs circulaires devraient en théorie être recommandés pour le système TPIR statique en raison de leur valeur plus élevée de l'efficacité de transmission maximale (par rapport aux autres coupleurs). Ainsi, cette technique de métamodélisation par polynômes chaos (PCE) se révèle donc comme étant un outil très utile dans l'analyse du système RIPT afin d'économiser le temps et les ressources de calcul.

IV. Conception et optimisation du système TPIR

Une optimisation multi objectifs combinée avec une technique de métamodélisation PCE a été proposée pour un système TPIR sans blindage (développé au laboratoire GeePs

et l'institut Vedecom) et un autre système avec blindage (développé au laboratoire GeePs). Ils sont présentés dans la figure 4. Le but était de déterminer les dimensions du système, afin d'une part d'améliorer l'efficacité de la transmission et d'autre part de réduire le poids/le coût du système tout en prenant en compte les recommandations de l'ICNIRP.

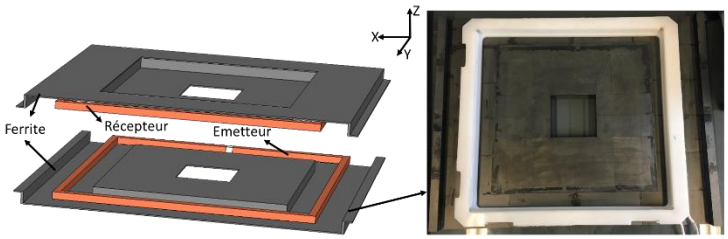

(a) Système TPIR sans blindage

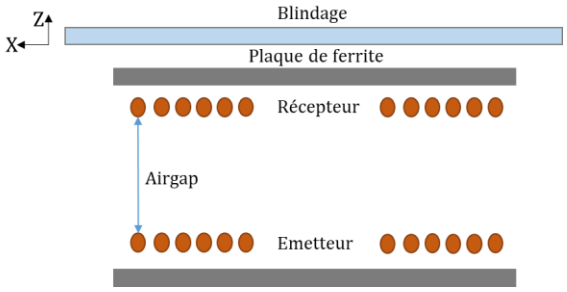

(b) Système TPIR avec blindage

Figure 4 Système TPIR pratique

L'inductance mutuelle influence le plus l'efficacité maximale de la transmission si l'émetteur et récepteur sont identiques, et si la longueur du fil est prédéfinie. Les fonctions objectives qui apparaissent naturellement en vue d'un dimensionnement sont ainsi:

1) l'inductance mutuelle avec des variables de conception, qui doit être maximisée;
2) le volume/masse de la ferrite (sans plaque d'aluminium) ou le coût du blindage (incluant la ferrite et les structures en aluminium; avec plaque d'aluminium), qui doit être minimisée, afin d'économiser le budget du système TPIR.

Dans notre travail, avec COMSOL, le temps pour un seul calcul (déterminant l'inductance mutuelle) est compris entre 1 et 5 minutes sur un processeur Intel Xeon W-2125. Le temps de calcul dépend de la complexité du modèle MEF 3D et de la taille du maillage. Cependant, pour construire un métamodèle PCE précis avec plus de trois variables de conception, il faut au moins 100 calculs du modèle MEF 3D, ce qui nécessite au moins 2,4 heures. En revanche, l'évaluation de l'inductance mutuelle basée sur le métamodèle PCE requiert de 1 à 2 secondes avec un processeur Intel(R) Core (TM) i5-8365U (CPU @ 1.60GHz 1.90 GHz). C'est pourquoi, le processus d'optimisation basé sur

le métamodèle PCE prend environ 15 minutes. Par conséquent, par rapport à une approche traditionnelle combinant directement des calculs MEF 3D avec une méthode d'optimisation multi objectifs, la technique proposée permet d'économiser un temps de calcul très significatif (même si l'on prend en compte le temps de calcul des échantillons d'apprentissage du métamodèle). Elle permet également de réduire d'environ un facteur deux les ressources informatiques (le prix du processeur Intel Xeon W-2125 est deux fois plus élevé que celui du processeur Intel(R) Core i5-8365U). Le temps de calcul économisé dépend fortement du nombre de variables de conception et des paramètres définis dans l'algorithme d'optimisation.

Dans le cas sans blindage: la taille de la plaque de ferrite a été optimisée pour une taille donnée de la bobine grâce à la métamodélisation PCE et à l'algorithme NSGA-II (Non-dominated Sorting Genetic Algorithm II). Puis nous avons comparé ensuite deux algorithmes d'optimisation: NSGA-II et Multiobjective Particle Swarm optimization (MOPSO) afin de déterminer l'algorithme le plus efficace en combinaison avec la technique PCE. Ceci a été étudié dans le cas avec d'un système avec une plaque d'aluminium. Il en est ressorti que MOPSO nécessite un temps de calcul plus faible, et le front de Pareto de MOPSO peut donner un plus grand ensemble de solutions réalisables que NSGAI-II avec la même taille de la population et de générations. Pour conclure, un méta-modèle basé sur la méthode PCE avec MOPSO s'avère une approche performante pour effectuer l'optimisation lorsqu'on considère le système impliquant un grand nombre de variables de conception sous contraintes.

Les dimensions du blindage en ferrite et en aluminium peuvent être sélectionnées par la méthode proposée précédemment, mais celle-ci est limitée quant au positionnement de la ferrite et à sa forme géométrique. Afin d'étendre la portée de l'approche, une optimisation topologique (OT) a été exploitée pour trouver une distribution de ferrite qui maximise l'inductance mutuelle, tout en contraignant le volume de la plaque de ferrite. Bien qu'il existe plusieurs méthodes OT dans la littérature, la méthode du matériau isotrope solide avec pénalisation (MISP) est aujourd'hui la plus utilisée en raison de sa mise en œuvre facile et intuitive. L'OT avec la méthode MISP a ainsi été adoptée pour organiser la distribution de la ferrite dans ce travail. En étudiant un système TPIR sans plaque d'aluminium, puis avec une plaque d'aluminium, nous avons montré qu'une partie de la ferrite au centre et sur les bords peut être enlevée sans affecter de façon notable l'inductance mutuelle. Il faut souligner que les résultats d'OT sont influencés par la plaque d'aluminium près du domaine de conception de la ferrite afin de diminuer les pertes par courants de Foucault sur le châssis. La dimension de la ferrite du côté du récepteur doit être plus grande que celle du côté de l'émetteur. Ces résultats donnent quelques lignes directrices pour disposer la ferrite sur la taille préfixée pour les systèmes TPIR.

V. Conclusion

Pour un système TPIR, un coupleur carré semble présenter plusieurs avantages notamment la tolérance au désalignement. La contrepartie est une fuite de densité de flux magnétique plus importante que les autres topologies.

Afin de prendre en compte des sources d'incertitude, plusieurs techniques de métamodélisation ont été combinées avec COMSOL pour construire des métamodèles. Elles ont été comparées sur le coupleur carré à échelle réduite. La technique de métamodélisation PCE (polynômes chaos) a été retenue en raison de sa précision et de sa capacité à effectuer l'analyse de sensibilité. De plus, elle a été également utilisée dans d'autres bobines de couplage. Ainsi, cette technique avère donc comme étant un outil très utile en vue du dimensionnement de systèmes TPIR.

La combinaison de COMSOL avec une technique de métamodélisation PCE a été proposée pour exprimer la relation entre l'inductance mutuelle et les variables de conception et pour optimiser le système. En effet, si une configuration complexe de coupleur avec un grand nombre de variables est impliquée dans le processus de conception, les équations analytiques deviennent très difficiles à obtenir, et la méthode MEF 3D prendrait trop de temps pour simuler toutes les configurations requises. Pour réduire le temps de calcul, l'algorithme MOPSO avec la technique de métamodélisation PCE fournit une solution rapide et simple, améliorant ainsi l'inductance mutuelle et réduisant le coût du calcul. Cette optimisation a été réalisée en prenant en compte les recommandations de l'ICNIRP. Pour ce qui concerne le dimensionnement de la ferrite, la méthode OT avec MISP a été mise en œuvre. Elle a montré qu'une partie de la ferrite au centre et sur les bords du système peut être supprimée tout en maintenant la valeur de l'inductance mutuelle. De plus, en présence d'a une plaque d'aluminium dans le système du côté du récepteur, la dimension de la ferrite située près de la plaque d'aluminium doit être choisie plus grande que celle du côté de l'émetteur si l'on veut conserver une même valeur d'inductance mutuelle.

REFERENCES

References

[1] M. Eshani, Y. Gao, S. E. Gay, and A. Emadi, "Modern electric, hybrid electric and fuel cell vehicles", in Fundamentals, Theory, and Design. Boca Raton, FL, USA: CRC Press, 2005.

[2] M. Yilmaz and P. T. Krein, "Review of battery charger topologies, charging power levels, and infrastructure for plug-in electric and hybrid vehicles", IEEE Trans. Power Electron., vol. 28, no. 5, pp. 2151–2169, May 2013.

[3] C T. Rim and C. Mi, "Wireless Power Transfer for Electric Vehicles and Mobile Devices | IEEE eBooks | IEEE Xplore". https://ieeexplore-ieee-org.ezproxy.universite-paris-saclay.fr/book/7953908 (accessed Sep. 25, 2022).

[4] T. M. Fisher, K. B. Farley, Y. Gao, H. Bai, and Z. T. Tse, "Electric vehicle wireless charging technology: A state-of-the-art review of magnetic coupling systems", Wireless Power Transf., vol. 1, no. 2, pp. 87–96, 2014.

[5] A. Mahesh, B. Chokkalingam, and L. Mihet-Popa, "Inductive Wireless Power Transfer Charging for Electric Vehicles–A Review", IEEE Access, vol. 9, pp. 137667–137713, 2021, doi: 10.1109/ACCESS.2021.3116678.

[6] "Wireless power transfer", Wikipedia. Jun. 11, 2022. Accessed: Jun. 16, 2022. [Online]. Available: https://en.wikipedia.org/w/index.php?title=Wireless_power_transfer&oldid=1092693026

[7] "WPT History", IEEE-WPT. https://wpt.ieee.org/wpt-history/ (accessed Jun. 16, 2022).

[8] N. Shinohara, Wireless Power Transfer via Radiowaves. John Wiley & Sons, 2014.

[9] J. A. Angelo, Encyclopedia of Space and Astronomy. Infobase Publishing, 2014.

[10] N. Tesla, "Apparatus for transmitting electrical energy", U. S. Patent 1119732 A, Dec. 1, 1914.

[11] W. C. Brown, "The history of wireless power transmission", Sol. Energy, vol. 56, no. 1, pp. 3–21, Jan. 1996.

[12] S. Niu, H. Xu, Z. Sun, Z. Y. Shao, and L. Jian, "The state-of-the-arts of wireless electric vehicle charging via magnetic resonance: principles, standards and core technologies", Renewable and Sustainable Energy Reviews, vol. 114, p. 109302, Oct. 2019, doi: 10.1016/j.rser.2019.109302.

[13] "Non-Contact Power Supply Transport System Technology | Technology | Solutions", DAIFUKU. https://www.daifuku.com/solution/technology/wirelesspower/ (accessed Jun. 16, 2022).

[14] "General Motors EV1", Wikipedia. Jun. 14, 2022. Accessed: Jun. 16, 2022. [Online]. Available: https://en.wikipedia.org/w/index.php?title=General_Motors_EV1&oldid=1093115724

[15] A. Kurs, A. Karalis, R. Moffatt, J. D. Joannopoulos, P. Fisher, and M. Soljačić, "Wireless Power Transfer via Strongly Coupled Magnetic Resonances", Science, vol. 317, no. 5834, pp. 83–86, Jul. 2007, doi: 10.1126/science.1143254.

[16] G. A. J. Elliott, S. Raabe, G. A. Covic, and J. T. Boys, "Multiphase Pickups for Large Lateral Tolerance Contactless Power-Transfer Systems", IEEE Transactions on Industrial Electronics, vol. 57, no. 5, pp. 1590–1598, May 2010, doi: 10.1109/TIE.2009.2031184.

[17] "ELIX Wireless introduces MDC-based 10kW wireless charging solution", Green Car Congress. https://www.greencarcongress.com/2015/07/20150715-elix.html (accessed Jun. 16, 2022).

[18] W. Li, "High efficiency wireless power transmission at low frequency using permanent magnet coupling", University of British Columbia, 2009. doi: 10.14288/1.0067661.

[19] F. Turki, "Metal foreign object detection system for inductive power transmission systems", DE102012108671A1, May 28, 2014 Accessed: Jun. 16, 2022. [Online]. Available: https://patents.google.com/patent/DE102012108671A1/en

[20] A. Westlake, "Qualcomm reveals BMW i8 Formula E safety car with wireless charging – SlashGear", SlashGear.com, Aug. 25, 2015. https://www.slashgear.com/qualcomm-reveals-bmw-i8-formula-e-safety-car-with-wireless-charging-25399244/ (accessed Jun. 16, 2022).

[21] K. Woronowicz, R. Czainski, D. Anders, and A. SAFAEE, "A method of operating a three phase primary winding structure and a primary unit", EP3071440A1, Sep. 28, 2016 Accessed: Jun. 16, 2022. [Online]. Available: https://patents.google.com/patent/EP3071440A1/en

[22] February 9 and 2017, "WiTricity Collaborating with Nissan on Wireless Charging for Electric Vehicles", WiTricity, Feb. 09, 2017. https://witricity.com/newsroom/press-releases/witricity-collaborating-nissan-wireless-charging-electric-vehicles/ (accessed Jun. 16, 2022).

[23] "Momentum Dynamics Announces Dual-Power Breakthrough in Automatic Inductive Charging", Momentum Dynamics, May 05, 2022. https://momentumdynamics.com/momentum-dynamics-announces-dual-power-breakthrough-in-automatic-inductive-charging/ (accessed Jun. 16, 2022).

[24] Wireless Power Transfer for Electric Vehicles: Foundations and Design Approach. Accessed: May 12, 2022. [Online]. Available: https://link.springer.com/book/10.1007/978-3-030-26706-3

[25] Z. Wang, Y. Zhang, X. He, B. Luo, and R. Mai, "Research and Application of Capacitive Power Transfer System: A Review," Electronics, vol. 11, no. 7, p. 1158, Apr. 2022, doi: 10.3390/electronics11071158.

[26] M. Kline, I. Izyumin, B. Boser, and S. Sanders, "Capacitive power transfer for contactless charging", in 2011 Twenty-

Sixth Annual IEEE Applied Power Electronics Conference and Exposition (APEC), Mar. 2011, pp. 1398–1404. doi: 10.1109/APEC.2011.5744775.

[27] J. Dai and D. C. Ludois, "A Survey of Wireless Power Transfer and a Critical Comparison of Inductive and Capacitive Coupling for Small Gap Applications", IEEE Transactions on Power Electronics, vol. 30, no. 11, pp. 6017–6029, Nov. 2015, doi: 10.1109/TPEL.2015.2415253.

[28] A. Triviño, J. M. González-González, and J. A. Aguado, "Wireless Power Transfer Technologies Applied to Electric Vehicles: A Review," Energies, vol. 14, no. 6, p. 1547, Mar. 2021, doi: 10.3390/en14061547.

[29] "World's First Electric Bus with Bombardier's PRIMOVE System Begins Revenue Service", Bombardier. https://bombardier.com/en/media/news/worlds-first-electric-bus-bombardiers-primove-system-begins-revenue-service (accessed Sep. 19, 2022).

[30] C. Panchal, S. Stegen, and J. Lu, "Review of static and dynamic wireless electric vehicle charging system", Engineering Science and Technology, an International Journal, vol. 21, no. 5, pp. 922–937, Oct. 2018, doi: 10.1016/j.jestch.2018.06.015.

[31] S. Y. Choi, B. W. Gu, S. Y. Jeong, and C. T. Rim, "Advances in wireless power transfer systems for roadway-powered electric vehicles", IEEE J. Emerg. Sel. Topics Power Electron., vol. 3, no. 1, pp. 18-36, Mar. 2015.

[32] J. H. Kim, B.-S. Lee, J.-H. Lee, S.-H. Lee, C.-B. Park, S.-M. Jung, S.-G. Lee, K.-P. Yi, and J. Baek, "Development of 1-MW inductive power transfer system for a high-speed train", IEEE Trans. Ind. Electron., vol. 62, no. 10, pp. 6242_6250, Oct. 2015.

[33] Y. Jang, S. Jeong, and M. Lee, "Initial Energy Logistics Cost Analysis for Stationary, Quasi-Dynamic, and Dynamic Wireless Charging Public Transportation Systems," Energies, vol. 9, no. 7, p. 483, Jun. 2016, doi: 10.3390/en9070483.

[34] Onar OC, Miller JM, Chinthavali M, Jones PT. ORNL developments in stationary and dynamic wireless charging. In: Proceedings of the IEEE Applied Power Electronics Conference & Exposition (APEC), March 19; 2014.

[35] G. A. Covic and J. T. Boys, "Modern Trends in Inductive Power Transfer for Transportation Applications", IEEE Journal of Emerging and Selected Topics in Power Electronics, vol. 1, no. 1, pp. 28–41, Mar. 2013, doi: 10.1109/JESTPE.2013.2264473.

[36] "Vehicle Initiative Consortium for Transport Operation and Road Inductive Applications", Victoria Project, April. 25, 2017. http://greentechlatvia.eu/wp-content/uploads/bsk-pdf-manager/1-8_Project_Victoria_(Bludszuweit)_8.pdf (accessed Sept. 19, 2022).

[37] "Final Report Summary - FASTINCHARGE (Innovative fast inductive charging solution for electric vehicles) | FP7 | CORDIS | European Commission". https://cordis.europa.eu/project/id/314284/reporting (accessed Sep. 21, 2022).

[38] K. Barry, "Electric Buses Test Wireless Charging in Germany", Wired. Accessed: Jun. 22, 2022. [Online]. Available: https://www.wired.com/2013/03/wireless-charging-bus-germany/

[39] "Wireless charging for quiet and clean public transport in Torino (Italy) | Eltis". https://www.eltis.org/discover/case-studies/wireless-charging-quiet-and-clean-public-transport-torino-italy (accessed Jun. 22, 2022).

[40] "J2954: Wireless Power Transfer for Light-Duty Plug-in/Electric Vehicles and Alignment Methodology - SAE International." https://www.sae.org/standards/content/j2954_202010/ (accessed Mar. 26, 2021).

[41] "IEC 61980-1:2020 | IEC Webstore". https://webstore.iec.ch/publication/31657 (accessed Jun. 17, 2022).

[42] "ISO 19363:2020 Electrically propelled road vehicles — Magnetic field wireless power transfer — Safety and interoperability requirements", ISO. https://www.iso.org/cms/render/live/en/sites/isoorg/contents/data/standard/07/35/73547.html (accessed Jun. 17, 2022).

[43] C. Song et al., "Low EMF and EMI Design of a Tightly Coupled Handheld Resonant Magnetic Field (HH-RMF) Charger for Automotive Battery Charging", IEEE Transactions on Electromagnetic Compatibility, vol. 58, no. 4, pp. 1194–1206, Aug. 2016, doi: 10.1109/TEMC.2016.2557842.

[44] M. Abou Houran, X. Yang, and W. Chen, "Magnetically Coupled Resonance WPT: Review of Compensation Topologies, Resonator Structures with Misalignment, and EMI Diagnostics", Electronics, vol. 7, no. 11, p. 296, Nov. 2018, doi: 10.3390/electronics7110296.

[45] "ICNIRP Guidelines for Limiting Exposure to Electromagnetic Fields (1 Hz to 100 kHz)," Health Physics, vol. 118, no. 5, pp. 818-836, 2010.

[46] "ICNIRP Guidelines for Limiting Exposure to Electromagnetic Fields (100 kHz to 300 GHz)," Health Physics, vol. 118, no. 5, pp. 483–524, 2020.

[47] "IEEE Standard for Safety Levels with Respect to Human Exposure to Electric, Magnetic, and Electromagnetic Fields, 0 Hz to 300 GHz", IEEE Std C95.1-2019 (Revision of IEEE Std C95.1-2005/ Incorporates IEEE Std C95.1-2019/Cor 1-2019), pp. 1–312, Oct. 2019, doi: 10.1109/IEEESTD.2019.8859679.

[48] "IEEE Standard for Military Workplaces–Force Health Protection Regarding Personnel Exposure to Electric, Magnetic, and Electromagnetic Fields, 0 Hz to 300 GHz", IEEE Std C95.1-2345-2014, pp. 1–69, May 2014, doi: 10.1109/IEEESTD.2014.6820718.

[49] S. Jayalath and A. Khan, "Design, Challenges, and Trends of Inductive Power Transfer Couplers for Electric Vehicles: A Review", IEEE Journal of Emerging and Selected Topics in Power Electronics, vol. 9, no. 5, pp. 6196–6218, Oct. 2021, doi: 10.1109/JESTPE.2020.3042625.

[50] A. A. S. Mohamed, A. A. Shaier, H. Metwally, and S. I. Selem, "A comprehensive overview of inductive pad in electric vehicles stationary charging", Appl. Energy, vol. 262, Mar. 2020, Art. no. 114584.

[51] M. Budhia, G. A. Covic, and J. T. Boys, "Design and Optimization of Circular Magnetic Structures for Lumped Inductive Power Transfer Systems", IEEE Transactions on Power Electronics, vol. 26, no. 11, pp. 3096–3108, Nov. 2011, doi: 10.1109/TPEL.2011.2143730.

[52] M. M. Biswas, "Comparison study of inductive wireless power transfer pad topologies for electric vehicle charging", University of Akron, 2018. Accessed: May 12, 2022. [Online]. Available: https://etd.ohiolink.edu/apexprod/rws_olink/r/1501/10?clear=10&p10_accession_num=akron1536943828810247

[53] M. McDonough and B. Fahimi, "Comparison between circular and square coils for use in Wireless Power Transmission", in 9th IET International Conference on Computation in Electromagnetics (CEM 2014), Mar. 2014, pp. 1–2. doi: 10.1049/cp.2014.0243.

[54] Z. Duan, Y.-X. Guo, and D.-L. Kwong, "Rectangular coils optimization for wireless power transmission", Radio Science, vol. 47, no. 3, 2012, doi: 10.1029/2011RS004970.

[55] M. Budhia, J. T. Boys, G. A. Covic, and C. Y. Huang, "Development of a single-sided flux magnetic coupler for electric vehicle IPT charging systems," IEEE Trans. Ind. Electron., vol. 60, no. 1, pp. 318–328, Jan. 2013.

[56] A. Zaheer, G. A. Covic, and D. Kacprzak, "A bipolar pad in a 10-kHz 300-W distributed IPT system for AGV applications," IEEE Trans. Ind. Electron., vol. 61, no. 7, pp. 3288–3301, 2014.

[57] H. Matsumoto, Y. Neba, H. Iura, D. Tsutsumi, K. Ishizaka, and R. Itoh, "Trifoliate Three-Phase Contactless Power Transformer in Case of Winding-Alignment", IEEE Transactions on Industrial Electronics, vol. 61, no. 1, pp. 53–62, Jan. 2014, doi: 10.1109/TIE.2013.2242421.

[58] S. Kim, G. A. Covic, and J. T. Boys, "Tripolar pad for inductive power transfer systems for EV charging", IEEE Trans. Power Electron., vol. 32, no. 7, pp. 5045–5057, Jul. 2017.

[59] Y. Li, R. Mai, L. Lu, and Z. He, "A novel IPT system based on dual coupled primary tracks for high power applications", J. Power Electron., vol. 16, no. 1, pp. 111–120, Jan. 2016.

[60] Y. Li, T. Lin, R. Mai, L. Huang, and Z. He, "Compact double-sided decoupled coils-based WPT systems for high-power applications: Analysis, design, and experimental verification", IEEE Trans. Transp. Electrific., vol. 4, no. 1, pp. 64–75, Mar. 2018.

[61] D. Patil, M. K. McDonough, J. M. Miller, B. Fahimi, and P. T. Balsara, "Wireless power transfer for vehicular applications: Overview and challenges", IEEE Trans. Transport. Electrific., vol. 4, no. 1, pp. 3–37, Mar. 2018.

[62] M. L. Hiles, R. G. Olsen, K. C. Holte, D. R. Jensen, and K. L. Griffing, "Power frequency magnetic field management using a combination of active and passive shielding technology", IEEE Transactions on Power Delivery, vol. 13, no. 1, pp. 171–179, Jan. 1998, doi: 10.1109/61.660875.

[63] J. Zhou, Y. Gao, C. Zhou, J. Ma, X. Huang, and Y. Fang, "Optimal power transfer with aluminum shielding for wireless power transfer systems", in 2017 20th International Conference on Electrical Machines and Systems (ICEMS), Aug. 2017, pp. 1–4. doi: 10.1109/ICEMS.2017.8056143.

[64] M. Mohammad, E. T. Wodajo, S. Choi, and M. E. Elbuluk, "Modeling and Design of Passive Shield to Limit EMF Emission and to Minimize Shield Loss in Unipolar Wireless Charging System for EV", IEEE Transactions on Power Electronics, vol. 34, no. 12, pp. 12235–12245, Dec. 2019, doi: 10.1109/TPEL.2019.2903788.

[65] A. A. S. Mohamed and A. A. Shaier, "Shielding Techniques of IPT System for Electric Vehicles' Stationary Charging", in Electric Vehicle Integration in a Smart Microgrid Environment, CRC Press, 2021.

[66] T. Campi, S. Cruciani, and M. Feliziani, "Magnetic shielding of wireless power transfer systems", in Proc. Int. Symp. Electromagn. Compat.,Tokyo, Japan, May 2014, pp. 422–425.

[67] M. Mohammad, J. Pries, O. Onar, V. P. Galigekere, G.-J. Su, S. Anwar, J. Wilkins, U. D. Kavimandan, and D. Patil, "Design of an EMF suppressing magnetic shield for a 100-kW DD-coil wireless charging system for electric

vehicles", in Proc. IEEE Appl. Power Electron. Conf. Expo. (APEC), Mar. 2019, pp. 1521–1527.
[68] K. Kadem, et al.. An Efficient Method for Dimensioning Magnetic Shielding for an Induction Electric Vehicle Charging System. Progress In Electromagnetics Research, EMW Publishing, 2021, 170, pp.153-167.
[69] X. Zhang, Z. Yuan, Q. Yang, H. Meng, Y. Jin, Z. Wang, and S. Jiang, "High-frequency electromagnetic force characteristics on electromagnetic shielding materials in wireless power transmission system", in Proc. IEEE PELS Workshop Emerg. Technologies: Wireless Power Transf. (WoW), May 2017, pp. 1–5.
[70] C. Yao, W. Zhao, D. Ma, X. Yang, and H. Tang, "3D modelling of metal shield on circular coil pad for contactless electric vehicle charging using finite element analysis", in 2016 IEEE 2nd Annual Southern Power Electronics Conference (SPEC), Dec. 2016, pp. 1–5. doi: 10.1109/SPEC.2016.7846005.
[71] T. Campi, S. Cruciani, F. Maradei, and M. Feliziani, "Active coil system for magnetic field reduction in an automotive wireless power transfer system", in Proc. IEEE Int. Symp. Electromagn. Compat., Signal PowerIntegrity (EMC+SIPI), Jul. 2019, pp. 189–192.
[72] S. Y. Choi, B. W. Gu, S. W. Lee, W. Y. Lee, J. Huh, and C. T. Rim, "Generalized active EMF cancel methods for wireless electric vehicles", IEEE Trans. Power Electron., vol. 29, no. 11, pp. 5770–5783, Nov. 2014.
[73] T. Campi, S. Cruciani, F. Maradei, and M. Feliziani, "Magnetic field mitigation by multicoil active shielding in electric vehicles equipped with wireless power charging system", IEEE Trans. Electromagn. Compat., vol. 62, no. 4, pp. 1398–1405, Aug. 2020.
[74] J. Park et al. "Planar multiresonance reactive shield for reducing electromagnetic interference in portable wireless power charging application", Applied Physics Letters: Vol 114, No 20'. https://aip.scitation.org/doi/10.1063/1.5097038 (accessed Sep. 25, 2022).
[75] S. Kim, H.-H. Park, J. Kim, J. Kim, and S. Ahn, "Design and analysis of a resonant reactive shield for a wireless power electric vehicle", IEEE Trans. Microw. Theory Techn., vol. 62, no. 4, pp. 1057–1066, Apr. 2014.
[76] H. Moon, S. Kim, H. H. Park, and S. Ahn, "Design of a resonant reactive shield with double coils and a phase shifter for wireless charging of electric vehicles,'' IEEE Trans. Magn., vol. 51, no. 3, pp. 1–4, Mar. 2015.
[77] L. Tan, K. E. I. Elnail, M. Ju, and X. Huang, "Comparative Analysis and Design of the Shielding Techniques in WPT Systems for Charging EVs," Energies, vol. 12, no. 11, p. 2115, Jun. 2019, doi: 10.3390/en12112115.
[78] M. Ibrahim, "Wireless Inductive Charging for Electrical Vehicules : Electromagnetic Modelling and Interoperability Analysis", phdthesis, Université Paris Sud – Paris XI, 2014. Accessed: Jun. 22, 2022. [Online]. Available: https://tel.archives-ouvertes.fr/tel-01127163
[79] E. Asa, M. Mohammad, O. C. Onar, J. Pries, V. Galigekere, and G.-J. Su, "Review of safety and exposure limits of electromagnetic fields (EMF) in wireless electric vehicle charging (WEVC) applications", in Proc. IEEE Transp. Electrific. Conf. Expo (ITEC), Jun. 2020, pp. 17_24.
[80] K. Kadem, "Modelling and optimization of a magnetic coupler for dynamic induction charging of electric vehicles", Theses, Centralesupelec, 2020. Accessed: May 24, 2022. [Online]. Available: https://hal.archives-ouvertes.fr/tel-03253967
[81] V. Shevchenko, O. Husev, R. Strzelecki, B. Pakhaliuk, N. Poliakov, and N. Strzelecka, "Compensation topologies in IPT systems: Standards, requirements, classification, analysis, comparison and application", IEEE Access, vol. 7, pp. 120559–120580, 2019.
[82] B. Esteban, M. Sid-Ahmed, and N. C. Kar, "A comparative study of power supply architectures in wireless EV charging systems", IEEE Trans. Power Electron., vol. 30, no. 11, pp. 6408–6422, Nov. 2015.
[83] F. Liu, Y. Zhang, K. Chen, Z. Zhao, and L. Yuan, "A comparative study of load characteristics of resonance types in wireless transmission systems", in Proc. Asia–Pacific Int. Symp. Electromagn. Compat. (APEMC), May 2016, pp. 203–206.
[84] A. Zaheer, M. Neath, H. Z. Z. Beh, and G. A. Covic, "A dynamic EV charging system for slow moving traffic applications", IEEE Trans. Transp. Electrific., vol. 3, no. 2, pp. 354–369, Jun. 2017.
[85] P. Zhang, M. Saeedifard, O. C. Onar, Q. Yang, and C. Cai, "A field enhancement integration design featuring misalignment tolerance for wireless EV charging using LCL topology", IEEE Trans. Power Electron., vol. 36, no. 4, pp. 3852–3867, Apr. 2021.
[86] S. Zhou and C. Mi, "Multi-paralleled LCC reactive power compensation networks and their tuning method for electric vehicle dynamic wireless charging", IEEE Trans. Ind. Electron., vol. 63, no. 10, pp. 6546–6556, Oct. 2016.
[87] F. Corti, L. Paolucci, A. Reatti, F. Grasso, L. Pugi, N. Tesi, E. Grasso, and M. Nienhaus, "A comprehensive comparison of resonant topologies for magnetic wireless power transfer", in Proc. IEEE 20th Medit. Electrotech. Conf. (MELECON), Jun. 2020, pp. 582–587.
[88] N. Shinohara, "Trends in wireless power transfer: WPT technology for energy harvesting, mllimeter-wave/THz

rectennas, MIMO-WPT, and advances in near-field WPT applications", IEEE Microw. Mag., vol. 22, no. 1, pp. 46–59, Jan. 2021.

[89] R. Bosshard, J. W. Kolar, J. Mühlethaler, I. Stevanovi ć, B. Wunsch, and F. Canales, "Modeling and eta-alpha-Pareto optimization of inductive power transfer coils for electric vehicles," IEEE J. Emerg. Sel. Topics Power Electron., vol. 3, no. 1, pp. 50–64, Mar. 2015, doi: 10.1109/JESTPE.2014.2311302.

[90] A. Hariri, A. Elsayed, and O. A. Mohammed, "An integrated characterization model and multiobjective optimization for the design of an EV charger's circular wireless power transfer pads," IEEE Trans. Magn., vol. 53, no. 6, pp. 1–4, Jun. 2017, doi: 10.1109/TMAG.2017.2661722.

[91] T. Yilmaz, N. Hasan, R. Zane, and Z. Pantic, "Multi-objective optimization of circular magnetic couplers for wireless power transfer applications," IEEE Trans. Magn., vol. 53, no. 8, pp. 1–12, Aug. 2017, doi: 10.1109/TMAG.2017.2692218.

[92] A. A. S. Mohamed, S. An, and O. Mohammed, "Coil design optimization of power pad in IPT system for electric vehicle applications," IEEE Trans. Magn., vol. 54, no. 4, pp. 1–5, Apr. 2018, doi: 10.1109/TMAG.2017.2784381.

[93] M. Lu and K. D. T. Ngo, "Systematic design of coils in series–series inductive power transfer for power transferability and efficiency," IEEE Trans. Power Electron., vol. 33, no. 4, pp. 3333–3345, Apr. 2018, doi:10.1109/TPEL.2017.2706306.

[94] M. Mohammad, S. Choi, and M. E. Elbuluk, "Loss minimization design of ferrite core in a DD-coil-based high-power wireless charging system for electrical vehicle application," IEEE Trans. Transport. Electrific., vol. 5, no. 4, pp. 957–967, Dec. 2019, doi: 10.1109/TTE.2019.2940878.

[95] Y. Otomo and H. Igarashi, "Topology optimization of magnetic couplers for wireless power transfer considering electromagnetic shields," in Proc. 45th Annu. Conf. IEEE Ind. Electron. Soc. (IECON), Oct. 2019, pp. 4341–4344, doi: 10.1109/IECON.2019.8927357.

[96] M. G. S. Pearce, M. J. O'Sullivan, C. Carretero, G. A. Covic, and J. T. Boys, "Optimising ferrite-less pad reflection winding with a multiobjective genetic algorithm," in Proc. IEEE PELS Workshop Emerg. Technol. Wireless Power Transfer (WoW), Jun. 2019, pp. 165–168, doi: 10.1109/WoW45936.2019.9030684.

[97] S. Bandyopadhyay, P. Venugopal, J. Dong, and P. Bauer, "Comparison of magnetic couplers for IPT-based EV charging using multi-objective optimization," IEEE Trans. Veh. Technol., vol. 68, no. 6, pp. 5416–5429, Jun. 2019.

[98] M. Bertoluzzo, M. Forzan, P. Di Barba, M. E. Mognaschi, and E. Sieni, "Pareto optimal solutions of a wireless power transfer system," Eur. Phys. J. Appl. Phys., vol. 90, no. 2, p. 20904, May 2020, doi: 10.1051/epjap/2020200052.

[99] Y. Yao, S. Gao, Y. Wang, X. Liu, X. Zhang, and D. Xu, "Design and optimization of an electric vehicle wireless charging system using interleaved boost converter and flat solenoid coupler," IEEE Trans. Power Electron., vol. 36, no. 4, pp. 3894–3908, Apr. 2021, doi: 10.1109/TPEL.2020.3019441

[100] R. K. Yakala, S. Pramanick, D. P. Nayak, and M. Kumar, "Optimization of Circular Coil Design for Wireless Power Transfer System in Electric Vehicle Battery Charging Applications", Trans Indian Natl. Acad. Eng., vol. 6, no. 3, pp. 765–774, Sep. 2021, doi: 10.1007/s41403-021-00224-z.

[101] K. Chen, J. Pan, Y. Yang, and K. W. E. Cheng, "Optimization of Ferrites Structure by Using a New Core-Less Design Algorithm for Electric Vehicle Wireless Power Transfer", Energies, vol. 14, no. 9, p. 2590, Jan. 2021, doi: 10.3390/en14092590.

[102] W. Shi et al., "Design of a Highly Efficient 20-kW Inductive Power Transfer System With Improved Misalignment Performance", IEEE Transactions on Transportation Electrification, vol. 8, no. 2, pp. 2384–2399, Jun. 2022, doi: 10.1109/TTE.2021.3133759.

[103] H. Zhao et al., "Shielding Optimization of IPT System Based on Genetic Algorithm for Efficiency Promotion in EV Wireless Charging Applications", IEEE Transactions on Industry Applications, vol. 58, no. 1, pp. 1190–1200, Jan. 2022, doi: 10.1109/TIA.2021.3121353.

[104] Y. Li et al., "A new coil structure and its optimization design with constant output voltage and constant output current for electric vehicle dynamic wireless charging," IEEE Trans. Ind. Informat., vol. 15, no. 9, pp. 5244–5256, Sep. 2019, doi: 10.1109/tii.2019.2896358.

[105] Y. Zhang, J. Deng, S. Wang, Z. Wang, and Y. Yang, "Multi-objective optimization of single-transmitter coupled multi-receiver IPT system for maglev trains," in Proc. IEEE Appl. Power Electron. Conf. Expo (APEC), Mar. 2020, pp. 1649–1654, doi: 10.1109/APEC39645.2020.9124214.

[106] R. Tavakoli, E. M. Dede, C. Chou, and Z. Pantic, "Cost-Efficiency Optimization of Ground Assemblies for Dynamic Wireless Charging of Electric Vehicles", IEEE Transactions on Transportation Electrification, vol. 8, no. 1, pp. 734–751, Mar. 2022, doi: 10.1109/TTE.2021.3105573.

[107] Y. Otomo and H. Igarashi, "A 3-D Topology Optimization of Magnetic Cores for Wireless Power Transfer Device",

IEEE Transactions on Magnetics, vol. 55, no. 6, pp. 1–5, Jun. 2019, doi: 10.1109/TMAG.2019.2900744.
[108] Y. Gong, Y. Otomo, and H. Igarashi, "Multi-objective topology optimization of magnetic couplers for wireless power transfer", International Journal of Applied Electromagnetics and Mechanics, vol. 64, no. 1–4, pp. 325–333, Jan. 2020, doi: 10.3233/JAE-209337.
[109] Y. Otomo and H. Igarashi, "Topology optimization of magnetic cores for WPT using the geometry projection method", COMPEL - The international journal for computation and mathematics in electrical and electronic engineering, vol. 41, no. 3, pp. 889–899, Jan. 2021, doi: 10.1108/COMPEL-02-2021-0064.
[110] M. Hu, U. K. Madawala, and C. Baguley, "The Optimal Placement of Ferrite in Inductive Power Transfer Coupling Pads", in 2021 IEEE 12th Energy Conversion Congress & Exposition - Asia (ECCE-Asia), May 2021, pp. 469–474. doi: 10.1109/ECCE-Asia49820.2021.9479004.
[111] M.P. Bendsøe and O.Sigmund, "Material interpolation schemes in topology optimization. Archive of Applied Mechanics 69, 635–654 (1999). https://doi-org.ezproxy.universite-paris-saclay.fr/10.1007/s004190050248
[112] T. Sato, K. Watanabe, and H. Igarashi, "Multimaterial Topology Optimization of Electric Machines Based on Normalized Gaussian Network," IEEE Trans. Magn., vol. 51, no. 3, Art. no. 7202604, 2015.
[113] M. Moustapha, C. Lataniotis, S. Marelli, B. Sudret, UQLab user manual – Support vector machines for regression, Report UQLab-V2.0-111, Chair of Risk, Safety and Uncertainty Quantification, ETH Zurich, Switzerland, 2022.
[114] D. P. Searson, "GPTIPS 2: An Open-Source Software Platform for Symbolic Data Mining," in Handbook of Genetic Programming Applications, A. H. Gandomi, A. H. Alavi, and C. Ryan, Eds. Cham: Springer International Publishing, 2015, pp. 551–573. doi: 10.1007/978-3-319-20883-1_22.
[115] G. Blatman and B. Sudret, "Adaptive sparse polynomial chaos expansion based on least angle regression", Journal of Computational Physics, vol. 230, no. 6, pp. 2345–2367, Mar. 2011, doi: 10.1016/j.jcp.2010.12.021.
[116] R. Trinchero, M. Larbi, H. M. Torun, F. G. Canavero, and M. Swaminathan, "Machine Learning and Uncertainty Quantification for Surrogate Models of Integrated Devices With a Large Number of Parameters", IEEE Access, vol. 7, pp. 4056–4066, 2019, doi: 10.1109/ACCESS.2018.2888903.
[117] G. D. Capua et al., "Mutual Inductance Behavioral Modeling for Wireless Power Transfer System Coils", IEEE Transactions on Industrial Electronics, vol. 68, no. 3, pp. 2196–2206, Mar. 2021, doi: 10.1109/TIE.2019.2962432.
[118] A. Delgado et al., "Self and Mutual Inductance Behavioral Modeling of Square-Shaped IPT Coils With Air Gap and Ferrite Core Plates," IEEE Access, vol. 10, pp. 7476–7488, 2022, doi: 10.1109/ACCESS.2021.3138239.
[119] G. Di Capua, A. Maffucci, K. Stoyka, G. Di Mambro, S. Ventre, V. Cirimele, F. Freschi, F. Villone, N. Femia, "Analysis of dynamic wireless power transfer systems based on behavioral modeling of mutual inductance", Sustainability, vol. 13, Feb. 2021.
[120] V. Cirimele et al., "Uncertainty Quantification for SAE J2954 Compliant Static Wireless Charge Components", IEEE Access, vol. 8, pp. 171489–171501, 2020, doi: 10.1109/ACCESS.2020.3025052.
[121] B. Sudret, "Global sensitivity analysis using polynomial chaos expansions", Rel. Eng. Syst. Saf., vol. 93, no. 7, pp. 964_979, Jul. 2008.
[122] D. Kalyanmoy. "Multi-Objective Optimization using Evolutionary Algorithms," John Wiley & Sons, Ltd, Chichester, England, 2001.
[123] C. A. C. Coello, G. T. Pulido, and M. S. Lechuga, "Handling multiple objectives with particle swarm optimization", IEEE Transactions on Evolutionary Computation, vol. 8, no. 3, pp. 256–279, Jun. 2004, doi: 10.1109/TEVC.2004.826067.
[124] M. M. Biswas, "Comparison study of inductive wireless power transfer pad topologies for electric vehicle charging", University of Akron, 2018. Accessed: May 12, 2022. [Online]. Available: https://etd.ohiolink.edu/apexprod/rws_olink/r/1501/10?clear=10&p10_accession_num=akron1536943828810247
[125] A. Ahmad and M. S. Alam, "Magnetic Analysis of Copper Coil Power Pad with Ferrite Core for Wireless Charging Application", Trans. Electr. Electron. Mater., vol. 20, no. 2, pp. 165–173, Apr. 2019, doi: 10.1007/s42341-018-00091-6.
[126] Z. Luo and X. Wei, "Analysis of Square and Circular Planar Spiral Coils in Wireless Power Transfer System for Electric Vehicles", IEEE Transactions on Industrial Electronics, vol. 65, no. 1, pp. 331–341, Jan. 2018, doi: 10.1109/TIE.2017.2723867.
[127] A. Zaheer, H. Hao, G. A. Covic, and D. Kacprzak, "Investigation of Multiple Decoupled Coil Primary Pad Topologies in Lumped IPT Systems for Interoperable Electric Vehicle Charging", IEEE Transactions on Power Electronics, vol. 30, no. 4, pp. 1937–1955, Apr. 2015, doi: 10.1109/TPEL.2014.2329693.
[128] T. Batra, "Design of Static Wireless Charging System for Electric Vehicles with Focus on Magnetic Coupling and

Emissions," Dec. 2015, Accessed: Mar. 25, 2021. [Online]. Available: https://vbn.aau.dk/en/publications/design-of-static-wireless-charging-system-for-electric-vehicles-w

[129] K. Kadem, M. Bensetti, Y. Le Bihan, E. Labouré, and M. Debbou, "Optimal Coupler Topology for Dynamic Wireless Power Transfer for Electric Vehicle," Energies, vol. 14, no. 13, p. 3983, Jul. 2021, doi: 10.3390/en14133983.

[130] Y. Yang, J. Cui, and X. Cui, "Design and Analysis of Magnetic Coils for Optimizing the Coupling Coefficient in an Electric Vehicle Wireless Power Transfer System", Energies, vol. 13, no. 16, pp. 1–15, 2020, Accessed: May 25, 2021. [Online]. Available: https://ideas.repec.org/a/gam/jeners/v13y2020i16p4143-d397479.html.

[131] R. Bosshard, J. Mühlethaler, J. W. Kolar, and I. Stevanović, "Optimized magnetic design for inductive power transfer coils," in 2013 Twenty-Eighth Annual IEEE Applied Power Electronics Conference and Exposition (APEC), Mar. 2013, pp. 1812–1819. doi: 10.1109/APEC.2013.6520541.

[132] "Software for Simulating Static and Low-Frequency Electromagnetics," COMSOL. https://www.comsol.com/acdc-module (accessed Jan. 29, 2022).

[133] P. S. R. Nayak and D. Kishan, "Design and analysis of SS resonant IPT system with computed mutual inductance through FEM model," in 2018 International Conference on Power, Instrumentation, Control and Computing (PICC), Jan. 2018, pp. 1–5. doi: 10.1109/PICC.2018.8384758.

[134] V. Cirimele, "Design and integration of a dynamic IPT system for automotive applications," PhD thesis, Université Paris Saclay; Politecnico di Torino, 2017. Accessed: Nov. 10, 2020. [Online]. Available: https://tel.archives-ouvertes.fr/tel-01578716

[135] R. W. Erickson and D. Maksimović, "Inductor Design," in Fundamentals of Power Electronics, R. W. Erickson and D. Maksimović, Eds. Boston, MA: Springer US, 2001, pp. 539–564. doi: 10.1007/0-306-48048-4_14.

[136] "High Frequency Litz Wires." [Online]. Available: https://www.schupp.ch/gb/katalog_gb_pdf/LTHF_high_frequency_stranded_wires.pdf (accessed: Jun. 07, 2022).

[137] "Taped | ELEKTRISOLA". https://www.elektrisola.com/en/Products/Litz-Wire/Products/Taped (accessed: Jun. 07, 2022).

[138] T. Guillod, J. Huber, F. Krismer, and J. W. Kolar, "Litz wire losses: Effects of twisting imperfections", in 2017 IEEE 18th Workshop on Control and Modeling for Power Electronics (COMPEL), Jul. 2017, pp. 1–8. doi: 10.1109/COMPEL.2017.8013327.

[139] Y. Tang, H. Ma, D. J. Thrimawithana, and U. K. Madawala, "Copper foil windings for WPT systems," in Proc. IEEE PELS Workshop Emerg. Technol., Chongqing, China, May 2017, pp. 162–167.

[140] Keysight, "E4990A Impedance Analyzer, 20 Hz to 10/20/30/50/120 MHz," Keysight. https://www.keysight.com/fr/en/product/E4990A/impedance-analyzer-20-hz-10-20-30-50-120-mhz.html (accessed Mar. 02, 2022).

[141] "RF & Near-Field Probes for EMC Measurements", Aaronia AG. https://aaronia.com/antennas/rf-and-near-field-probes/ (accessed Jun. 09, 2022).

[142] MITEQ, "Datasheet MITEQ amplifier AU-1442," 2022. [Online]. Available: https://nardamiteq.com/viewmodel.php?model=AU-1442.

[143] " Tektronix RSA5106A | RF & Microwave Spectrum Analyzers | Location, leasing ou achat de matériel de test neuf et d'occasion". https://www.electrorent.com/fr/products/rf-and-microwave-spectrum-analyzers/spectrum-analyzers-performance/tektronix/rsa5106a/01t1O000004Tep0QAC (accessed Jun. 09, 2022).

[144] F. Benyoubi, "Near-field characterization of radiated emissions from electromagnetic shielding boxes", these de doctorat, Nantes, 2019. Accessed: May 12, 2022. [Online]. Available: http://www.theses.fr/2019NANT4004

[145] V. Rajamani, C. F. Bunting, A. Orlandi, and A. Duffy, "Introduction to feature selective validation (FSV)," in 2006 IEEE Antennas and Propagation Society International Symposium, Jul. 2006, pp. 601–604. doi: 10.1109/APS.2006.1710595.

[146] F. Benyoubi, L. Pichon, M. Bensetti, Y. Le Bihan, and M. Feliachi, "An Efficient Method for Modeling the Magnetic Field Emissions of Power Electronic Equipment From Magnetic Near Field Measurements," IEEE Transactions on Electromagnetic Compatibility, vol. 59, no. 2, pp. 609–617, Apr. 2017, doi: 10.1109/TEMC.2016.2643167.

[147] "LE GUIPAGE MODERNE". http://www.leguipagemoderne.fr/ (accessed Jun. 08, 2022).

[148] TDK, "N27 Ferrite Datasheet." [Online]. Available: http://scholar.google.com/scholar?hl=en&btnG=Search&q=intitle:Ferrites+and+accessories#0.

[149] "NF Corporation: High Speed Bipolar Amplifier". https://www.nfcorp.co.jp/english/pro/pp/p_amp/h_spe/hsa_s/index.html (accessed Jun. 09, 2022).

[150] E. B. Rosa, "Calculation of the Self-Inductance of Single-Layer Coils", 2018. doi: 10.6028/bulletin.034.

[151] S. J. Ling, W. Moebs, and J. Sanny, "12.4 Magnetic Field of a Current Loop", Sep. 2016, Accessed: Jul. 15, 2022.

[Online]. Available: https://pressbooks.online.ucf.edu/osuniversityphysics2/chapter/magnetic-field-of-a-current-loop/

[152] M. Larbi, I. S. Stievano, F. G. Canavero, and P. Besnier, "Variability impact of many design parameters: The case of a realistic electronic link", IEEE Trans. Electromagn. Compat., vol. 60, no. 1, pp. 34-41, Feb. 2018.

[153] S. De Ridder et al., "A Generative Modeling Framework for Statistical Link Analysis Based on Sparse Data", IEEE Transactions on Components, Packaging and Manufacturing Technology, vol. 8, no. 1, pp. 21–31, Jan. 2018, doi: 10.1109/TCPMT.2017.2761907.

[154] R. Trinchero, P. Manfredi, I. S. Stievano, and F. G. Canavero, "Machine learning for the performance assessment of high-speed links", IEEE Trans. Electromagn. Compat., vol. 60, no. 6, pp. 1627-1634, Dec. 2018.

[155] I. M. Sobol, "Sensitivity estimates for nonlinear mathematical models", Math. Model. Comput. Exp., vol. 1, no. 4, pp. 407-414, 1990.

[156] J. A. K. Suykens, T. Van Gestel, J. De Brabanter, B. De Moor, and J. Vandewalle, Least Squares Support Vector Machines. Singapore: World Scientific, 2002.

[157] "The Nature of Statistical Learning Theory | SpringerLink". https://link-springer-com.ezproxy.universite-paris-saclay.fr/book/10.1007/978-1-4757-3264-1 (accessed Apr. 08, 2022).

[158] S. Marelli, and B. Sudret, UQLab: A framework for uncertainty quantification in Matlab, Proc. 2nd Int. Conf. on Vulnerability, Risk Analysis and Management (ICVRAM2014), Liverpool, United Kingdom, 2014, 2554-2563.

[159] M. Mitchell, "An Introduction to Genetic Algorithms | The MIT Press". https://mitpress.mit.edu/books/introduction-genetic-algorithms (accessed Jul. 18, 2022).

[160] G. F. Smits and M. Kotanchek, "Pareto-Front Exploitation in Symbolic Regression", in Genetic Programming Theory and Practice II, U.-M. O'Reilly, T. Yu, R. Riolo, and B. Worzel, Eds. Boston, MA: Springer US, 2005, pp. 283–299. doi: 10.1007/0-387-23254-0_17.

[161] C. Soize and R. Ghanem, "Physical systems with random uncertainties: Chaos representations with arbitrary probability measure", SIAM J. Sci. Comput., vol. 26, no. 2, pp. 395-410, 2004.

[162] M. Berveiller, B. Sudret, and M. Lemaire,"Stochastic finite element: A nonintrusive approach by regression", Eur. J. Comput. Mech., vol. 15, nos. 1_3, pp. 81-92, 2006.

[163] S. Marelli, N. Luthen, B. Sudret, UQLab user manual – Polynomial chaos expansions, Report UQLab-V2.0-104, Chair of Risk, Safety and Uncertainty Quantification, ETH Zurich, Switzerland, 2022.

[164] D. C. Montgomery, Design and Analysis of Experiments. New York, NY, USA: Wiley, 2004.

[165] S. Marelli, C. Lamas, K. Konakli, C. Mylonas, P. Wiederkehr, B. Sudret, UQLab user manual – Sensitivity analysis, Report UQLab-V2.0-106, Chair of Risk, Safety and Uncertainty Quantification, ETH Zurich, Switzerland, 2022.

[166] C. Lataniotis, E. Torre, S. Marelli, B. Sudret, UQLab user manual – The Input module, Report UQLab-V2.0-102, Chair of Risk, Safety and Uncertainty Quantification, ETH Zurich, Switzerland, 2022.

[167] M. D. McKay, R. J. Beckman, and W. J. Conover, "A Comparison of Three Methods for Selecting Values of Input Variables in the Analysis of Output from a Computer Code", Technometrics, vol. 21, no. 2, pp. 239–245, 1979, doi: 10.2307/1268522.

[168] M. Lu and K. D. T. Ngo, "Systematic Design of Coils in Series–Series Inductive Power Transfer for Power Transferability and Efficiency," IEEE Transactions on Power Electronics, vol. 33, no. 4, pp. 3333–3345, Apr. 2018, doi: 10.1109/TPEL.2017.2706306.

[169] "gamultiobj Algorithm - MATLAB & Simulink". https://www.mathworks.com/help/gads/gamultiobj-algorithm.html?searchHighlight=gamultiobj&s_tid=srchtitle_gamultiobj_2.

[170] M. Bensetti, et al., "Inductive Coupler and Magnetic Induction Charging System for Electric and hybrid Vehicles". FR3094832A1, WO2020208313A1.

[171] J. Li, F. Yin, and L. Wang, "Transmission efficiency of different shielding structures in wireless power transfer systems for electric vehicles," CSEE Journal of Power and Energy Systems, vol. 7, no. 6, pp. 1247–1255, Nov. 2021, doi: 10.17775/CSEEJPES.2019.00500.

[172] T. Campi, S. Cruciani, V. De Santis, F. Maradei, and M. Feliziani, "Magnetic field behavior in a carbon-fiber electrical vehicle charged by a wireless power transfer system," in 2017 International Symposium on Electromagnetic Compatibility - EMC EUROPE, Sep. 2017, pp. 1–6. doi: 10.1109/EMCEurope.2017.8094723.

[173] "Improving Your Meshing with Swept Meshes", COMSOL. https://www.comsol.fr/blogs/improving-your-meshing-with-swept-meshes/ (accessed Sep. 04, 2022).

[174] "Transition Boundary Condition". https://doc.comsol.com/5.5/doc/com.comsol.help.woptics/woptics_ug_optics.6.24.html (accessed Aug. 03, 2022).

[175] S. Cruciani, T. Campi, F. Maradei, and M. Feliziani, "Conductive Layer Modeling by Improved Second-Order

Artificial Material Single-Layer Method," IEEE Transactions on Antennas and Propagation, vol. 66, no. 10, pp. 5646–5650, Oct. 2018, doi: 10.1109/TAP.2018.2854413.

[176] M. Feliziani, S. Cruciani, T. Campi, and F. Maradei, "Artificial Material Single Layer to Model the Field Penetration Through Thin Shields in Finite-Elements Analysis", IEEE Transactions on Microwave Theory and Techniques, vol. 66, no. 1, pp. 56–63, Jan. 2018, doi: 10.1109/TMTT.2017.2737994.

[177] J. Sallan, J. L. Villa, A. Llombart, and J. Fco. Sanz, "Optimal Design of ICPT Systems Applied to Electric Vehicle Battery Charge", IEEE Transactions on Industrial Electronics, vol. 56, no. 6, pp. 2140–2149, Jun. 2009, doi: 10.1109/TIE.2009.2015359.

[178] E. ElGhanam, M. Hassan, A. Osman, and H. Kabalan, "Design and Performance Analysis of Misalignment Tolerant Charging Coils for Wireless Electric Vehicle Charging Systems", World Electric Vehicle Journal, vol. 12, no. 3, p. 89, Sep. 2021, doi: 10.3390/wevj12030089.

[179] V. Martínez-Cagigal. Multi-Objective Particle Swarm Optimization (MOPSO) (https:// www. mathworks. com/matlabcentral/fileexchange/62074-multi-objective-particle-swarm-optimization-mopso), MATLAB Central File Exchange.

[180] B. S. B. Mohamodhosen, "Topology optimisation of electromagnetic devices", Theses, Ecole Centrale de Lille, 2017. Accessed: Jul. 29, 2022. [Online]. Available: https://tel.archives-ouvertes.fr/tel-01818091

[181] M.P. Bendsøe, "Optimal shape design as a material distribution problem," Structural Optimization, vol. 1, pp. 193–202, 1989.

[182] "Performing Topology Optimization with the Density Method", COMSOL. https://www.comsol.com/blogs/performing-topology-optimization-with-the-density-method/ (accessed Sep. 04, 2022).

[183] T. Kva°Lseth, "Note on the R2 measure of goodness of fit for nonlinear models", Bull. Psychon. Soc. vol. 21 (1), p.79–80, Jan. 1983, doi: https://doi-org.ezproxy.universite-paris-saclay.fr/10.3758/BF03329960.

[184] A.-N. Spiess and N. Neumeyer, "An evaluation of R2 as an inadequate measure for nonlinear models in pharmacological and biochemical research: a Monte Carlo approach", BMC Pharmacol, vol. 10, p. 6, Jun. 2010, doi: 10.1186/1471-2210-10-6.

[185] J. Frost, "R-squared Is Not Valid for Nonlinear Regression", Statistics By Jim, Apr. 10, 2017. http://statisticsbyjim.com/regression/r-squared-invalid-nonlinear-regression/ (accessed Aug. 10, 2022).

[186] F. Lu, H. Zhang, H. Hofmann, and C. C. Mi, "An inductive and capacitive combined wireless power transfer system with LC-compensated topology," IEEE Trans. Power Electron., vol. 31, no. 12, pp. 8471–8482, Dec. 2016.

[187] B. Luo, T. Long, R. Mai, R. Dai, Z. He, and W. Li, "Analysis and design of hybrid inductive and capacitive wireless power transfer for high-power applications," IET Power Electron., vol. 11, no. 14, pp. 2263–2270, Nov. 2018.